Optical Focusing and Imaging through Scattering Media

Thesis by
Edward Haojiang Zhou

In Partial Fulfillment of the Requirements for the
degree of
Doctor of Philosophy

CALIFORNIA INSTITUTE OF TECHNOLOGY
Pasadena, California

2017
Defended May 9th, 2017

Edward Haojiang Zhou
ORCID: 0000-0001-7020-9502

To Dr. Changhuei Yang and Dr. Benjamin Judkewitz, who, by their examples, encouraged me to walk the path of learning and researching, and to my wife Shihan, who walks it with me.

ACKNOWLEDGEMENTS

First and foremost, I would like to express my heartfelt thanks to Prof. Changhuei Yang, who, as my supervisor, earnestly propagates the doctrine, imparts professional knowledge, and resolves doubts. Through his mentorship and supervision, I learned how to do independent research and the importance of persistence when facing obstacles. Through his support and encouragement, I was able to explore the unknown, develop new ideas, and do interesting science. All of these have become my invaluable assets.

I would like to thank Prof. Benjamin Judkewitz for being my mentor in the first two years of my study. He helped me through the days when I was ignorant, naive and impatient. I learned the importance of concentration, professionalism, and optimism. He helped me build up my basis in experimental and theoretical optics. Even now, I still learn remotely from his wisdom in life and research.

My committee members Prof. Yu-Chong Tai, Prof. P. P. Vaidyanathan, and Prof. Long Cai have been extremely supportive and taken time from their busy schedules to supervise my candidacy and defense. I am very grateful for their precious insights and generous help. Moreover, as outstanding scientists in their respective fields, they also shared their philosophy of doing research with me. I still remember when Prof. Tai told me: "When you came across obstacles in solving the problem, do not always treat them as your enemies, try to turn your enemies into friends." Prof. Cai asked me to be brave to face up to competition. My knowledge of signals and systems is built up on Prof. Vaidyanathan's EE 111 and 112 class.

You will find that this thesis contains work that I have done with collaborators. I would like to extend my sincere gratitude to them. Prof. Daifa Wang worked extensively on the architecture and programming of FPGA board. I am in debt to Dr. Haowen Ruan and Dr. Mooseok Jang for their unselfish suggestions and generous support in developing the ideas. I'd like to especially thank Dr. Atsushi Shibukawa, Albert Chung, Michelle Cua, and Josh Brake. They are reliable partners and talented scientists to work with. They are always ready to help out and get their hands dirty when I needed something quick or something I was not familiar with.

I would like to express my gratitude towards all members (both past and present) of the Biophotonics Lab. They made every day here enjoyable and the lab a great place for research. I would like to thank Dr. Ying Min Wang, Prof. Guoan Zheng,

Dr. Roarke Horstmeyer, Dr. Xiaoze Ou, Dr. Seung Ah Lee, and Jinho Kim for answering my naive quesitons, listening to my crazy ideas and giving their insightful suggestions. Thank you to Prof. Jiangtao Huangfu, Prof. Marinko Sarunic, Prof. Shuo Pang, Dr. Chao Han, Dr. Jian Ren, Jian Xu, Daniel Martin, Hangwen Lu, Hao Deng, Dr. Yan Liu, and Dr. Antony Chan. I have benefited a lot from their knowledge, intelligence and experience. They expanded my horizon in science and enriched my knowledge in different fields. A special thanks goes to Anne, our mom in the lab. She takes really good management of our lab, so that I can focus on my study and research.

I would like to thank all of my friends for making my time at Caltech pleasingly colorful. Chen, Wen, Hank, Eileen, and Sophy: you are my best buddies through fair and foul. Our conversation spanning over biochemistry, geophysics, material science, and architecture have always been great inspirations in my research. Our footprint across the mountains, beaches, and rivers in southern California have always been my cherished memory.

Finally, I'd like to take this chance to give my sincerest gratitude to my family. To my father Yi Zhou, though I would never have the chance to see him again. To my mother Jing Jiang, who dedicated herself to raise me up through the ups and downs. To my wife Shihan Su, who gave up her career, moved from Hong Kong to California resolutely, and stays with me through thick and thin.

ABSTRACT

Optical techniques, which have been widely used in various fields including biomedicine, remote sensing, astronomy, and industrial production, play an important role in modern life. Optical focusing and imaging, which correspond to the basic methods of utilizing light, are key to the implementation of optical techniques. In free space or a nearly transparent medium, optical imaging and focusing can be easily realized by using conventional optical elements, such as lenses and mirrors, due to the ballistic propagation of light in these media. However, in scattering media like biological tissue and fog, refractive index inhomogeneities cause diffusive propagation of light that increases with depth, which restricts the use of optical methods in thick, scattering media. Generally speaking, scattering media poses three challenges to optical focusing and imaging: wavefront aberrations, glare, and decorrelation. Wavefront aberrations can randomize light traveling through a scattering medium, disrupt the formation of focus, and break the conjugate relation in imaging. Glare caused by backscattering will largely impair the visibility of imaging, and decorrelation in dynamic media requires systems that counter the effect of scattering to operate faster than the decorrelation time. In this thesis, we explored solutions to the problem of scattering from different aspects. We presented Time Reversal by Analysis of Changing wavefronts from Kinetic targets (TRACK) technique to realize noninvasive optical focusing through a scattering medium. We showed that by taking the difference between time-varying scattering fields caused by a moving object and applying optical phase conjugation, light can be focused back to the location previously occupied by the object. To tackle the decorrelation of living tissue, we built up a fast digital optical phase conjugation (DOPC) system based on FPGA and DMD, which has a response time of 5.3 ms and was the fastest DOPC system in the world before 2017. We demonstrated that the system is fast enough to focus light through 2.3mm-thick living mouse skin. As for glare, inspired by noise canceling headphones, we invented an optical analogue termed coherence gated negation (CGN) technique. CGN can optically cancel out the glare in an active illumination imaging scenario to realize imaging through scattering media, like fog. In the experiment, we suppressed the glare by an order of magnitude and allowed improved imaging of a weak target. Finally, we demonstrated a method to image a moving target through scattering media noninvasively. Its principle roots are in the speckle-correlation-based imaging (SCI) invented by Ori Katz. We improved the

technique and extended its application to bright field imaging of a moving target.

PUBLISHED CONTENT AND CONTRIBUTIONS

- **Edward Haojiang Zhou**, Haowen Ruan, Changhuei Yang, and Benjamin Judkewitz. *Focusing on moving targets through scattering samples*. Optica 1, 227-232 (2014). DOI: 10.1364/OPTICA.1.000227.

  E.H.Z. participated in the design of the experiments. E.H.Z. built up the optical system, conducted optical experiments, and participated in analyzing the data and writing the manuscript.

- Daifa Wang*, **Edward Haojiang Zhou***, Joshua Brake, Haowen Ruan, Mooseok Jang, and Changhuei Yang. *Focusing through dynamic tissue with millisecond digital optical phase conjugation*. Optica 2, 728-735 (2015). DOI: 10.1364/OPTICA.2.000728. (* indicates equal contribution to the work.)

  E.H.Z. participated in the conception of the project and design of experiments. E.H.Z. built up the optical system, conducted optical experiments, and participated in analyzing the data and writing the manuscript.

- **Edward Haojiang Zhou**, Atsushi Shibukawa, Joshua Brake, and Changhuei Yang. *Glare suppression by coherence gated negation*. Optica 3, 1107-1113 (2016). DOI: 10.1364/OPTICA.3.001107.

  E.H.Z. participated in the conception of the project and design of experiments. E.H.Z. built up the optical system, conducted optical experiments, and participated in analyzing the data and writing the manuscript.

- Michelle Cua, **Edward Haojiang Zhou**, and Changhuei Yang. *Imaging moving targets through scattering media*. Optics Express 25, 3935-3945 (2017). DOI: 10.1364/OE.25.003935.

  E.H.Z. conceived the project and participated in designing the experiments, analyzing the data, and writing the manuscript.

TABLE OF CONTENTS

LIST OF ILLUSTRATIONS

Chapter 1

INTRODUCTION

Focusing and imaging correspond to two basic requirements in utilizing light: manipulating and observing. Optical focusing and imaging are of great importance in biomedicine, remote sensing, astronomy, industrial production, to name a few. The advantage of using light can be summarized in three aspects, as follows.

First, optical resolution is only limited by diffraction, and can reach sub-micrometer scale [1]. It enables optical focusing to have a precise spatial selectivity, which allows for stimulation or manipulation of micro structures and micro processes. For example, photolithography [2, 3] is an indispensable tool for integrated circuit fabrication, and optical focusing is also widely used for the control of cellular or subcellular biological systems, such as in photodynamic therapy [4], photoreleasing [5], optogenetics [6, 7], and optical cell trapping and shearing [8, 9]. Optical imaging with its fine resolution opens a door to the microworld through direct visualization. Optical microscopy [10, 11] has long been a reliable tool in diagnosis. Recent development in super-resolution microscopy [12–16] has pushed the resolution limit down to tens of nanometers, even several nanometers. Although electron [17] and scanning probe microscopy [18, 19] inherently possess a finer resolution (subnanometer), optical microscopy is still the only way to observe living processes at micro scale without harsh preparation procedures.

Second, due to the physical interaction between light and matter, it is possible to use optical focusing and imaging to investigate material compositions through spectroscopy, polarization, photoluminescence, and photoacoustics [20]. For instance, Raman spectroscopy [21–24] is extensively used to observe vibrational, rotational, and other low-frequency modes in a molecular system.

Third, optical focusing and imaging have the ability to perform at high temporal resolution. It enables us to control and observe temporal evolution of physical events, which led to the advent of ultrafast optics [25]. Tremendous efforts have been made in the development of ultrafast spectroscopy [26, 27], laser-controlled chemistry, and so on, among which one exciting achievement is that the world's fastest 2-D camera up to date can capture events at up to 100 billion frames per second [28].

Conventionally, optical focusing and imaging are realized by lenses in a transparent medium, like air or glass, which are based on the ballistic propagation of light. However, when light propagates through most scattering media, refractive index inhomogeneities cause diffuse scattering that increases with depth. This poses a major challenge to all the aforementioned optical methods. Moreover, glare caused by backscattering will largely impair the visibility of imaging, and time-varying scattering by dynamic media will also pose a challenge to the system response time. All of these factors fundamentally limit the feasibility of optical focusing and imaging in scattering media, such as biological tissues and fog. In this chapter, we provide an overview of the physics behind optical scattering, discuss the challenges brought in, and introduce different methods used to overcome scattering.

1.1 Physics of Scattering

Light interacts with matter in many different ways including absorption, elastic scattering, inelastic scattering, quasi-elastic scattering, nonlinear process. Here we limit our discussion to elastic scattering, which causes light to diffusively propagate in scattering media. We will first start with single particle scattering model, and then expand our discussion to a group of particles. Finally, based on the model, we will discuss the properties of real scattering media and conclude with some general "rules of thumb" that are useful when considering the interaction of light with tissue.

Scattering of a single particle

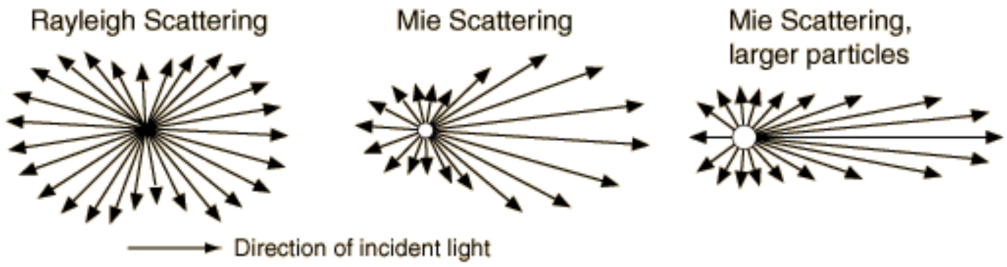

Figure 1.1: Rayleigh scattering and Mie scattering [29]

A simple model to start with is the scattering of a single small particle, which can be described as Rayleigh scattering or Mie scattering [30–32], as shown in Fig. 1.1. For particles much smaller than the wavelength of the incident light, their scattering of light can be explained by Rayleigh scattering. It is an approximation derived from the interaction between light and a dipole. The scattered intensity distribution $I(r, \theta)$

(expressed in polar coordinates) for unpolarized incident light can be expressed as [30, 32]

$$I_s(r,\theta) = 8\pi^4 {n_{su}}^4 (\frac{{n_s}^2 - {n_{su}}^2}{{n_s}^2 + 2{n_{su}}^2}) \frac{a^6}{r^2\lambda^4}(1+\cos^2\theta) I_0, \tag{1.1.1}$$

where I_0 is the incident light intensity, λ is its wavelength, n_s and n_{su} are the respective refractive indices of the scatterer and its surrounding medium, and a is the radius of the scatterer.

Mie scattering is applied when the particle size is on the order of the wavelength. It can be derived by solving Maxwell's equations for the case of a spherical scatter, composed of homogeneous and isotropic material, that is irradiated by a monochromatic plane wave [33]. The angular intensity distribution of scattered light for two perpendicular polarizations can be describe as,

$$I_1(\theta) = \left| \sum_{n=1}^{\infty} \frac{2n+1}{n(n+1)} [a_n \pi_n(\cos\theta) + b_n \tau_n(\cos\theta)] \right|^2, \tag{1.1.2}$$

$$I_2(\theta) = \left| \sum_{n=1}^{\infty} \frac{2n+1}{n(n+1)} [b_n \pi_n(\cos\theta) + a_n \tau_n(\cos\theta)] \right|^2, \tag{1.1.3}$$

where a_n and b_n are coefficients defined by the boundary conditions, and $\pi_n(\cos\theta)$ and $\tau_n(\cos\theta)$ are the Mie angular functions. The functions can be described as

$$\pi_n(\cos\theta) = \frac{1}{\sin\theta} P_n^1(\cos\theta), \tag{1.1.4}$$

$$\tau_n(\cos\theta) = \frac{d}{d\theta} P_n^1(\cos\theta), \tag{1.1.5}$$

where P_n^1 are associated Legendre polynomials of the first kind. In both cases, we can conclude that incident beam is deflected from its original propagation. A narrow incident beam will be scattered into a cone of beams with different directions. Aside from forward scattering, there is backscattering as well.

Based on the single particle model, we can derive more parameters to characterize the scattering of light by a single particle. One important parameter is the scattering anisotropy g [32],

$$g = < \cos(\theta) > , \tag{1.1.6}$$

where θ is the scattering angle. g describes the angular spread of light scattered off a particle. The values of g can range from -1 to 1, where a lower negative value indicates more backward scattering, while a higher positive value indicates more forward scattering. Another important parameter for a single scatterer is its

scattering cross section σ_s [mm^2]. σ_s indicates the particle's scattering capability. It can be thought of as the effective area that guarantees scattering when a photon impinges. σ_s is related to its geometric cross-sectional area A [mm^2] by the proportionality constant called the scattering efficiency Q_s [dimensionless], which is described as $\sigma_s = Q_s A$. Note that Q_s takes on a statistical nature and is not necessarily equal to the physical cross section area of the scatterer.

Scattering of a collection of particles

Based on the scattering model of a single scatterer, we expand our discussion to the scattering of a collection of homogeneous scatterers that are randomly distributed within a finite three-dimensional space. This is a simplified model of a real scattering medium. The scattering characteristics of the sample per unit length are described by the scattering coefficient μ_s [mm^{-1}] and the scattering mean free path (MFP) l_s [mm]:

$$\mu_s = \sigma_s N, \tag{1.1.7}$$

$$l_s = \frac{1}{\mu_s}, \tag{1.1.8}$$

where N is the number of scatterers per unit volume [mm^{-3}]. The scattering MFP is the average distance between scattering events. From l_s, we can derive the intensity of ballistic light after light travels a thickness of l through the sample [32],

$$I_b(l) = I_0 e^{-\frac{l}{l_s}} = I_0 e^{-\mu_s l}. \tag{1.1.9}$$

Eq. 1.1.9 only quantifies how many photons are scattered. It doesn't consider how much the photons have deviated from their original trajectory. For example, if $g \approx 1$ and a photon encounters many scattering events, the trajectory of the photon will still not deviate from its ballistic trajectory too much. In other words, the photon retains some "memory" of its original orientation. To eliminate this "memory", the anisotropy of the scatterers is incorporated to characterize the scattering sample by their reduced scattering coefficient μ_s' [mm^{-1}] or transport mean free path (TMFP) l_s' [mm], which are defined as,

$$\mu_s' = (1 - g)\mu_s, \tag{1.1.10}$$

$$l_s' = \frac{1}{\mu_s'}. \tag{1.1.11}$$

From the equations, we can tell μ_s' is a lumped property incorporating μ_s and g. By multiplying μ_s by a factor of $(1 - g)$, we convert the photon movement

with many small steps $1/\mu_s$ that involve only partial deflection to a random walk of step size $1/\mu_s'$. We can think of the TMFP as the mean distance after which a photon's direction becomes randomized. By the definition of MFP and TMFP, people divide light propagation in scattering media into four different regimes [32, 34, 35]. Within one MFP through a scattering media, ballistic photons are still dominant. This regime is called ballistic regime. In the region from the MFP to the TMFP, photons are scattered a few times but are just slightly deflected from their paths. This regime is called the quasi-ballistic regime. Between one and ten TMFPs, incident photons have been scattered many times but still retain some "memory" of their original directionality. This regime is called quasi-diffusive regime. Finally, beyond ten TMFPs, the directions of the scattered photons are barely related to its original directions. This regime is called diffusive regime. If you want to directly visualize the difference of scattering in different regimes, please refer to a schematic depiction from Vasilis Ntziachristos's paper [34].

The particle model described above is an inaccurate approximation for a real scattering medium. Consider the case of biological tissue for example. Its micro-structure is more complicated than smaller particles of the same identity suspended in a uniform environment. Biological tissues can have micro structures ranging from 0.01 μm for membranes to 10 μm for whole cells [32, 36]. The refractive indices of scatterers can also vary from 1.34-1.62 for different tissue components [32, 36]. Therefore, it is really difficult to solve the scattering of a real scattering medium through all the micro processes and then find a solution to counter its influence. However, the model we use is accurate enough when considering the scattering process at the macro scale, such as in estimating the portion of ballistic transmission and randomness of transmitted wavefront. We may have a chance to draw some useful conclusions from the macro-phenomena of scattering and then come to some useful tools by either resolving or utilizing scattering. This leads to the discussions in the following sections.

1.2 Macro-Phenomena of Scattering

Speckle

When a single optical mode is shone onto a scattering medium, light propagates diffusively within the scattering medium, as shown in Fig.1.2(a). The concept of optical mode will be discussed in the end of this section. For now, we can just take it as a beam that is perfectly monochromatic and as narrow as possible. After traveling beyond the diffusive regime, the output will be a spatially uncorrelated

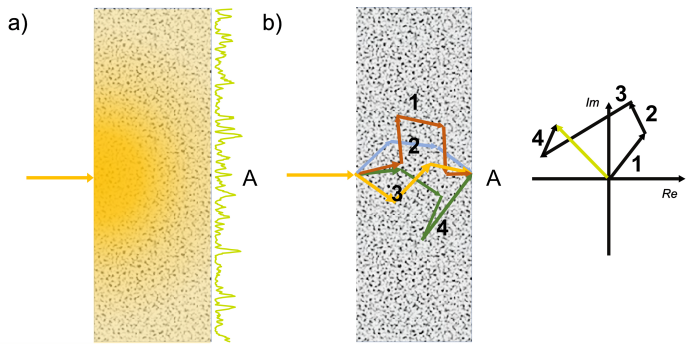

Figure 1.2: Schematic depiction of light's diffusive propagation and output wavefront through a scattering medium. (a) A perfectly monochromatic beam propagates through a scattering medium. (b) At an arbitrary point on the output wavefront, the electric field can be deemed as a summation of different beamlets.

wavefront. Initially, we limit attention to a single polarization state, since the same analysis will apply for the other polarization. At an arbitrary point A(x,y) on the output surface $z = z_{output}$, the output optical field is a summation of beamlets that encounter different scattering events, as shown in Fig. 1.2(b). Moreover, from the previous section we know that the scattering of each beamlet can be considered a random process. Thus, we can consider the output electric field of every beamlet at point A as a random variable $a_k(x, y)$ and the output electric field at point A, $E(x, y)$ can be described as summation of $a_k(x, y)$ in the complex plane as shown in Fig. 1.2(b),

$$E(x, y) = \sum_{k=1}^{N} a_k(x, y) = \sum_{k=1}^{N} |a_k(x, y)| e^{i\theta_k}, \tag{1.2.1}$$

where $|a_k(x, y)|$ and θ_k are the amplitude and phase of a_k, respectively. If we decompose $E(x, y)$ into the real and imaginary parts, we have

$$E(x, y) = \mathrm{Re}(E(x, y)) + i\,\mathrm{Im}(E(x, y)), \tag{1.2.2}$$

$$\mathrm{Re}(E(x, y)) = \sum_{k=1}^{N} |a_k(x, y)| \cos\theta_k, \tag{1.2.3}$$

$$\mathrm{Im}(E(x, y)) = \sum_{k=1}^{N} |a_k(x, y)| \sin\theta_k. \tag{1.2.4}$$

We know that $a_k(x, y)$ is generated by the incident beam with limited energy, so $|a_k(x, y)|$ should possess limited mean value and variance. Note that we have only shown four $a_k(x, y)$s that sum up at point A in Fig. 1.2(b). In fact, N is very large, considering the fact of diffusive propagation of light in the medium. Therefore,

we can apply the central limit theorem to Eqs.1.2.3 and 1.2.4, which simply means $\mathrm{Re}(E(x, y, z))$ and $\mathrm{Im}(E(x, y))$ follow a Gaussian distribution. By evaluating their first-order statistical properties, we can find out that the real and imaginary parts of the output field have zeros means, identical variances, and are uncorrelated. Supposing $\mathrm{Re}(E(x, y))$ follows a Gaussian distribution with zero mean and variance σ^2, the joint probability function of $\mathrm{Re}(E(x, y))$ and $\mathrm{Im}(E(x, y))$ is

$$p(\mathrm{Re}(E(x, y)), \mathrm{Im}(E(x, y))) = \frac{1}{2\pi\sigma^2} \exp\left(-\frac{[\mathrm{Re}(E(x, y))]^2 + [\mathrm{Im}(E(x, y))]^2}{2\sigma^2}\right). \tag{1.2.5}$$

Such a density function is commonly known as a circular Gaussian density function. Therefore, $E(x, y)$ can be referred to as a circular complex Gaussian random variable.

For the output wavefront, it is more straightforward to talk about its amplitude $|E(x, y)|$, intensity $I(x, y)$, and phase $\theta(x, y)$. We can apply the transformation of these random variables with reference to $\mathrm{Re}(E(x, y))$ and $\mathrm{Im}(E(x, y))$ as follows:

$$|E(x, y)| = \sqrt{[\mathrm{Re}(E(x, y)]^2 + [\mathrm{Im}(E(x, y)]^2}, \tag{1.2.6}$$

$$I(x, y) = [\mathrm{Re}(E(x, y)]^2 + [\mathrm{Im}(E(x, y)]^2, \tag{1.2.7}$$

$$\theta = Arg(\mathrm{Re}(E(x, y)) + i\,\mathrm{Im}(E(x, y))). \tag{1.2.8}$$

Then the probability density functions of $|E(x, y)|$, $I(x, y)$ and $\theta(x, y)$ are

$$p(|E(x, y)|) = \begin{cases} \frac{1}{\sigma^2} \exp\left(\frac{-|E(x,y)|^2}{2\sigma^2}\right) & \text{,if } |E(x, y)| \geq 0 \\ 0 & \text{,otherwise} \end{cases}, \tag{1.2.9}$$

$$p(I(x, y)) = \begin{cases} \frac{1}{2\sigma^2} \exp\left(\frac{-I(x,y)}{2\sigma^2}\right) & \text{,if } |I(x, y)| \geq 0 \\ 0 & \text{,otherwise} \end{cases}, \tag{1.2.10}$$

$$\text{and } p(\theta(x, y)) = \begin{cases} \frac{1}{2\pi} & \text{,if } -\pi \leq \theta(x, y) < \pi \\ 0 & \text{,otherwise} \end{cases}. \tag{1.2.11}$$

From the equations, we can conclude that the intensity of the output wavefront follows a negative exponential distribution, the amplitude follows a Rayleigh distribution, and the phase possesses a uniform distribution [37]. The phase and amplitude are independent. The statistics have been confirmed in experiment. Fig. 1.3(a) is an intensity pattern of a scattered wavefront we captured by a CCD sensor with an objective lens. We can tell the two-dimensional intensity distribution is a speckle pattern. A two-dimensional histogram of the amplitude and phase of speckle pattern is shown in Fig. 1.3(b), which matches the probability distribution of phase

and amplitude. Note that speckle is the smallest feature in a speckle pattern. The speckle size is defined by the diffraction limit $\frac{\lambda}{NA}$, where the numerical aperture NA is the sine of the maximum take-off angle of light on the output surface. By the Shannon's sampling theorem, within the half width of a speckle $\frac{\lambda}{2NA}$, the amplitude and phase can be deemed as uniform. An area of $(\frac{\lambda}{2NA})^2$ on the output surface can be treated as a single optical mode. This clarifies the definition of an optical mode at the beginning of this section. This is also why we can discretize a continuous wavefront into an array of discrete optical modes, which we will frequently use in the transmission matrix theory. A rigorous proof of wavefront discretization can be found in the supplementary material of reference [38].

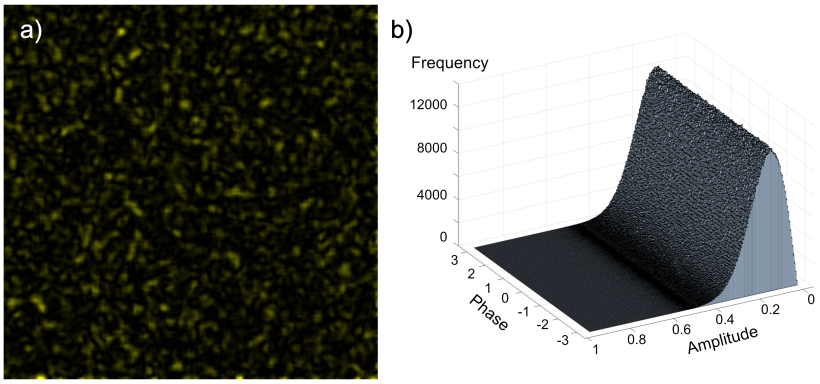

Figure 1.3: Statistics of the output scattering wavefront. (a) The spatial intensity pattern of the output scattering wavefront. (b) 2D histogram of the phase and amplitude of the output scattering wavefront.

The previous discussion was based on a single mode input. If we have a wide incident beam or multiple input modes, the conclusions still hold. Without loss of generality, let's suppose we have two input modes, their output wavefronts are $E_1(x, y)$ and $E_2(x, y)$. $\mathrm{Re}(E_1(x, y))$ and $\mathrm{Im}(E_1(x, y))$ follow a Gaussian distribution with zero mean and variance ${\sigma_1}^2$, while $\mathrm{Re}(E_2(x, y))$ and $\mathrm{Im}(E_2(x, y))$ follow a Gaussian distribution with zero mean and variance ${\sigma_2}^2$. If the incident beams are perfectly monochromatic, the output wavefront will be a coherent summation of $E_1(x, y)$ and $E_2(x, y)$. That is $E_{output}(x, y) = E_1(x, y) + E_2(x, y)$. If $E_1(x, y)$ and $E_2(x, y)$ are independent, $\mathrm{Re}(E_{output}(x, y))$ follows a Gaussian distribution with zero mean and variance ${\sigma_1}^2 + {\sigma_2}^2$ by calculating the probability density function of summation of independent random variables, as does $\mathrm{Im}(E_{output}(x, y))$. Going through the same derivation as the case of a single incident mode, we come to the same statistical properties for output wavefront from multiple input modes.

Transmission matrix theory

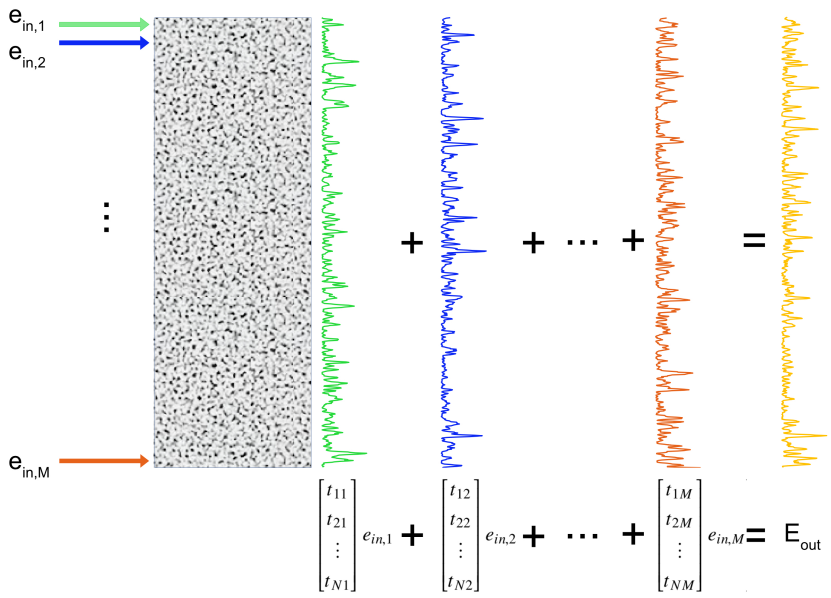

Figure 1.4: The output of a incident input wavefront can be deemed as the summation of the output wavefronts of every single input mode, as discussed in the previous section. The conclusion can also be expressed by the transmission matrix theorem as shown in Eq. 1.2.14.

If we treat the process through which light propagates inside the scattering media as a linear lossless process of the optical field and look at the input and output wavefronts, we can describe scattering as a linear transform between the two [39–41]. Based on the discussion in the speckle section, the input and output wavefronts can be discretized as elementwise arrays of optical modes. Suppose array E_{in} and array E_{out} represent the input and output wavefront and have M and N elements, respectively. Every element of E_{in} and E_{out} is the complex value of the corresponding optical mode. The transform can be represented by a N by M transmission matrix $T_{in\to out}$, which describes how the phase and amplitude of the input field is modified by the medium and presented on the output plane. Its mathematical representation is [40]

$$E_{out} = T_{in\to out} E_{in}. \tag{1.2.12}$$

To be more clear, an elementwise expression of Eq. 1.2.12 is

$$\begin{bmatrix} t_{11} & t_{12} & \dots & t_{1M} \\ t_{21} & t_{22} & \dots & t_{2M} \\ \vdots & \vdots & \ddots & \vdots \\ t_{N1} & t_{N2} & \dots & t_{NM} \end{bmatrix} \begin{bmatrix} e_{in,1} \\ e_{in,2} \\ \vdots \\ e_{in,M} \end{bmatrix} = \begin{bmatrix} t_{11}e_{in,1} + t_{12}e_{in,2} + \cdots + t_{1M}e_{in,M} \\ t_{21}e_{in,1} + t_{22}e_{in,2} + \cdots + t_{2M}e_{in,M} \\ \vdots \\ t_{N1}e_{in,1} + t_{N2}e_{in,2} + \cdots + t_{NM}e_{in,M} \end{bmatrix} = \begin{bmatrix} e_{out,1} \\ e_{out,2} \\ \vdots \\ e_{out,N} \end{bmatrix}, \tag{1.2.13}$$

where $e_{in,k}$ and $e_{out,k}$ are the kth element in array E_{in} and E_{out}, respectively and t_{ij} is the element at the ith row and jth column of the transmission matrix $T_{in\to out}$. If we take a close look at the terms on the left and right of the second equal sign in Eq. 1.2.13, we can rewrite the equation as

$$E_{out} = \left[\begin{bmatrix} t_{11} \\ t_{21} \\ \vdots \\ t_{N1} \end{bmatrix} e_{in,1} + \begin{bmatrix} t_{12} \\ t_{22} \\ \vdots \\ t_{N2} \end{bmatrix} e_{in,2} + \cdots + \begin{bmatrix} t_{1M} \\ t_{2M} \\ \vdots \\ t_{NM} \end{bmatrix} e_{in,M} \right], \tag{1.2.14}$$

which simply means that the output optical field is the summation of every individual output of a single input optical mode. A schematic demonstration is shown Fig. 1.4. In the previous section, we derived the statistics of the output wavefront of a single input mode. In transmission matrix theorem, for a defined input mode $e_{in,j}$, its output wavefront is described as an array $[t_{1j}e_{in,j}, t_{2p}e_{in,j}, \dots, t_{Nj}e_{in,j}]$. So that, $t_{k,j}e_{in,j}$ should follow the circular Gaussian distribution due to its statistical property. For a definite j, $e_{in,j}$ is a complex constant, so it is t_{ij} that possess a circular Gaussian distribution. In other words, every element in the same column of the transmission matrix follows a circular Gaussian distribution. If every column of the transmission matrix is independent, then every element t_{ij} in the transmission matrix $T_{in\to out}$ follows a circular Gaussian distribution. Generating a random matrix with circular Gaussian distributed elements is usually how people simulate a scattering medium. Transmission matrix theory is widely used in the analysis of wavefront shaping and phase conjugation. We will see more derivations based on this in the following sections.

Memory effect

In the previous section, we modeled the scattering as a transmission matrix. For a real scattering medium, its transmission matrix can have an additional macroscopic structure, either correlation in spatial domain or Fourier domain, depending on its scattering property. Memory effect is the manifestation of correlations in the

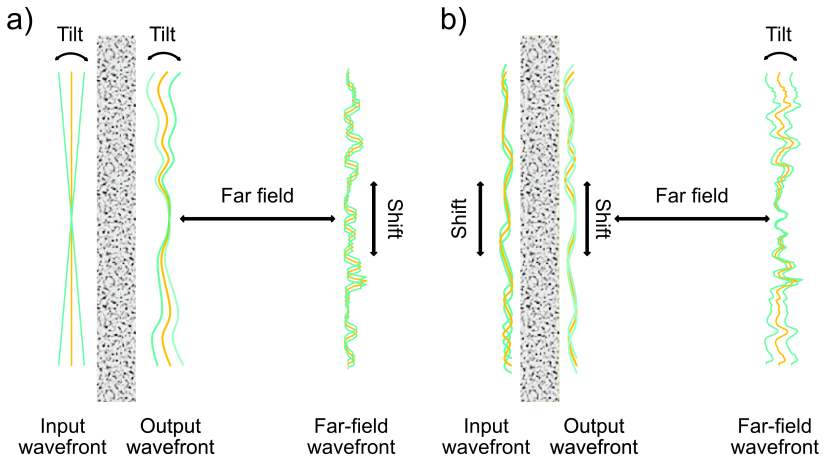

Figure 1.5: Schematic depiction of two types of memory effects. (a) Traditional memory effect. (b) Translational memory effect.

transmission matrix. Up to date, two types of memory effects have been discovered. They are the traditional memory effect [42, 43] and the translational memory effect [38], respectively.

The traditional memory effect for a general scalar wave was first derived theoretically in 1988 [42]. It was verified experimentally for optical waves in the same year [43]. The traditional memory effect describes the following phenomenon: when an input wavefront reaching a diffusing sample is titled within a certain angular range, the output wavefront is equally tilted, resulting in a spatial shift of the speckle pattern at far filed, as shown in Fig 1.5(a). The distance within which this property holds is called the memory effect region (MER). It can be approximated by the equation [38],

$$MER \approx \frac{v\lambda}{\pi L}, \tag{1.2.15}$$

where v is the distance from the output plane of the scattering medium to the screen, λ is the wavelength of the light source and L is the thickness of the scattering medium. From the equation, the MER is inversely proportional to the thickness of the scattering media. For useful applications, it requires the scattering medium to be thin. Moreover, it requires a distance of far-field propagation to realize the shift of the output wavefront. The conjugate planes of the tilt-and-shift relation is the input surface and the far-field plane. If we think inversely of the phenomenon, a point source within the MER will generate a random speckle pattern through the scattering medium. When we shift the point source, the speckle pattern will also

shift at far field. If we treat the speckle pattern as a point spread function (PSF), the PSF will be shift-invariant within the MER, which is similar to the scenario in a traditional lens based imaging system. People have demonstrated direct image transfer and computational image recovery based on the traditional memory effect. We will see some related work we have done in Chapter 5.

The translational memory effect was first reported in 2015 [38]. It is a complementary type of memory effect to the traditional one. It describes the following phenomenon: when an input wavefront reaching an anisotropically scattering medium is shifted within a certain distance, the output wavefront is equally shifted, resulting in the tilting of far-filed wavefront, as shown in Fig. 1.5(b). The translational memory effect applies for thick and highly forward scattering media, such as biological samples. Different from the traditional memory effect, its shift-invariant PSF region is on the output surface the scattering medium, which has important implication for biomedical imaging and adaptive optics.

There are also many other macro-phenomena discovered on optical scattering, such as the shower-curtain effect [44–46] and Anderson localization [47–49]. We will not talk about them in detail.

1.3 The Problem of Scattering

As briefly discussed in the abstract, scattering is a major challenge for optical focusing and imaging. In this section, we will analyze three effects that hinder optical focusing and imaging through scattering media, which are wavefront aberrations, glare, and decorrelation.

Wavefront aberration

Wavefront aberrations originate from the diffusive propagation of forward-scattering light through scattering media. They are the differences between the scattered wavefront and the wavefront intended to present through a scattering medium. Wavefront aberrations induced by scattering are different from the wavefront aberration in a lens system [50, 51]. First, it cannot be predicted by the geometrical setup such as aperture size, propagation distance, and lens shape [52]. Second, the order of scattering wavefront aberration is very high, considering the fact that the output wavefront is made up of diffraction limited speckles. As such, the aberrations cannot be compensated by traditional lens design. As shown in Fig. 1.6(a), a collimated beam is focused on the focal plane by a lens in free space. However, if we applied the same strategy in the presence of a scattering medium, the outcome will be a speckle

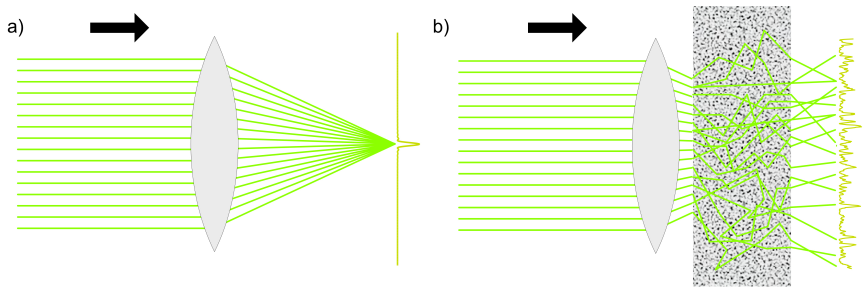

Figure 1.6: Schematic depiction of problem of scattering for focusing light through a scattering medium. (a) Optical focusing can be easily realized by a lens in free space. (b) Scattering media leads to a diffusive propagation, which results in a random output wavefront.

field on the focal plane. Based on the statistical property of speckle pattern, light intensity is not well confined to a small region so that it lost its spatial selectivity. For imaging, conventional imaging systems relies on lenses and mirrors to transform light from a point on the object plane to a point on the image plane [53, 54]. If there is a scattering medium in front of the object, the PSF will spread out as a speckle field. The point-to-point conjugate relationship between the object and image is broken by the wavefront aberrations. Therefore, conventional optical methods will fail when they are applied to imaging through scattering media.

Glare

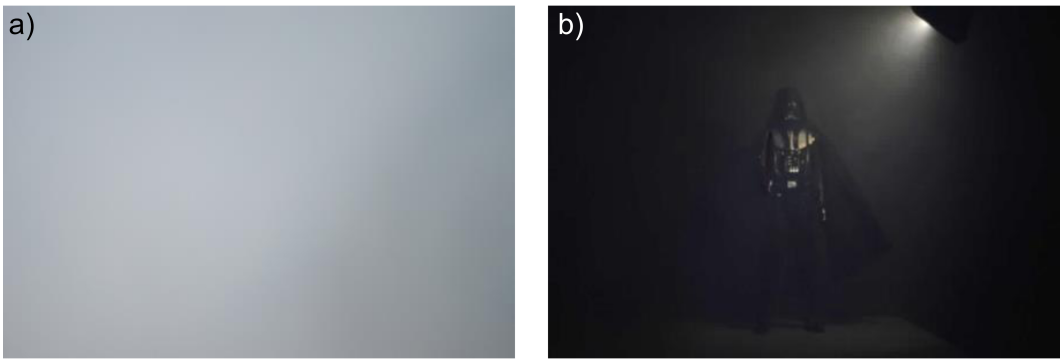

Figure 1.7: Experimental demonstration of issue brought by glare. (a) shows the captured camera image with a reflective illumination. The glare from the light source prevents us from seeing the target. (b) shows a captured image where the figurine is locally illuminated.

Glare is the undesired backward-scattering light when we illuminate a scattering

sample [55, 56]. It impacts imaging more than focusing. When we try to image a target through a scattering medium, in most cases such as remote imaging in fog, haze, and sandstorm, we don't have access to the other side of the scattering media. Therefore, a reflective illumination setup has to be adopted over trans-illumination, which means the light source and the detector are on the same side with reference to the sample. In the reflective illumination scenario, light first propagates through the scattering medium before illuminating the target. The glare from the illumination source impinging on the scattering medium can mask the reflections from a weak distant target [57–59]. An experimental demonstration is shown in Fig. 1.7. This brief experiment illustrates the issue: glare can significantly reduce our ability to image or probe into scattering media. Here we point both a camera and a spotlight at a fog bank (generated by a fog machine). A figurine is on the other side of this fog bank. Fig. 1.7(a) shows the captured camera image with the spotlight illumination. The glare from the spotlight prevents us from seeing the figurine. Fig. 1.7(b) shows a captured image where the figurine is locally illuminated. Despite the slight blurring introduced by scattering from the fog, we can readily discern the figurine. The more challenging part is that the glare wavefront generated by a coherent light source is a speckle field with severe intensity variance. Even if an incoherent light source is used, the glare will still show up as an uneven noise term, as we can see from Fig. 1.7(a). Moreover, if the glare intensity is too high, its shot noise will overwhelm the signal. Glare as a strong background cannot be easily removed by simple digital signal processing such as background subtraction and contrast enhancement. Physical methods are required to suppress the glare or separate it from the target reflection.

Decorrelation

All the previous discussion is based on a static scattering media. However, many scattering media we frequently deal with are dynamic, whose micro structure or composition is changing over time. For example, living biological tissues can have blood cells moving continuously in the vessel. The refractive indices of cytoplasm in cells will also vary based on metabolism. Fog is made up of small droplets of water in the condensed phase. The water droplets are kept in the air by thermal Brownian motion. All of these micro changes will accumulate and lead to a time-varying output wavefront when we shine a coherent beam through the sample[60–63]. The change of the output wavefront can be described as a decorrelation process and characterized by its intensity autocorrelation function based on the diffusing-wave

spectroscopy [64]. Suppose the mean intensities of speckle patterns at different times are the same, then the autocorrelation function can be written as [65, 66]

$$g_2(\tau) = \frac{< I(x, y, t_0) I(x, y, t_0 + \tau) >_{x,y}}{< I(x, y) >_{x,y}^2} - 1, \tag{1.3.1}$$

where $< >_{x,y}$ represents the ensemble-average in the capture plane, $I(x, y, t)$ is the speckle pattern at time t, and τ is the time interval. According to the assumption, $< I(x, y) >_{x,y} = < I(x, y, t_0)_{x,y} > = < I(x, y, t_0 + \tau)_{x,y} >$. $g_2(\tau)$ is the correlation factor. From the statistics of speckle, we know that $g_2(\tau)$ can range from 0 to 1,

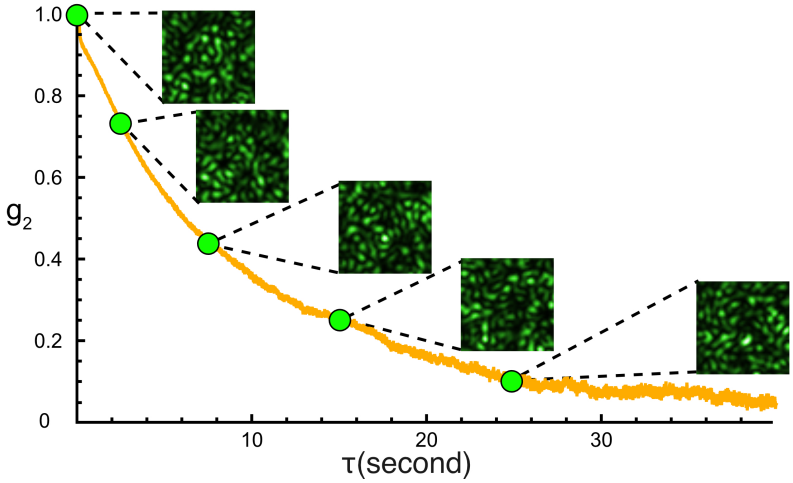

Figure 1.8: Measured decorrelation curve of a 1 mm thick rat brain tissue.

which corresponds the change of correlation. Then the speed of decorrelation can be describe as $\Delta g_2/\tau$. However, as shown in Fig. 1.8, the decorrelation process doesn't always follow a linear fashion. Fig.1.8 is an example of a decorrelation curve measured in experiment. Therefore, decorrelation time is more commonly used to describe how fast a tissue decorrelates. It is the time interval τ after which the $g_2(\tau)$ autocorrelation factor decays to a pre-determined value, typically $1/e^2$, $1/e$ [66–71]. If we choose $1/e^2$ as a standard, for example, the decorrelation time τ_{1/e^2} for the dorsal skin of a living mouse with 1.5 mm thickness can be shorter than 50 ms [66, 69].

Decorrelation poses a challenge for the techniques that work under the assumption that scattering is static. For example, wavefront shaping technique is a novel technique that can focus light through scattering media, which we are going to introduce in the following section. However, decorrelation will disrupt the focus by changing the transmission matrix [66]. The general solution is to speed up the system and

keep its response time shorter than the decorrelation time, which we will discuss detailedly in Chapter 3.

1.4 Methods for Optical Focusing and Imaging through Scattering Media

In this section, we will give a brief review on the techniques to realize optical focusing and imaging through scattering media. The discussion will focus on the concepts and principles. First, we will talk about wavefront shaping, a novel method that enables optical focusing through scattering media. Then, we will go through different methods people use to realize imaging through scattering media. Finally, we will introduce techniques for glare suppression.

Wavefront shaping

Although focusing through scattering media has long been considered impossible, recent developments in wavefront shaping (WFS) have changed this view. The basic principle behind WFS is rooted in the transmission matrix theory. Let's first take a back look on Eq. 1.2.14:

$$\begin{bmatrix} e_{out,1} \\ e_{out,2} \\ \vdots \\ e_{out,N} \end{bmatrix} = \left[\begin{bmatrix} t_{11} \\ t_{21} \\ \vdots \\ t_{N1} \end{bmatrix} e_{in,1} + \begin{bmatrix} t_{12} \\ t_{22} \\ \vdots \\ t_{N2} \end{bmatrix} e_{in,2} + \cdots + \begin{bmatrix} t_{1M} \\ t_{2M} \\ \vdots \\ t_{NM} \end{bmatrix} e_{in,M} \right].$$

For a single output mode $e_{out,1}$, we have

$$e_{out,1} = t_{11}e_{in,1} + t_{12}e_{in,2} + \cdots + t_{1M}e_{in,M} = \sum_{k=1}^{N} t_{1k}e_{in,k}. \tag{1.4.1}$$

When the input is a plane wave, $e_{in,k}$ is identical for $k \in [1, M]$. $t_{1k}e_{in,k}$ is out of phase for different k, resulting in $e_{out,1}$ as a speckle. If we can control the phase of $e_{in,k}$ and set $\arg(e_{in,k}) = -\arg(t_{1k})$, we can line $t_{1k}e_{in,k}$s up in the complex plane, as shown in Fig. 1.9(b). Let $e'_{out,1}$ be the output after we optimize the phase of each input mode, then $|e'_{out,1}|$can be expressed as

$$|e'_{out,1}| = \sum_{k=1}^{N} \left| |t_{1k}|e^{\arg(t_{1k})}|e_{in,k}|e^{\arg(e_{in,k})} \right| = \sum_{k=1}^{M} |t_{1k}||e_{in,k}|. \tag{1.4.2}$$

Comparing to its modulus before the optimization, $|e_{out,1}|$, which is

$$|e_{out,1}| = |\sum_{k=1}^{M} t_{1k}e_{in,k}|, \tag{1.4.3}$$

we can derive the intensity enhancement factor η as

$$\eta = \frac{< |e'_{out,1}|^2 >}{< |e_{out,1}|^2 >} = \frac{\left\langle \left| \sum_{k=1}^{M} |t_{1k}||e_{in,k}| \right|^2 \right\rangle}{\left\langle | \sum_{k=1}^{M} t_{1k} e_{in,k}|^2 \right\rangle} = \frac{\left\langle \left| \sum_{k=1}^{M} |t_{1k}| \right|^2 \right\rangle}{\left\langle | \sum_{k=1}^{M} t_{1k}|^2 \right\rangle}. \tag{1.4.4}$$

Then we try to figure out the intensity of unoptimized modes (the background), it can be proved that their mean intensity before and after optimization are nearly the same, when M is much greater than N [35, 40]. $< |e_{out,1}|^2 >$ is equal to the background before optimization, so $< |e_{out,1}|^2 >$ can approximate the background after optimization as well. Therefore, η is also the signal to background ratio or peak to background ratio (PBR) after WFS. From the statistics of a transmission matrix,

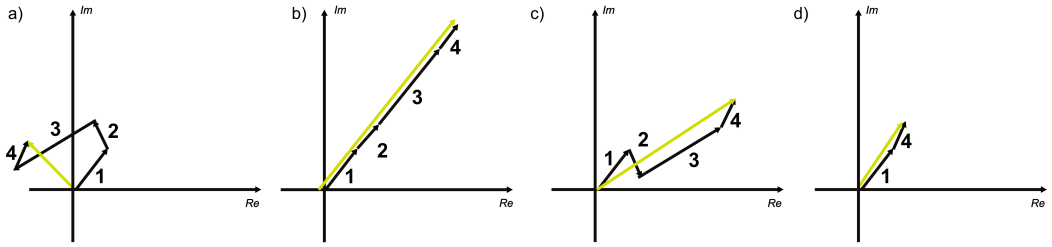

Figure 1.9: Schematic depiction of different modulation strategies. (a) Original unmodulated phasors out of phase. (b) Phase modulation. (c) Binary phase modulation. (d) Binary amplitude modulation.

we know that t_{1k} follows circular Gaussian distribution, then we can find $\eta = \frac{\pi}{4}M$. If we want to enhance the intensity in multiple output modes, going through the same calculation, we find that $\eta = \frac{\pi}{4}\frac{M}{N}$, where N is the number output modes to optimize. If we "shape" the input wavefront, we can focus light to a small region through scattering media.

The modulation of input modes can be relaxed to binary phase modulation or binary amplitude modulation in different experimental scenarios, which will still lead to an enhancement in the target output modes as shown in Fig.1.9(c) and (d). Fig.1.9(c) depicts the method by which binary phase modulation enhances the target output mode. If we shift the phase of phasor 2 and 3 by π, then all the output modes are partially lined up. In contrast, for binary amplitude modulation, we switch off all the input modes that negatively contribute to the the target output mode intensity. As shown in in Fig. 1.9(d), we turned off phasor 2 and 3 and only used phasor 1 and 4. Going through the same calculation of enhancement factor as in Eq. 1.4.4, we

can summarize η for different modulation strategies as follows:

$$\begin{aligned} \eta_{phase\ modulation} &= \frac{\pi}{4}\frac{M}{N}, \\ \eta_{binary\ phase} &= \frac{1}{\pi}\frac{M}{N}, \\ \eta_{binary\ amplitude} &= \frac{1}{2\pi}\frac{M}{N}, \end{aligned} \tag{1.4.5}$$

where M is the number of controllable input modes, and N is the number of output modes to optimize. Chapter 3 is an example of application of binary amplitude modulation, a more detailed discussion on this strategy can be found in the principle section.

Thanks to the development of modern electronics technology, a spatial light modulator (SLM) can be used to shape the wavefront in practice. An SLM could be either a LCOS-SLM (liquid crystal on silicon-Spatial Light Modulator), a ferroelectric LC-SLM (liquid crystal-spatial light modulator) or a DMD (digital micromirror device), which can realize phase modulation, binary phase modulation or binary amplitude modulation, respectively. Then the question comes to how to find out the correct input wavefront. In general, the correct wavefront can be obtained by iterative optimization [72–80], measuring the transmission matrix [81–85] or by phase conjugation [86–95]. Iterative optimization requires a feedback signal that quantifies how much intensity is focused on the target modes. The feedback signal can be fluorescent light from a probe particle [72–74], photoacoustic wave [75, 76], ultrasound [77], second-harmonic generation [78], two-photon or multi-photon excitation [79, 80] or light intensity in the corresponding modes measured by a photodetector [40]. Iterative methods inherently suffers from a relatively long time of convergence, since the solution is found through trial and error. Transmission matrix measurement [81–85] can be deemed as an extension of iteration optimization. It is equivalent to figuring out the optimum input wavefront to all the output modes of interest. Transmission matrix measurement figures out the transmission matrix by measuring the output wavefronts with the pre-knowledge of corresponding input wavefronts. We can expect that transmission matrix measurement is even more time-consuming than iterative optimization. Moreover, in most situations of application, it requires direct access to the output plane.

Phase conjugation will be detailedly discussed in chapter 2 and 3. Here, we just give a brief introduction to the principle. Phase conjugation describes the reciprocity of light propagation in a linear and lossless medium [96, 97]: the phase conjugate

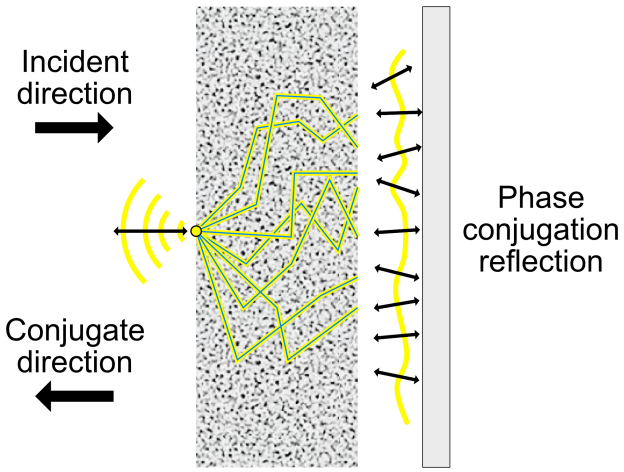

Figure 1.10: Schematic depiction of phase conjugation

reflection of a wavefront is a "time-reversed" replica of the wavefront's electric field. As shown in Fig.1.10, if we place a point source at the target mode, then light will propagate through the scattering medium and generate an output wavefront. At the output plane, if the wavefront is reflected off the output plane with a conjugate phase, scattered light will retrace their propagation and result in light focusing back at the target mode, as if time is reversed. From the process of phase conjugation, we know that, if we can have a focus at the target mode, the correct input wavefront for WFS can be easily figured out by measuring the wavefront coming out of the scattering media and conjugating the measured phase. However, the requirement to originally have a focus at the target mode where we aim to focus defeats the purpose of WFS. A way around this problem is to phase conjugate light from a guide star [98]. A guide star could be a small fluorescent particle [88] or a second harmonic generating particle [86] embedded in the scattering media. An alternative approach is to use ultrasound tagging to create a virtual guide star [67, 87, 89]. However, these guide stars all have their limits and disadvantages in application. For example, it is difficult to place small particles to a designated position without direct access to the target plane. For ultrasound tagging, the tagged photons are only a small portion compared to the total number of photons sent in, which may lead to a small signal to background ratio in the captured wavefront. Therefore, more noninvasive guide stars with better control and higher efficiency are still waiting to be discovered.

Methods for imaging through scattering media

Generally speaking, three approaches can be used to realize imaging through scattering media in the diffusive regime. The first is to scan the focus obtained by WFS. From the discussion in the previous section, we know a tight focus can be formed through scattering media by WFS. If the WFS technique used, like TRUE technique [67, 87], has ability to select an arbitrary mode through the scattering media, then we are able to scan the focus over the object. Scanning can also be realized with the assistant of memory effect [99], but it has limitation in the thickness of the scattering media and scanning range. Moreover, the object has to be placed at a distance behind the scattering media. Focus scanning approaches also require the signal generated by the object to be distinguished by the detector from the input light. Therefore, existing demonstration is limited to a fluorescent [67] or second harmonic generating [99] object.

The second approach is measuring the transmission matrix [81, 100]. As aforementioned in the transmission matrix section, transmission matrix describes the transform between input wavefront and output wavefront. In an imaging scenario, the input wavefront is the optical field to be found from the object, while output wavefront can be obtained from measurement. If we know the transmission matrix, then the object can be figured out by solving the inverse problem of the transform. As discussed in the WFS section, it is difficult to acquire the pre-knowledge of transmission matrix without access to the object plane. This approach shares the same limit with transmission matrix measurement in WFS. The third approach is the speckle-correlation-based imaging (SCI) [79, 101, 102], which we will discuss in detail in chapter 5. In general, optical imaging through scattering media still has a long way to go for application.

Methods for glare suppression

The optical field associated with glare and the reflected optical field from a remote target is different in an important way. Specifically, the glare components generally have a shorter optical path from source to detector. In principle, glare suppression can be performed using time-of-flight (TOF) methods [103–106] with the help of fast imaging systems, such as intensified charge-coupled device (ICCD) [107]. A TOF method would discard glare photons by binning the arriving light based on arrival time. Unfortunately, the requisite devices are very costly and, worse, tend to have very finite operating lifetime. There are some interesting developments in the use of modulated illumination and post-detection processing to achieve TOF

gating electronically [108]. One limitation for these methods is that they need to contend with glare associated noise, as the glare is not suppression prior to detection. Methods such as light detection and ranging (LIDAR) [109] can detect targets occluded by glare by coherently gated (CG) detection of light that have travelled a specific path length (or path length range). CG methods have a target range limitation—targets beyond the coherence length of the light source cannot be detected [110]. You will find more discussions on various glare suppression techniques in chapter 5. In general, there is not a comprehensive solution for glare suppression, as you can feel on the road when driving in a foggy day.

1.5 Outline of This Thesis

In this thesis, we will explore solutions to the problem of scattering from different aspects. Chapter 2 and 3 will aim on optical focusing through scattering media, while chapter 4 and 5 aim on imaging. Chapter 2 talks about Time Reversal by Analysis of Changing wavefronts from Kinetic targets (TRACK) technique. We will show that the motion of object can be incorporated as a guide star in phase conjugation. We will demonstrate that by taking the difference between time-varying scattering fields caused by a moving object and applying optical phase conjugation, light can be focused back to the location previously occupied by the object. Chapter 3 tackles the decorrelation problem in wavefront shaping. We will talk about our strategies to speed up a DOPC system and demonstrate that our system is fast enough to focus light through 2.3mm-thick living mouse skin, which has a potential to transfer wavefront shaping to *in vivo* applications. Chapter 4 introduces a glare suppression method based on destructive interference. We will show an optical analogue to noise canceling headphones and some experimental results in imaging through strongly backscattering media. Finally, in chapter 5, we will demonstrate a method to image a moving target through scattering media noninvasively. Its principle roots are in the speckle-correlation-based imaging (SCI) invented by Ori Katz. We will talk about how we improved the technique and extended its application to a bright field imaging scenario.

References

[1] Max Born and Emil Wolf. *Principles of optics: electromagnetic theory of propagation, interference and diffraction of light*. Elsevier, 1980.

[2] BJ Lin. *Optical methods for fine line lithography*. Elsevier, North Holland, 1980.

[3] Marc D Levenson, NS Viswanathan, and Robert A Simpson. "Improving resolution in photolithography with a phase-shifting mask". In: *IEEE Transactions on electron devices* 29.12 (1982), pp. 1828–1836.

[4] Thomas J Dougherty et al. "Photodynamic therapy". In: *Journal of the National Cancer Institute* 90.12 (1998), pp. 889–905.

[5] Graham CR Ellis-Davies. "Caged compounds: photorelease technology for control of cellular chemistry and physiology". In: *Nature methods* 4.8 (2007), pp. 619–628.

[6] Karl Deisseroth. "Optogenetics". In: *Nature methods* 8.1 (2011), pp. 26–29.

[7] Ofer Yizhar et al. "Optogenetics in neural systems". In: *Neuron* 71.1 (2011), pp. 9–34.

[8] Sylvie Hénon et al. "A new determination of the shear modulus of the human erythrocyte membrane using optical tweezers". In: *Biophysical journal* 76.2 (1999), pp. 1145–1151.

[9] JP Mills et al. "Nonlinear elastic and viscoelastic deformation of the human red blood cell with optical tweezers". In: *MCB-TECH SCIENCE PRESS*- 1 (2004), pp. 169–180.

[10] Mark C Pierce, David J Javier, and Rebecca Richards-Kortum. "Optical contrast agents and imaging systems for detection and diagnosis of cancer". In: *International journal of cancer* 123.9 (2008), pp. 1979–1990.

[11] Jerome Mertz. *Introduction to optical microscopy*. Vol. 138. CSIRO, 2010.

[12] Stefan W Hell and Jan Wichmann. "Breaking the diffraction resolution limit by stimulated emission: stimulated-emission-depletion fluorescence microscopy". In: *Optics letters* 19.11 (1994), pp. 780–782.

[13] Mats GL Gustafsson. "Nonlinear structured-illumination microscopy: wide-field fluorescence imaging with theoretically unlimited resolution". In: *Proceedings of the National Academy of Sciences of the United States of America* 102.37 (2005), pp. 13081–13086.

[14] Michael J Rust, Mark Bates, and Xiaowei Zhuang. "Sub-diffraction-limit imaging by stochastic optical reconstruction microscopy (STORM)". In: *Nature methods* 3.10 (2006), pp. 793–796.

[15] Eric Betzig et al. "Imaging intracellular fluorescent proteins at nanometer resolution". In: *Science* 313.5793 (2006), pp. 1642–1645.

[16] Dong Li et al. “Extended-resolution structured illumination imaging of endocytic and cytoskeletal dynamics”. In: *Science* 349.6251 (2015), aab3500.

[17] Joseph Goldstein et al. *Scanning electron microscopy and X-ray microanalysis: a text for biologists, materials scientists, and geologists*. Springer Science & Business Media, 2012.

[18] Yasushi Inouye and Satoshi Kawata. “Near-field scanning optical microscope with a metallic probe tip”. In: *Optics letters* 19.3 (1994), pp. 159–161.

[19] Bert Hecht et al. “Scanning near-field optical microscopy with aperture probes: Fundamentals and applications”. In: *The Journal of Chemical Physics* 112.18 (2000), pp. 7761–7774.

[20] E Hecht. “Optics 4th edition by Eugene Hecht Reading”. In: *MA: Addison-Wesley Publishing Company* 1 (2001), p. 2001.

[21] Derek Albert Long and DA Long. *Raman spectroscopy*. McGraw-Hill New York, 1977.

[22] Mildred S Dresselhaus et al. “Raman spectroscopy of carbon nanotubes”. In: *Physics reports* 409.2 (2005), pp. 47–99.

[23] LM Malard et al. “Raman spectroscopy in graphene”. In: *Physics Reports* 473.5 (2009), pp. 51–87.

[24] Norman Colthup. *Introduction to infrared and Raman spectroscopy*. Elsevier, 2012.

[25] Andrew Weiner. *Ultrafast optics*. Vol. 72. John Wiley & Sons, 2011.

[26] Graham Fleming. “Chemical applications of ultrafast spectroscopy”. In: (1986).

[27] Jagdeep Shah. *Ultrafast spectroscopy of semiconductors and semiconductor nanostructures*. Vol. 115. Springer Science & Business Media, 2013.

[28] Liang Gao et al. “Single-shot compressed ultrafast photography at one hundred billion frames per second”. In: *Nature* 516.7529 (2014), pp. 74–77.

[29] *Mie Scattering and Rayleigh Scattering*. `http://hyperphysics.phy-astr.gsu.edu/hbase/atmos/blusky.html`. Accessed: 2017-04-10.

[30] Hendrik Christoffel Van de Hulst and V Twersky. “Light scattering by small particles”. In: *Physics Today* 10.12 (1957), pp. 28–30.

[31] Craig F Bohren and Donald R Huffman. *Absorption and scattering of light by small particles*. John Wiley & Sons, 2008.

[32] Lihong V Wang and Hsin-i Wu. *Biomedical optics: principles and imaging*. John Wiley & Sons, 2012.

[33] *Mie Scattering Calculator*. `http://omlc.org/calc/mie_calc.html`. Accessed: 2017-04-10.

[34] Vasilis Ntziachristos. "Going deeper than microscopy: the optical imaging frontier in biology". In: *Nature methods* 7.8 (2010), pp. 603–614.

[35] Ying Min Wang. "Deep tissue fluorescence imaging with time-reversed light". PhD thesis. California Institute of Technology, 2013.

[36] Steven L Jacques. "Optical properties of biological tissues: a review". In: *Physics in medicine and biology* 58.11 (2013), R37.

[37] Joseph W Goodman. *Speckle phenomena in optics: theory and applications*. Roberts and Company Publishers, 2007.

[38] Benjamin Judkewitz et al. "Translation correlations in anisotropically scattering media". In: *Nature physics* 11.8 (2015), pp. 684–689.

[39] Carlo WJ Beenakker. "Random-matrix theory of quantum transport". In: *Reviews of modern physics* 69.3 (1997), p. 731.

[40] Ivo Micha Vellekoop. "Controlling the propagation of light in disordered scattering media". In: *arXiv preprint arXiv:0807.1087* (2008).

[41] Dietrich Marcuse. "Light transmission optics". In: (1972).

[42] Shechao Feng et al. "Correlations and fluctuations of coherent wave transmission through disordered media". In: *Physical review letters* 61.7 (1988), p. 834.

[43] Isaac Freund, Michael Rosenbluh, and Shechao Feng. "Memory effects in propagation of optical waves through disordered media". In: *Physical review letters* 61.20 (1988), p. 2328.

[44] Itai Dror, Arnon Sandrov, and Norman S Kopeika. "Experimental investigation of the influence of the relative position of the scattering layer on image quality: the shower curtain effect". In: *Applied optics* 37.27 (1998), pp. 6495–6499.

[45] Eitan Edrei and Giuliano Scarcelli. "Optical imaging through dynamic turbid media using the Fourier-domain shower-curtain effect". In: *Optica* 3.1 (2016), pp. 71–74.

[46] Gregoire Tremblay, Robert Bernier, and Gilles Roy. "The shower curtain effect paradoxes". In: *SPIE Remote Sensing*. International Society for Optics and Photonics. 2015, pp. 964107–964107.

[47] Diederik S Wiersma et al. "Localization of light in a disordered medium". In: *Nature* 390.6661 (1997), pp. 671–673.

[48] Tal Schwartz et al. "Transport and Anderson localization in disordered two-dimensional photonic lattices". In: *Nature* 446.7131 (2007), pp. 52–55.

[49] Mordechai Segev, Yaron Silberberg, and Demetrios N Christodoulides. "Anderson localization of light". In: *Nature Photonics* 7.3 (2013), pp. 197–204.

[50] Virendra N Mahajan. "Zernike circle polynomials and optical aberrations of systems with circular pupils". In: *Applied optics* 33.34 (1994), pp. 8121–8124.

[51] James C Wyant and Katherine Creath. "Basic wavefront aberration theory for optical metrology". In: *Applied optics and optical engineering* 11.s 29 (1992), p. 2.

[52] Robert Edward Fischer et al. *Optical system design*. Citeseer, 2000.

[53] Kurt Rossmann. "Point spread-function, line spread-function, and modulation transfer function: Tools for the study of imaging systems 1". In: *Radiology* 93.2 (1969), pp. 257–272.

[54] Glenn D Boreman. *Modulation transfer function in optical and electro-optical systems*. Vol. 21. SPIE press Bellingham, WA, 2001.

[55] Maths Abrahamsson and J Sjöstrand. "Impairment of contrast sensitivity function (CSF) as a measure of disability glare." In: *Investigative ophthalmology & visual science* 27.7 (1986), pp. 1131–1136.

[56] Aldo Badano and Michael J Flynn. "Image degradation by glare in radiologic display devices". In: *Medical Imaging 1997*. International Society for Optics and Photonics. 1997, pp. 222–231.

[57] David B Rensch and RK Long. "Comparative studies of extinction and backscattering by aerosols, fog, and rain at 10.6 μ and 0.63 μ". In: *Applied Optics* 9.7 (1970), pp. 1563–1573.

[58] Ronald TH Collis et al. *Visibility Measurement for Aircraft Landing Operations.* Tech. rep. DTIC Document, 1970.

[59] BJ Brinkworth. "Calculation of attenuation and back-scattering in cloud and fog". In: *Atmospheric Environment (1967)* 5.8 (1971), pp. 605–611.

[60] TEW Schumann. "Theoretical aspects of the size distribution of fog particles". In: *Quarterly Journal of the Royal Meteorological Society* 66.285 (1940), pp. 195–208.

[61] Barry H Friemel et al. "Speckle decorrelation due to two-dimensional flow gradients". In: *IEEE transactions on ultrasonics, ferroelectrics, and frequency control* 45.2 (1998), pp. 317–327.

[62] J David Briers, Glenn Richards, and Xiao Wei He. "Capillary blood flow monitoring using laser speckle contrast analysis (LASCA)". In: *Journal of biomedical optics* 4.1 (1999), pp. 164–175.

[63] Sabine Przibilla et al. “Sensing dynamic cytoplasm refractive index changes of adherent cells with quantitative phase microscopy using incorporated microspheres as optical probes”. In: *Journal of biomedical optics* 17.9 (2012), pp. 0970011–0970019.

[64] DJ Pine et al. “Diffusing wave spectroscopy”. In: *Physical review letters* 60.12 (1988), p. 1134.

[65] Virgile Viasnoff, Francois Lequeux, and DJ Pine. “Multispeckle diffusing-wave spectroscopy: A tool to study slow relaxation and time-dependent dynamics”. In: *Review of scientific instruments* 73.6 (2002), pp. 2336–2344.

[66] Mooseok Jang et al. “Relation between speckle decorrelation and optical phase conjugation (OPC)-based turbidity suppression through dynamic scattering media: a study on in vivo mouse skin”. In: *Biomedical optics express* 6.1 (2015), pp. 72–85.

[67] Ying Min Wang et al. “Deep-tissue focal fluorescence imaging with digitally time-reversed ultrasound-encoded light”. In: *Nature communications* 3 (2012), p. 928.

[68] Yan Liu et al. “Optical focusing deep inside dynamic scattering media with near-infrared time-reversed ultrasonically encoded (TRUE) light”. In: *Nature Communications* 6 (2015).

[69] Daifa Wang et al. “Focusing through dynamic tissue with millisecond digital optical phase conjugation”. In: *Optica* 2.8 (2015), pp. 728–735.

[70] Joshua Brake, Mooseok Jang, and Changhuei Yang. “Analyzing the relationship between decorrelation time and tissue thickness in acute rat brain slices using multispeckle diffusing wave spectroscopy”. In: *JOSA A* 33.2 (2016), pp. 270–275.

[71] Yan Liu et al. “Focusing light inside dynamic scattering media with millisecond digital optical phase conjugation”. In: *Optica* 4.2 (2017), pp. 280–288.

[72] IM Vellekoop et al. “Demixing light paths inside disordered metamaterials”. In: *Optics express* 16.1 (2008), pp. 67–80.

[73] Ivo M Vellekoop and Christof M Aegerter. “Scattered light fluorescence microscopy: imaging through turbid layers”. In: *Optics letters* 35.8 (2010), pp. 1245–1247.

[74] Elbert G van Putten, A Lagendijk, and AP Mosk. “Optimal concentration of light in turbid materials”. In: *JOSA B* 28.5 (2011), pp. 1200–1203.

[75] Fanting Kong et al. “Photoacoustic-guided convergence of light through optically diffusive media”. In: *Optics letters* 36.11 (2011), pp. 2053–2055.

[76] Antonio M Caravaca-Aguirre et al. “High contrast three-dimensional photoacoustic imaging through scattering media by localized optical fluence enhancement”. In: *Optics express* 21.22 (2013), pp. 26671–26676.

[77] Jian Wei Tay et al. “Ultrasonically encoded wavefront shaping for focusing into random media”. In: *Scientific reports* 4 (2014), p. 3918.

[78] Jochen Aulbach et al. “Spatiotemporal focusing in opaque scattering media by wave front shaping with nonlinear feedback”. In: *Optics express* 20.28 (2012), pp. 29237–29251.

[79] Ori Katz et al. “Noninvasive nonlinear focusing and imaging through strongly scattering turbid layers”. In: *Optica* 1.3 (2014), pp. 170–174.

[80] Jianyong Tang, Ronald N Germain, and Meng Cui. “Superpenetration optical microscopy by iterative multiphoton adaptive compensation technique”. In: *Proceedings of the National Academy of Sciences* 109.22 (2012), pp. 8434–8439.

[81] SM Popoff et al. “Image transmission through an opaque material”. In: *arXiv preprint arXiv:1005.0532* (2010).

[82] Wonjun Choi et al. “Transmission eigenchannels in a disordered medium”. In: *Physical Review B* 83.13 (2011), p. 134207.

[83] Hyeonseung Yu et al. “Measuring large optical transmission matrices of disordered media”. In: *Physical review letters* 111.15 (2013), p. 153902.

[84] Thomas Chaigne et al. “Controlling light in scattering media non-invasively using the photoacoustic transmission matrix”. In: *Nature Photonics* 8.1 (2014), pp. 58–64.

[85] Angélique Drémeau et al. “Reference-less measurement of the transmission matrix of a highly scattering material using a DMD and phase retrieval techniques”. In: *Optics express* 23.9 (2015), pp. 11898–11911.

[86] Chia-Lung Hsieh et al. “Digital phase conjugation of second harmonic radiation emitted by nanoparticles in turbid media”. In: *Optics express* 18.12 (2010), pp. 12283–12290.

[87] Xiao Xu, Honglin Liu, and Lihong V Wang. “Time-reversed ultrasonically encoded optical focusing into scattering media”. In: *Nature photonics* 5.3 (2011), pp. 154–157.

[88] Ivo M Vellekoop, Meng Cui, and Changhuei Yang. “Digital optical phase conjugation of fluorescence in turbid tissue”. In: *Applied physics letters* 101.8 (2012), p. 081108.

[89] Ke Si, Reto Fiolka, and Meng Cui. “Fluorescence imaging beyond the ballistic regime by ultrasound-pulse-guided digital phase conjugation”. In: *Nature photonics* 6.10 (2012), pp. 657–661.

[90] Ke Si, Reto Fiolka, and Meng Cui. “Breaking the spatial resolution barrier via iterative sound-light interaction in deep tissue microscopy”. In: *arXiv preprint arXiv:1208.5264* (2012).

[91] Benjamin Judkewitz et al. “Speckle-scale focusing in the diffusive regime with time reversal of variance-encoded light (TROVE)”. In: *Nature photonics* 7.4 (2013), pp. 300–305.

[92] Cheng Ma et al. “Time-reversed adapted-perturbation (TRAP) optical focusing onto dynamic objects inside scattering media”. In: *Nature photonics* 8.12 (2014), pp. 931–936.

[93] Edward Haojiang Zhou et al. “Focusing on moving targets through scattering samples”. In: *Optica* 1.4 (2014), pp. 227–232.

[94] Haowen Ruan et al. “Iterative time-reversed ultrasonically encoded light focusing in backscattering mode”. In: *Scientific reports* 4 (2014), p. 7156.

[95] Yuta Suzuki et al. “Continuous scanning of a time-reversed ultrasonically encoded optical focus by reflection-mode digital phase conjugation”. In: *Optics letters* 39.12 (2014), pp. 3441–3444.

[96] Amnon Yariv. “Phase conjugate optics and real-time holography”. In: *IEEE Journal of Quantum Electronics* 14.9 (1978), pp. 650–660.

[97] Peter Günter. “Holography, coherent light amplification and optical phase conjugation with photorefractive materials”. In: *Physics Reports* 93.4 (1982), pp. 199–299.

[98] Roarke Horstmeyer, Haowen Ruan, and Changhuei Yang. “Guidestar-assisted wavefront-shaping methods for focusing light into biological tissue”. In: *Nature photonics* 9.9 (2015), pp. 563–571.

[99] Chia-Lung Hsieh et al. “Imaging through turbid layers by scanning the phase conjugated second harmonic radiation from a nanoparticle”. In: *Optics express* 18.20 (2010), pp. 20723–20731.

[100] Huichang Zhuang et al. “High speed color imaging through scattering media with a large field of view”. In: *Scientific Reports* 6 (2016).

[101] Jacopo Bertolotti et al. “Non-invasive imaging through opaque scattering layers”. In: *Nature* 491.7423 (2012), pp. 232–234.

[102] Amir Porat et al. “Widefield lensless imaging through a fiber bundle via speckle correlations”. In: *Optics Express* 24.15 (2016), pp. 16835–16855.

[103] *Range-Gating Technology*. `http://www.obzerv.com/en/range-gating-technology/core-expertise/`. Accessed: 2017-04-10.

[104] Martin Laurenzis and Arnaud Woiselle. “Laser gated-viewing advanced range imaging methods using compressed sensing and coding of range-gates”. In: *Optical Engineering* 53.5 (2014), pp. 053106–053106.

[105] David Monnin et al. “Active-imaging-based underwater navigation”. In: *SPIE Security+ Defence*. International Society for Optics and Photonics. 2015, 96490H–96490H.

[106] Frank Christnacher et al. “Influence of gating and of the gate shape on the penetration capacity of range-gated active imaging in scattering environments”. In: *Optics express* 23.26 (2015), pp. 32897–32908.

[107] M Teschke et al. “High-speed photographs of a dielectric barrier atmospheric pressure plasma jet”. In: *IEEE Transactions on Plasma Science* 33.2 (2005), pp. 310–311.

[108] Achuta Kadambi et al. “Frequency domain ToF: encoding object depth in modulation frequency”. In: *arXiv preprint arXiv:1503.01804* (2015).

[109] Claus Weitkamp. *Lidar: range-resolved optical remote sensing of the atmosphere*. Vol. 102. Springer Science & Business, 2006.

[110] David Huang et al. “Optical coherence tomography”. In: *Science (New York, NY)* 254.5035 (1991), p. 1178.

Chapter 2

FOCUSING ON MOVING TARGETS THROUGH SCATTERING SAMPLES

This chapter is adapted from the manuscript Zhou, E.H., Ruan, H., Yang, C. & Judkewitz, B. "Focusing on moving targets through scattering samples". Optica 1, 227 (2014). The contributions of authors are as follows: BJ and CY conceived the initial idea. EHZ and BJ developed the idea and scheme demonstration. The experiments were designed and performed by EHZ and BJ. The data analyses were performed by EHZ, HR, CY, and BJ.

Focusing light through scattering media is of great importance for imaging and stimulation in biomedical optics. While wavefront shaping and optical time-reversal techniques can in principle be used to focus light across scattering media, achieving this within a scattering medium with a noninvasive and efficient reference beacon, or guide star, remains an important challenge. In this chapter, we show optical time-reversal focusing using a new technique termed Time Reversal by Analysis of Changing wavefronts from Kinetic targets (TRACK). By taking the difference between time-varying scattering fields caused by a moving object and applying optical time reversal, light can be focused back to the location previously occupied by the object. We demonstrate this approach with discretely moved objects as well as with particles in an aqueous flow, and obtain a focal peak-to-background strength of 204 in our demonstration experiments. We further demonstrate that the generated focus can be used to noninvasively count particles in a flow-cytometry configuration—even when the particles are hidden behind a strong diffuser. By achieving optical time reversal and focusing noninvasively without any external guide stars, using just the intrinsic characteristics of the sample, this work paves the way to a range of scattering media imaging applications, including underwater and atmospheric focusing as well as noninvasive *in vivo* flow cytometry.

2.1 Introduction

Focusing light through highly scattering media is an important challenge in biomedical imaging, colloidal optics, and astronomy. When light propagates through strongly scattering samples, refractive index inhomogeneities scatter the light field in many directions. This was long thought of as a randomizing process, which

precludes the formation of a sharp focus. However, by taking advantage of the deterministic nature of scattering, researchers in the field of complex wavefront shaping have demonstrated that light can be focused at an arbitrary location within and across scattering media—by shaping the input wavefront reaching the sample [1, 2]. Because appropriate input wavefronts are complex and because they depend on sample structure as well as target location, determining them remains a key challenge. With direct optical access to the input plane and the focusing plane, wavefronts can be found with one of three strategies: iterative optimization [1, 3–5], optical time reversal[6], or measuring and inverting the sample transmission matrix [7, 8]. When there is no direct access to the target plane, e.g., when the target plane is hidden within the sample, physical guide stars such as beads can be placed within the sample and used as reference beacons [9–11]. Because this requires invasive insertion, recent research has focused on virtual, ultrasound-based guide stars relying on the acousto-optic [12–16] or the photo-acoustic effect[17–20]. However, all of these strategies are either limited by the acoustic resolution (tens of micrometers at best) or require many measurements, thereby increasing the recording time by orders of magnitude. Thus far, near-instantaneous time reversal at optical resolutions remains elusive. Here we introduce a new all-optical method, termed Time Reversal by Analysis of Changing wavefronts from Kinetic targets (TRACK), which achieves precise optical time reversal to a target hidden behind a scattering sample—without the need for acoustic guide stars. Unlike previous techniques, this method uses the motion of the target itself to serve as a guide star.

2.2 Principles

A concise setup for noninvasively focusing light through a scattering sample is shown in Fig. 2.1. The complete setup can be found in the latter section. We interpret optical scattering through our diffuser as a linear process described by a complex spatial transmission matrix, $T(x_a, x_b)$ [1]. This matrix defines the transformation of the optical field at an input plane with coordinates x_a directly before the diffuser to an output plane with coordinates x_b behind the diffuser, where we have a moving target with a reflectivity function $R(x_b)$. We assume that our digital phase-conjugation system is set up such that we can discretely measure and control the optical field along the input plane coordinates x_a.

Our detect-and-refocus process is composed of four primary steps. First, we illuminate the scatterer with an input wave, $U(x_a)$, to reflect light off our target. $U(x_a)$ transforms into a speckle field at the output plane as defined by the transmission

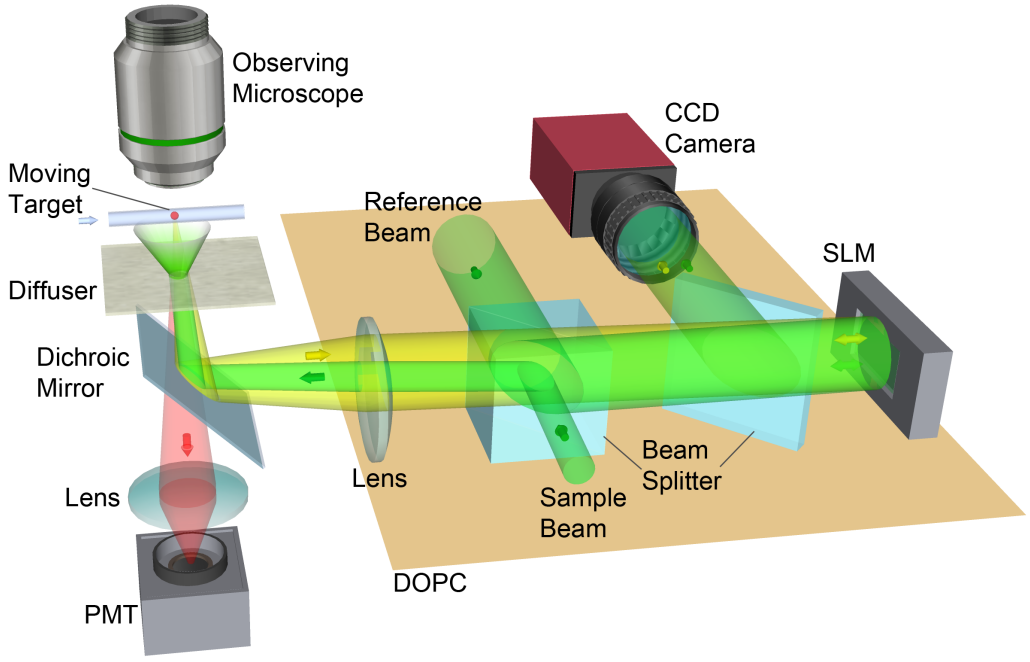

Figure 2.1: **Concise setup including sample for TRACK**: varying backscattered wavefronts due to a target's movement are captured by off-axis holography. The phase of the wavefront difference is time reversed by the digital optical phase-conjugation (DOPC) system. Diffuse light is focused back to the previous position of the target.

matrix: $S(x_b) = T(x_a, x_b)U(x_a)$. A portion of the speckle field $S(x_b)$ will hit our target object with reflectivity function $R(x_b)$. The target object's back-reflected optical field is thus the product $E_1(x_b) = R(x_b)S(x_b)$. Note that $R(x_b) = 0$ and hence $E_1(x_b) = 0$ everywhere except along the target's finite spatial extent. We also assume $S(x_b) \neq 0$ somewhere along our target to ensure a nonzero reflected signal.

Second, we measure the entire backscattered optical field at the input plane, $M_1(x_a)$, as depicted in Fig. 2.2(a). Following linear optics, we split the backscattered field $M_1(x_a)$ into a sum of two components: one reflected from out target object at the output plane, $E_1'(x_a)$, and one originating from all other locations within the sample volume, $B(x_a)$. The target-dependent component $E_1'(x_a)$ is defined as the target-reflected optical field at the output plane, $E_1'(x_b)$. After it has backscattered to the input plane. Following the common assumption of a lossless scattering process, we may use our transmission matrix to express $E_1'(x_a)$ as

$$E_1'(x_a) = T^t(x_a, x_b)E_1(x_b), \tag{2.2.1}$$

where T^t, the transpose of T, represents the reverse process of scattering from the output to the input plane. The total measured field at the input plane is thus the sum

$$M_1(x_a) = T^t(x_a, x_b)E_1(x_b) + B(x_a), \tag{2.2.2}$$

where again $B(x_a)$ is the background optical field arising from all other locations within the sample.

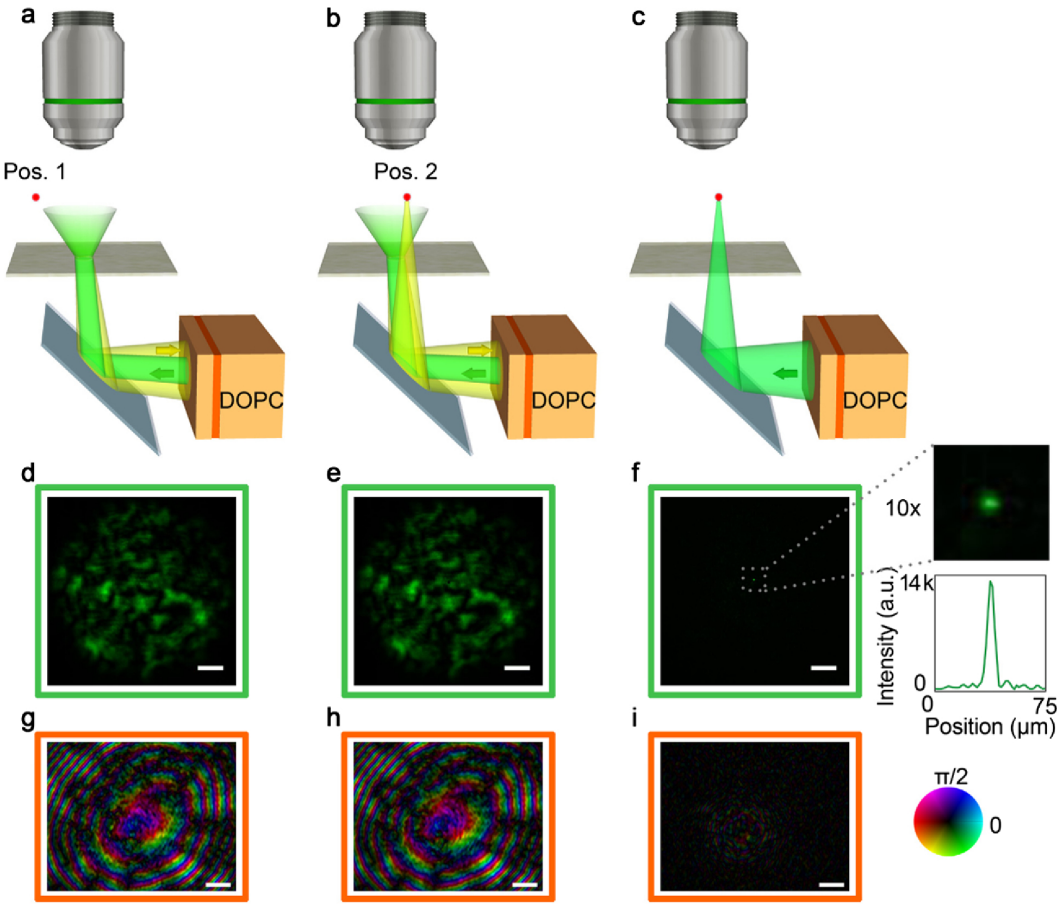

Figure 2.2: **Focusing on a moving target through a scattering sample**: (a) target at position 1 (far off the illuminated field of view); (b) target at position 2 (within the illuminated field of view); (c) light is focused behind the diffuser; (d)–(f) corresponding images recorded with the observing microscope; (g) and (h) phase maps recorded at the camera imaging the SLM surface; (i) difference of field in (g) and field in (h). The cross-section intensity distribution in (f) indicates a PBR of 204. Scale bars in (d)–(f) are 100 μm. Scale bars in (g)–(i) all stand for 1 mm.

Third, we measure a second backscattered field at the input plane, $M_2(x_a)$, after the reflective target object physically shifts a finite distance Δ across the output plane. This measurement is depicted in Fig. 2.2(b). A spatially shifted target will generate

a new reflected field, $E_2(x_b) = R(x_b - \Delta)S(x_b)$, which will again transform to the input plane via our transmission matrix and combine with a background field contribution to yield

$$M_2(x_a) = T^t(x_a, x_b)E_2(x_b) + B(x_a). \tag{2.2.3}$$

Equation 2.2.3 implicitly assumes that T and $B(x_a)$ remain the same as for the first measurement, requiring the scattering sample to be stationary (apart from target motion) at the time scale of the measurement interval.

Fourth, we digitally subtract our two measurements to efficiently remove and background contribution and isolate the target-reflected signal:

$$M_2(x_a) - M_1(x_a) = T^t(x_a, x_b)[E_2(x_b) - E_1(x_b)]. \tag{2.2.4}$$

We compute the phase conjugate of this subtraction and display it on our digital optical phase-conjugation (DOPC) setup's spatial light modulator (SLM) to create the following field at the input plane: $T^\dagger[E_2(x_b) - E_1(x_b)]^*$, where $\dagger$ denotes a conjugate transpose and $*$ a complex conjugation. This field scatters from the sample's input to output plane to form our final target-focused field, $E_f(x_b)$, as shown in Fig. 2.2(c):

$$E_f(x_b) = T(x_a, x_b)T^\dagger(x_a, x_b)[E_2(x_b) - E_1(x_b)]^* \approx [E_2(x_b) - E_1(x_b)]^*. \tag{2.2.5}$$

Here, we assume a complete scattering process to form the approximation $T(x_a, x_b)T^\dagger(x_a, x_b) \approx I$, the identity matrix. Conjugate light thus forms the field $E_2 - E_1$ at the sample plane, implying light is focused to both shifted target positions. If the target was originally off the laser speckle field (i.e., E_1 is zero everywhere), a focus will appear only at its second location, which corresponds to our ability to refocus onto a moving object.

2.3 Methods

Setup

All data were collected by a self-built optical system schematically described in Fig. 2.3. In the setup, we used a 532 nm fiber-coupled semiconductor laser (Spectra Physics, Excelsior 532). The polarization of the beam was made horizontal (by a half-wave plate and polarizing beam splitter), which is in accordance with SLM (Holoeye, PLUTO) modulation polarization. Beam splitter 1 splits the incoming light into two beams: the sample beam and the reference beam. The sample beam

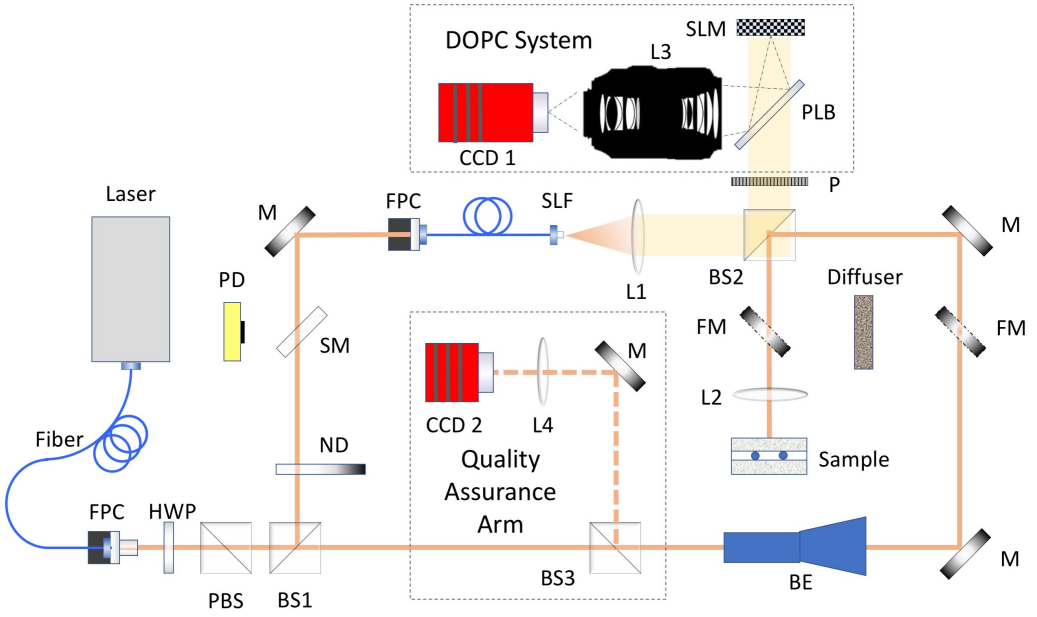

Figure 2.3: **Full setup diagram for TRACK**: Abbreviation: ND-Neutral Density filter wheel, BE-Beam Expander, BS1,2,3-Beam Splitter 1,2,3, BSH-Beam shutter, D-Diffuser, FM-Flip Mirror, FPC-Fiber Port Collimator, HWP-Half wave Plate,L1,2,3-Lens 1,2,3, M-Mirror, P-Polarization Plate, PBS-Polarizing Beam Splitter, PD-Photo Detector, PLB-Plate beam splitter, SM-Sample Mirror, SLF-Spatial Light Filter, SLM-Spatial Light Modulator.

was expanded by a laser expander for a suitable size of laser spot at the sample. Reflected by mirrors and beam splitter 2, the sample beam passed through lens 2 and was eventually reflected to the sample by a dichroic mirror, which was at a 45° angle to the horizontal plane (it is hard to show in the 2D scheme in Fig. 2.3; details of the sample setup can be found in Fig. 2.1). The sample was placed close to the focal plane of lens 2. Light backscattered by the sample was collected to the SLM by lens 2. The reference beam passed through a neutral density filter and was coupled into a single-mode polarization maintaining fiber for spatial filtering. After exiting the fiber, the beam was collimated by lens 1. Scattered light and reference light were combined by beam splitter 2 before reaching the DOPC system. Polystyrene beads were obtained from Life Technology. Retro-reflective beads, which consisted of aluminum coated 50 µm glass spheres, were obtained from Cospheric. To create samples we used adhesive backed, highly diffusing films (3M Scotch model no.810, 60 µm thick), which did not transmit a detectable ballistic component (measured with a detection threshold of 10^{-8} of the illumination power).

We used it as a random phase plate diffuser whose angle scattering distribution is plotted in appendix. To show that our results can be extended to biological samples, we performed TRACK experiments through a 0.5 mm thick section of *ex vivo* chicken muscle tissue (scattering coefficient μ_s: 30 mm^{-1} and anisotropy parameter g: 0.965 [14]). The results of this experiment are shown in appendix.

Fluorescence Signal Capture

In the flow-cytometry experiment, we used orange fluorescent (540/560) polystyrene microspheres obtained from Life Technology. As shown in Fig. 2.6(c), orange fluorescence from the beads propagated through the diffuser along with diffuse backscattered light at 532 nm. Colors were separated by the dichroic mirror (a 532 edge pass filter, model Di02-R532-25 $\times$ 36 from Semrock). Underneath the dichroic mirror, a lens images the surface of the diffuser to a compact PMT. The fluorescence spectrum of the sample and the transmission spectrum of edge pass filter are shown in Fig. 2.4. A median filter was used to filter the signal shown in Fig. 2.6(e).

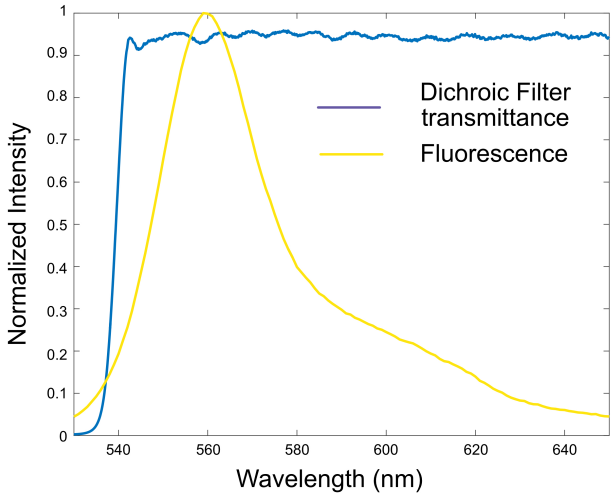

Figure 2.4: **Fluorescence spectrum of cytometry bead and dichroic mirror transmission spectrum.**

Reference Phase Correction

As aforementioned in discussion, in digital phase conjugation, reference beam and SLM curvature will affect the conjugate phase map and thus the time-reversal PBR. By digitally modulating the SLM curvature to iteratively maximize the reflection

from the SLM back into the single-mode fiber in the reference beam arm, we can compensate for SLM curvature as well as reference beam phase errors [14]. A threefold enhancement is observed.

Quality Assurance Setup

To assure the pixel-to-pixel alignment between the camera and SLM and the performance of the DOPC system, a quality assurance arm was configured in the sample arm including two flipping mirrors, beam splitter 3, a mirror, lens 4 and camera 2 (as shown in Fig. 2.3). When flip mirrors were flipped up, the system was changed from the reflective mode to the transmission mode. When applying time reversal, we expected to observe a focus on camera 2. By tuning the position and tilting of the SLM, we optimized the intensity of the focus. In this way, a day-to-day precise alignment of the DOPC system was guaranteed.

2.4 Results

Direct Observation of Optical Focusing in Reflection Mode

Our reflection-mode TRACK setup is diagramed in Fig. 2.1. To record backscattered light at the SLM plane, a camera was pixel-to-pixel aligned to image the SLM surface, and wavefronts were measured by off-axis holography [21, 22]. For demonstration, we created a sample consisting of 10 μm diameter polystyrene beads behind a highly diffusing tape. The beads were placed on a glass slide 7 mm behind the diffuser, whose movement was two-dimensionally controlled by a piezo stage. To confirm the formation of a focus through scattering media, an observing microscope (OM) was set up to image the target plane from the back. Importantly, this microscope was only used for validation of successful focusing, but not to derive wavefronts or create the foci.

We started by recording a backscattered wavefront without any targets behind the diffuser (Fig. 2.2(g)) and compared it to the wavefront measured when a target was inside the illuminated field of view (Fig. 2.2(h)). As expected, both wavefronts were dominated by backscattering from the entire diffuser, while the relative difference of the wavefronts was 15% (relative average amplitude) [Fig. 2.2(i)]. When we time reversed the difference wavefront by digital phase conjugation, the OM recorded a high-contrast focus at the location of the target. Fig. 2.2(f) includes a plot of the intensity profile (horizontal section across the peak), which shows a peak-to-background ratio (PBR) of 204.

Moving Target Tracking behind Scattering Media

If we keep repeating this experiment with a continuously moving target, light will be focused dynamically on the target. In other words, we can track the moving target through the scattering medium. To confirm this experimentally, we recorded a background wavefront at the SLM plane (with no target bead in the illuminated area), and subsequently moved a target bead to multiple locations within the illuminated area. At each position of the target [as shown in Figs. 2.5(a)–(c)], after recording the wavefront, we subtracted the background wavefront from the current wavefront and time reversed the result such that it focused on the current location of the target [as shown in Figs. 2.5(d)–(f)]. A detailed timing diagram of the system is included in the appendix. In this experiment, a 50 µm diameter retro-reflective target bead was 14 mm behind the diffuser.

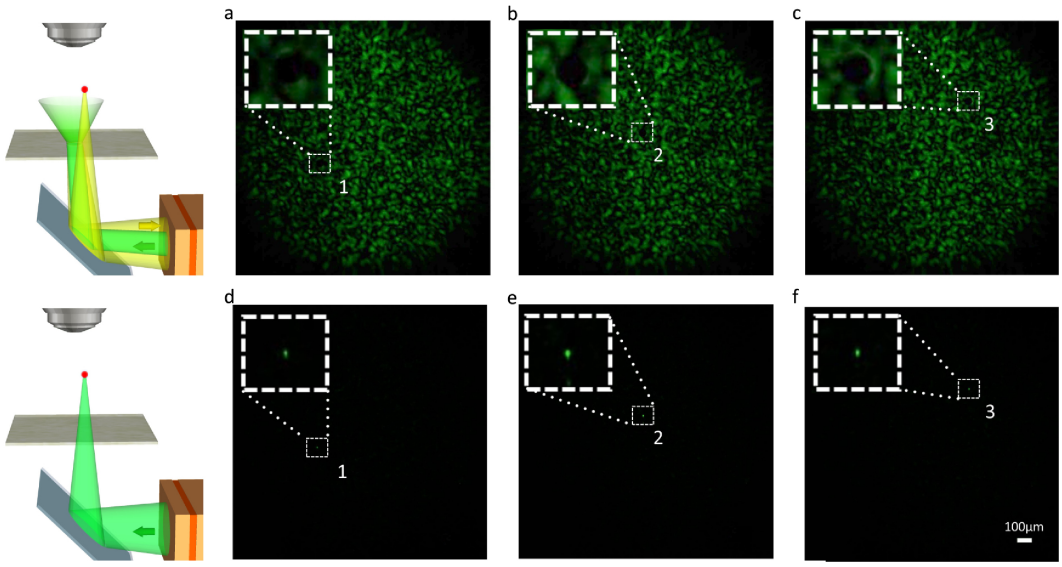

Figure 2.5: **Target tracking by TRACK**: images taken with the observing microscope. (a)–(c) Images of targets at positions 1–3 in the laser speckle; (d)–(f) phase conjugate foci at corresponding positions.

Optical Flow Cytometry in Scattering Media

To mimic an in vivo flow-cytometry scenario, we placed a microfluidic channel behind the diffuser. Two kinds of beads were used in this experiment: nonfluorescent polystyrene beads as guide stars and fluorescent beads to be counted in a flowcytometry-type setup. Repeating the first experiment ("direct observation of optical focusing," above) in a microfluidic channel, we recorded two scattering fields with a guide star bead outside and inside the illuminated area (Fig. 2.6(a)

and Media 1). We then phase conjugated the difference wavefront and observed a focus at the exact position of the guide bead (as shown in Fig. 2.6(c) and Media 1). From the cross-section intensity distribution, we measured a PBR of 134 and a full width half-maximum (FWHM) of 8.9 µm. After formation of the focus, fluorescence beads were flown at a speed of 5 cm/s, and the time-varying fluorescence signal was recorded by a single-channel photomultiplier tube (PMT). The PMT trace contained clearly detectable signals that corresponded to fluorescent beads passing the focus. Illumination, phase conjugation, and fluorescence detection by the PMT all occurred on the same side of the scattering sample in a reflection geometry.

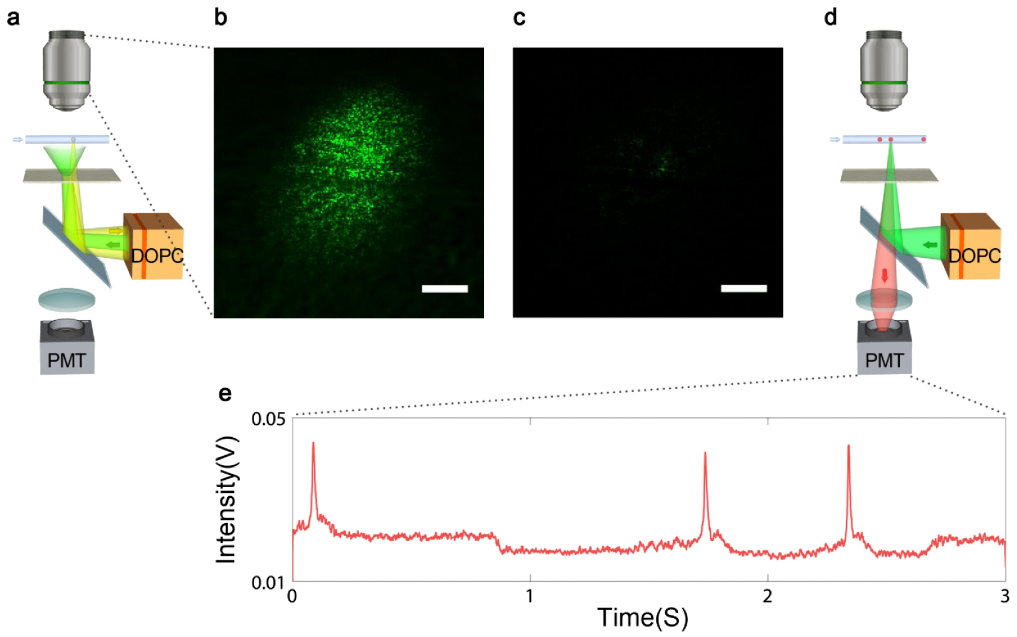

Figure 2.6: **Optical flow cytometry in scattering media**: (a) schematic of the recording step, in which a focus is established as above; (b) laser speckle shining on the microfluidic channel as imaged by the observing camera; (c) time-reversed focus established with the help of the first bead; (d) schematic of the particle counting setup; (e) signal captured on the PMT with clear signals caused by fluorescent beads passing the focus. Both scale bars stand for 100 µm.

2.5 Discussion

In this work we provided, to the best of our knowledge, the first demonstration of time-reversed optical focusing through scattering media by using the motion of a target object as a guide star—a technique we call TRACK. We would like to use this section to note some points of consideration associated with this work.

First, TRACK will focus on all backscattering targets that moved between the two

wavefront recordings. If the goal is to focus on a single target or bead, only one moving backscattering bead should be within the illuminated area.

Second, we would like to point out that our experimental setup associated with the experimental findings shown in Fig. 2.2,2.5 and 2.6 contain a microscope objective and camera (outlined in green in 2.1) that allowed us to directly observe the space after the diffuser. We used that imaging system to directly observe and verify that the TRACK focus was achieved. In practical applications, it is unlikely that such an observation perspective would be available. In most of the application scenarios, our only access to the target of interest would be on one side of the diffusing medium, in a reflection geometry. A good case in point would be the task of reflection-mode focusing of light through skin and into a blood vessel. The reflection-mode focusing results presented here show that focusing light in this geometry is feasible. For example, upon creating the time-reversed optical focus (Fig. 2.6), we can observe the passage of fluorescent beads through the microfluidic channel by simply observing the upticks in fluorescence scattered back through the diffuser. Another important trade-off space this method introduces is an intrinsic relationship between focus spot size and achievable PBR. Mathematically, these two quantities are related to each other through the number of optical modes that the DOPC can capture and control during playback [23]:

$$PBR_{phase-only} \approx \frac{\pi}{4} \cdot \frac{N_{SLM}}{N_{target}}, \tag{2.5.1}$$

where N_{SLM} indicates modes on the SLM from the scattering of the target and N_{target} represents the number of modes modulated by the target in the speckle plane. The above formula contains a $\pi/4$ factor because the DOPC in this set of experiments is a phase-only modulator system. For the experimental setup used for Fig. 2.2, the above formula predicts a focus PBR of 390—a quantity that is consistent with our experimental result of 204, indicating a time-reversal efficiency of >50%. The above formula leads to an interesting consequence. By using smaller target objects, we can effectively create a tighter optical focus and simultaneously boost the PBR. However, we caution that the use of ever smaller target objects will lead to a weaker initial scattering signal arriving at the DOPC and in turn degrade the time-reversed wavefront in the presence of noise. This will then reduce the focus PBR.

As the different sets of experimental results reported in Figs. 2.5 and 2.6 show, this method can be used to create a time-reversed focus that tracks with the target object or to create a fixed and static focus at a specific location along the trajectory of the object. Each of these focusing types is useful for different applications: dynamic

tracking can potentially be useful for following moving targets in deep ocean or convective atmosphere environments, while the static focus would be most useful for flow-cytometry-type applications.

Appendix

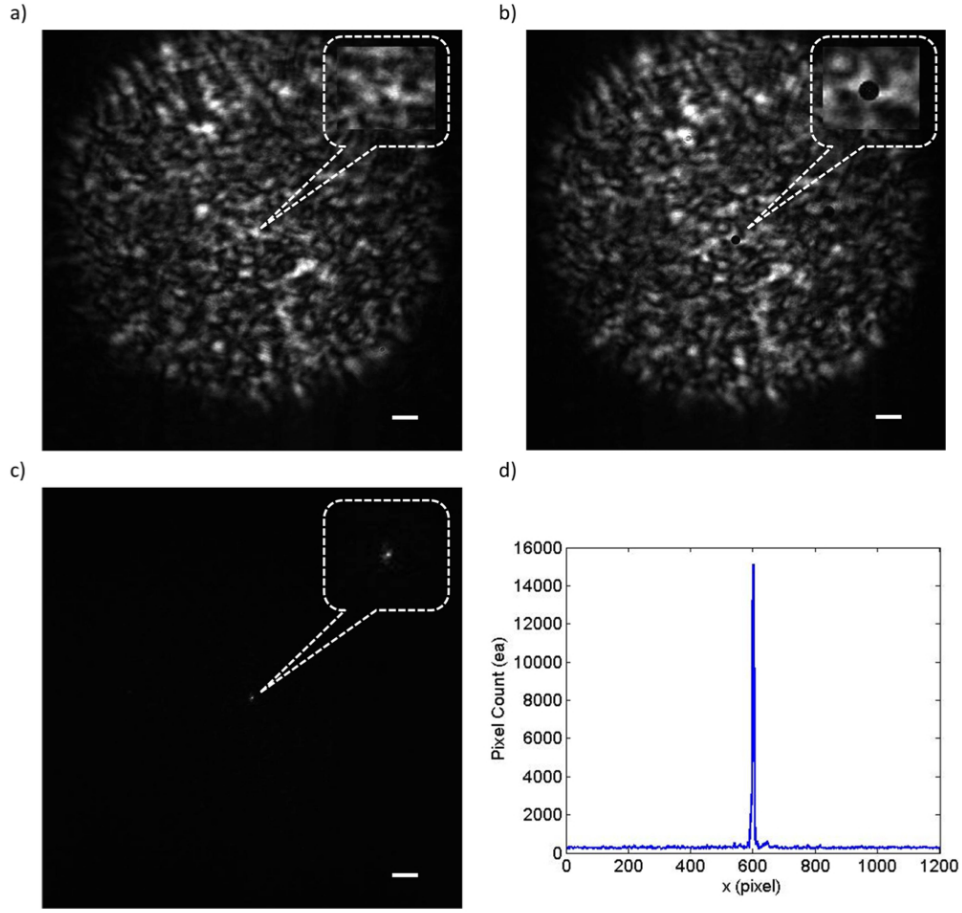

Figure 2.7: TRACK focusing with an experimental setup analogous to the one in Fig. 2.2, except that the diffuser was replaced with 0.5 mm thick chicken breast tissue (μ_s: 30 mm^{-1}). a) Laser speckle captured when the target is outside the speckle formed behind a 0.5 mm thick section of chicken breast. b) Laser speckle when the target moves in. c) Phase-conjugate focus. d) Cross section of the focus. Scale bars: 100 µm.

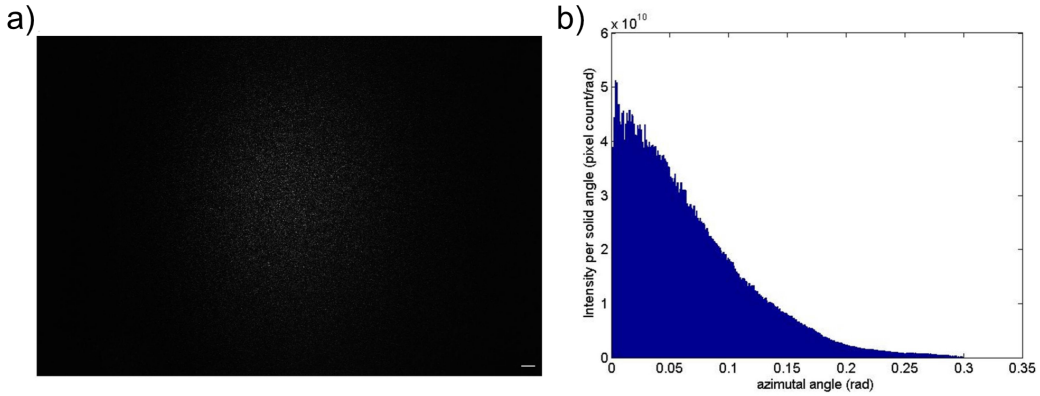

Figure 2.8: **Angle distribution of the diffusing sample**: a) Speckle pattern captured 7.25cm behind the diffuser attached to a pinhole shined laser through. b) Distribution of intensity scattering angle. Scale bar: 1 mm.

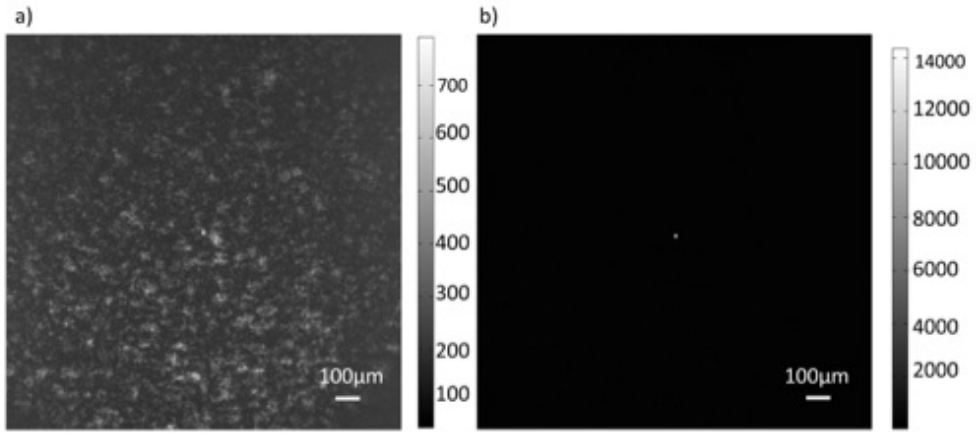

Figure 2.9: To compare TRACK to traditional reflective bead guide-stars, we performed an experiment analogous to the one described in Fig. 2.2, but started by time-reversing just one wavefront M_1 (recorded when a reflective bead was present behind the scattering medium – see Eq. 2.2.2. a) Image recorded by the observing camera when such a wavefront was time-reversed. The focus is barely visible on top of the background. b) TRACK focusing with the difference wavefront $M_1 - M_2$, where M_2 was the wavefront recorded after the target was moved outside the field of view.

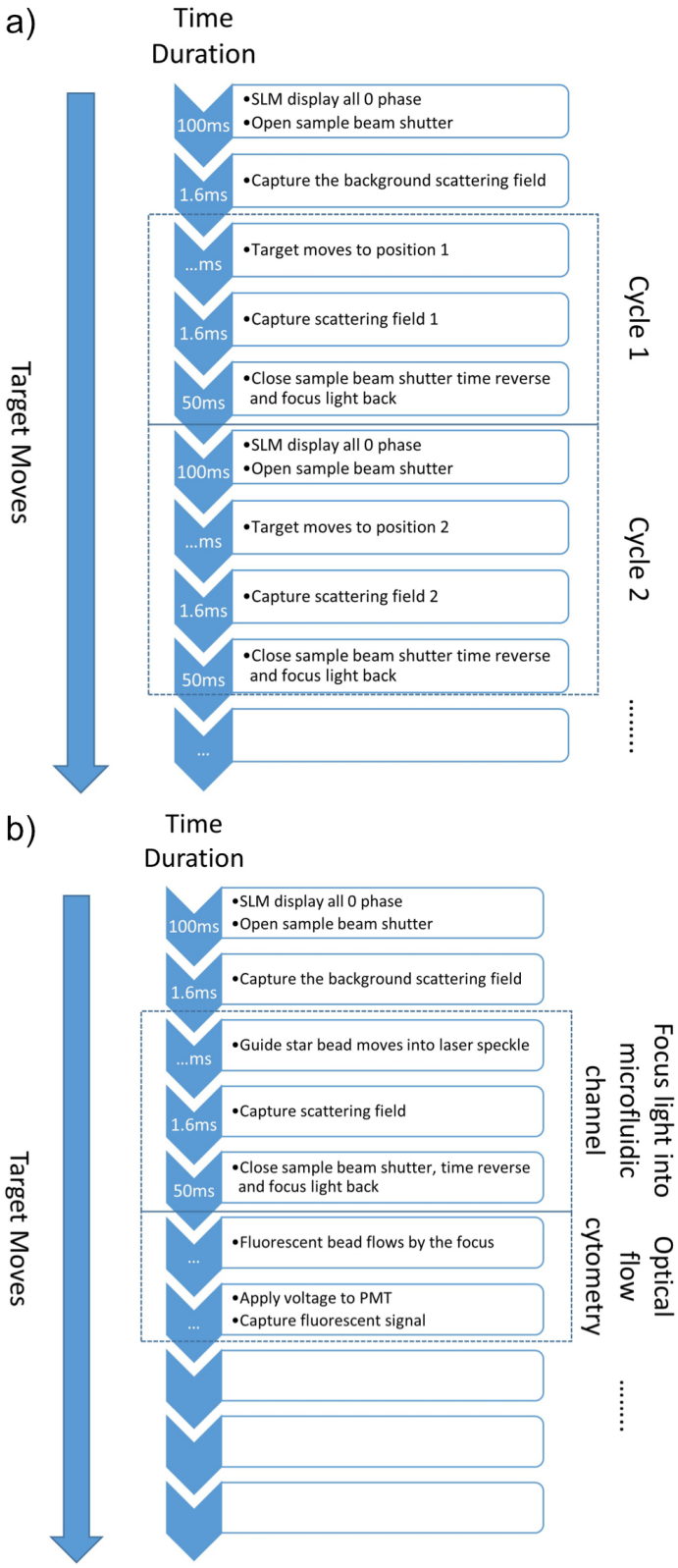

Figure 2.10: **Timing for the experiments**: a) Experiment in Fig. 2.5. b) Experiment in Fig.2.6.

References

[1] Ivo M Vellekoop and AP Mosk. “Focusing coherent light through opaque strongly scattering media”. In: *Optics letters* 32.16 (2007), pp. 2309–2311.

[2] Allard P Mosk et al. “Controlling waves in space and time for imaging and focusing in complex media”. In: *Nature photonics* 6.5 (2012), pp. 283–292.

[3] IM Vellekoop, Ad Lagendijk, and AP Mosk. “Exploiting disorder for perfect focusing”. In: *arXiv preprint arXiv:0910.0873* (2009).

[4] Donald B Conkey, Antonio M Caravaca-Aguirre, and Rafael Piestun. “High-speed focusing of light through dynamic turbid media”. In: *Computational Optical Sensing and Imaging*. Optical Society of America. 2012, CTu4B–6.

[5] Zahid Yaqoob et al. “Optical phase conjugation for turbidity suppression in biological samples”. In: *Nature photonics* 2.2 (2008), pp. 110–115.

[6] Hasan Yılmaz, Willem L Vos, and Allard P Mosk. “Optimal control of light propagation through multiple-scattering media in the presence of noise”. In: *Biomedical optics express* 4.9 (2013), pp. 1759–1768.

[7] SM Popoff et al. “Image transmission through an opaque material”. In: *arXiv preprint arXiv:1005.0532* (2010).

[8] Youngwoon Choi et al. “Scanner-free and wide-field endoscopic imaging by using a single multimode optical fiber”. In: *Physical review letters* 109.20 (2012), p. 203901.

[9] Chia-Lung Hsieh et al. “Digital phase conjugation of second harmonic radiation emitted by nanoparticles in turbid media”. In: *Optics express* 18.12 (2010), pp. 12283–12290.

[10] Ivo M Vellekoop, Meng Cui, and Changhuei Yang. “Digital optical phase conjugation of fluorescence in turbid tissue”. In: *Applied physics letters* 101.8 (2012), p. 081108.

[11] Xiaodong Tao et al. “Live imaging using adaptive optics with fluorescent protein guide-stars”. In: *Optics express* 20.14 (2012), pp. 15969–15982.

[12] Xiao Xu, Honglin Liu, and Lihong V Wang. “Time-reversed ultrasonically encoded optical focusing into scattering media”. In: *Nature photonics* 5.3 (2011), pp. 154–157.

[13] Puxiang Lai et al. “Reflection-mode time-reversed ultrasonically encoded optical focusing into turbid media”. In: *Journal of Biomedical Optics* 16.8 (2011), pp. 080505–080505.

[14] Ying Min Wang et al. “Deep-tissue focal fluorescence imaging with digitally time-reversed ultrasound-encoded light”. In: *Nature communications* 3 (2012), p. 928.

[15] Ke Si, Reto Fiolka, and Meng Cui. “Fluorescence imaging beyond the ballistic regime by ultrasound-pulse-guided digital phase conjugation”. In: *Nature photonics* 6.10 (2012), pp. 657–661.

[16] Benjamin Judkewitz et al. “Speckle-scale focusing in the diffusive regime with time reversal of variance-encoded light (TROVE)”. In: *Nature photonics* 7.4 (2013), pp. 300–305.

[17] Fanting Kong et al. “Photoacoustic-guided convergence of light through optically diffusive media”. In: *Optics letters* 36.11 (2011), pp. 2053–2055.

[18] Donald B Conkey et al. “Super-resolution photoacoustic imaging through a scattering wall”. In: *Nature communications* 6 (2015).

[19] Puxiang Lai et al. “Nonlinear photoacoustic wavefront shaping (PAWS) for single speckle-grain optical focusing in scattering media”. In: *arXiv preprint arXiv:1402.0816* (2014).

[20] Thomas Chaigne et al. “Controlling light in scattering media non-invasively using the photoacoustic transmission matrix”. In: *Nature Photonics* 8.1 (2014), pp. 58–64.

[21] Ulf Schnars and Werner Jüptner. “Direct recording of holograms by a CCD target and numerical reconstruction”. In: *Applied optics* 33.2 (1994), pp. 179–181.

[22] Etienne Cuche, Pierre Marquet, and Christian Depeursinge. “Spatial filtering for zero-order and twin-image elimination in digital off-axis holography”. In: *Applied optics* 39.23 (2000), pp. 4070–4075.

[23] Ivo Micha Vellekoop. “Controlling the propagation of light in disordered scattering media”. In: *arXiv preprint arXiv:0807.1087* (2008).

Chapter 3

FOCUSING THROUGH DYNAMIC TISSUE WITH MILLISECOND DIGITAL OPTICAL PHASE CONJUGATION

This chapter is adapted from the manuscript Wang, D., Zhou, E.H.*, Brake, J., Ruan, H., Jang, M. & Yang, C. "Focusing through dynamic tissue with millisecond digital optical phase conjugation". Optica 2, 728 (2015). The contributions of authors are as follows: HR, MJ and CY conceived the initial idea. EHZ and DW developed the idea and experimental scheme. The experiments were designed and performed by EHZ and DW. The data analyses were performed by DW, EHZ, HR, and CY. * denotes equal contribution to the work.*

Digital optical phase conjugation (DOPC) is a new technique employed in wavefront shaping and phase conjugation for focusing light through or within scattering media such as biological tissues. DOPC is particularly attractive as it intrinsically achieves a high fluence reflectivity in comparison to non-linear optical approaches. However, the slow refresh rate of liquid crystal spatial light modulators and limitations imposed by computer data transfer speeds have thus far made it difficult for DOPC to achieve a playback latency shorter than ~ 200 ms and therefore prevented DOPC from being practically applied to thick living samples. In this paper, we report a novel DOPC system that is capable of 5.3 ms playback latency. This speed improvement of almost two orders of magnitude is achieved by using a DMD (digital micromirror device), field programmable gate array (FPGA) processing, and a single-shot binary phase retrieval technique. With this system, we are able to focus through 2.3 mm living mouse skin with blood flowing through it (decorrelation time ~ 30 ms) and demonstrate that the focus can be maintained indefinitely—an important technological milestone that has never been previously reported.

3.1 Introduction

Focusing light through tissues has long been a challenge for biomedical optics. The turbid nature of tissues strongly scatters light and hinders the formation of a sharp focus. Recently, research in the field of wavefront shaping has shown that by correcting the wavefront incident on scattering media, focus can be constructed at an arbitrary location behind the sample [1, 2]. Different strategies have been developed to realize this process, including iterative wavefront optimization [1, 3–

5], transmission matrix measurement [6–8], and optical phase conjugation (OPC) [9–11]. Among these, OPC implements the corrected wavefront by recording the scattered light field globally and then playing back the conjugate light field by a phase conjugate mirror (PCM) without time-consuming iterations. Since the process of elastic light scattering is time symmetric, by playing a conjugate version of the scattered wavefront back through the scattering medium, the conjugate input wavefront can be recovered.

By employing OPC, a number of novel techniques for focusing light through or within a scattering medium have recently been developed. These include TRUE (Time-Reversed Ultrasonically Encoded Light) [12, 13], TROVE (Time Reversal of Variance-Encoded light) [14], TRACK (Time Reversal by Analysis of Changing wavefronts from Kinetic targets) [15], and TRAP (Time-Reversed Adapted-Perturbation) focusing [16]. These methods have the potential to improve or enable biomedical applications such as deep tissue imaging, photodynamic therapy, and noninvasive cytometry.

There are two major advantages of OPC compared to other wavefront shaping techniques. First, it is able to arrive at the correct wavefront solution without iteration. Second, the number of controllable optical modes in the playback wavefront can be very high; $\sim 5 \times 10^5$ modes or more. Optical phase conjugation methods can be categorized into two primary groups. Non-linear OPC methods [12, 17, 18] employ non-linear crystals to store the scattered field and propagate the phase conjugate field. In contrast, the digital optical phase conjugation (DOPC) method [13–16] uses an electronic camera in an interferometric setup to capture the optical wavefront information and subsequently produce a suitable OPC field by using that information to pattern a spatial light modulator.

The DOPC method has several intrinsic advantages over non-linear OPC methods. First, whereas non-linear crystals are strongly dependent on wavelength, DOPC can freely work with a broad range of wavelengths. Second, DOPC provides the flexibility to render wavefront playback beyond a single OPC field. In fact, TROVE, TRACK, and TRAP all exploit this unique capability of DOPC to render complex and nuanced wavefronts. In the case of TRACK and TRAP for example, the rendered wavefront is actually a differential DOPC wavefront. Third, and perhaps most importantly, the DOPC method has the intrinsic ability to achieve a fluence reflectivity greater than unity. Here we define fluence reflectivity as the ratio between the total amount of light that one can play back on the conjugate wavefront to the total

amount of scattered light required to determine the conjugate wavefront in the first place. While nonlinear OPC methods can in principle provide gain enhancement by temporally squeezing the playback photon packet [19], a practical and useful approach to deliver large amounts of energy over an extended period of time has not been demonstrated.

Currently, the DOPC method does have a significant disadvantage versus nonlinear OPC methods – response speed. Recently, nonlinear methods with system response latencies on the order of milliseconds have been reported [20, 21]. In contrast, DOPC systems reported thus far have response times on the order of hundreds of milliseconds or more [22]. This slow response is due to the use of slow liquid crystal spatial light modulators and conventional personal computer (PC) based data transfer. Fast response speed is a key criterion if we are to apply OPC methods usefully for *in vivo* applications in thick samples. This is due mainly to the dynamic nature of biological tissue caused by the constant motion of the scatterers within. This rate of change is dependent both on sample thickness and the degree of immobilization. As a reference point, the scattered field of 532 nm light through an unclamped living mouse skin flap has a speckle decorrelation time of $\sim$ 30 ms. When the same tissue is clamped, this decorrelation time increases to $\sim$ 300 ms. [22].

The primary goal of this paper is to show that the use of a high speed DMD (digital mirror device) and FPGA data processing allows DOPC to achieve high response speeds as well. While using the binary modulation of the DMD to accomplish wavefront shaping may seem counter-intuitive and the oblique reflection angle significantly complicates DOPC system alignment, overcoming these challenges enables us to incorporate the strengths of the DOPC while minimizing the response time of the system. In this paper, we report a novel DMD based DOPC system with a demonstrated playback latency of 5.3 ms. We demonstrate our system is capable of focusing light through 2.3 mm thick unclamped mouse dorsal skin with a decorrelation time of less than 30 ms. By repeating the DOPC procedure 50 or even more times per second, we are able to maintain the focus through the living sample indefinitely. This demonstration of sustainable focusing through a thick living sample with blood flowing through it is the first of its kind and opens the door for new applications of OPC in the deep tissue regime of live biological samples.

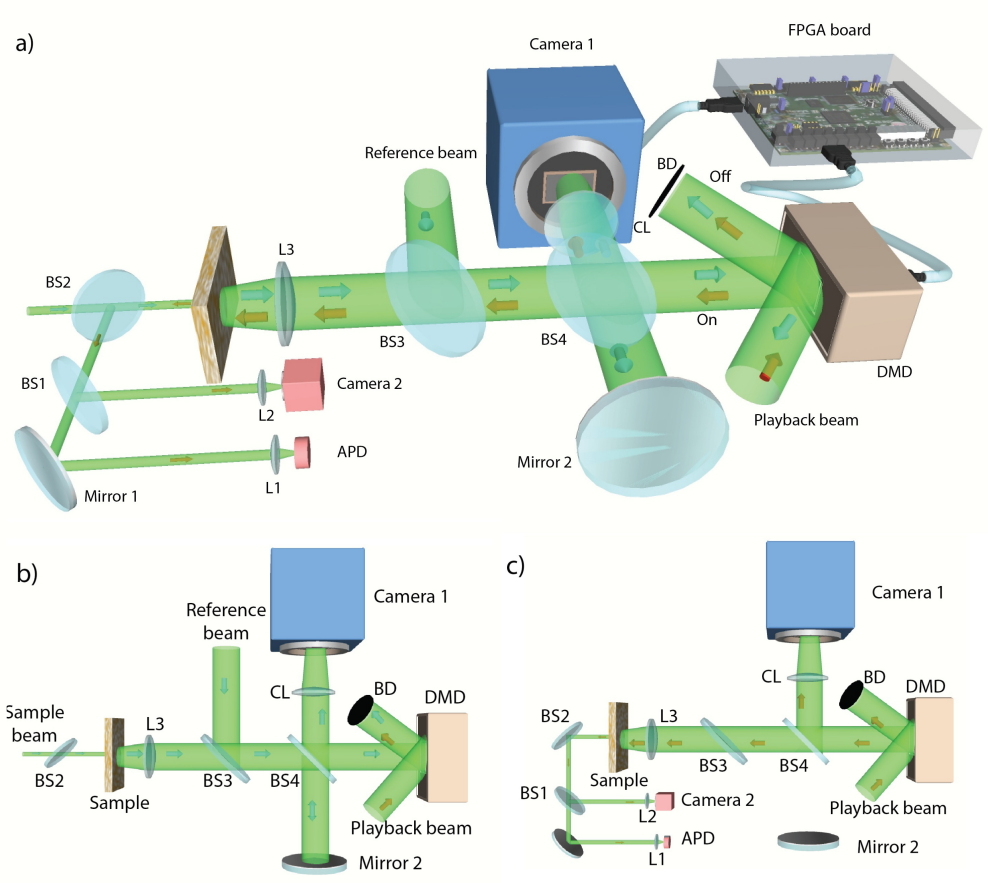

Figure 3.1: (a) Simplified schematic of the DMD based DOPC. A 2.5 mm diameter collimated beam from the laser source (Excelsior 532 nm single mode, 200 mW, Spectra-Physics) is incident onto the sample through BS2. Scattered light from the sample is collected by L3 and is combined with the reference beam by BS3. The combined reference and sample beam is reflected by BS4 and Mirror 2, passes through BS4, and is captured by Camera 1 (pco.edge 5.5, PCO-TECH). The DMD (W4100, Wintech) and Mirror 2 are aligned symmetrically with reference to BS4 and the DMD surface is imaged onto the camera sensor chip by CL (AF-S VR Micro-NIKKOR 105 mm f/2.8G IF-ED, Nikon) with pixel-to-pixel alignment. Camera 1 and the DMD are connected through a host FPGA (ViClaro IV GX Camera Link Development Kit, Microtronix). The conjugate result is observed on Camera 2 (Prosilica GX 1920, Allied Vision) and the APD (SPCM-AQRH-14, Excelitas). (b) Optical path schematic of the recording step. (c) Optical path schematic of the playback step. (L: lens, BS: beamsplitter, BD: beam dump, CL: camera lens, APD: avalanche photo diode).

3.2 Methods

A simplified schematic of the DMD based DOPC system is shown in Fig. 3.1(a). A complete optical scheme can be found in the Supplement. The light paths of the

set-up for recording and playback are shown in Fig. 3.1(b) and (c), respectively. As shown in Fig. 3.1(b), in the recording step, all the pixels on the DMD are turned off. This causes the playback beam to diffract away from Camera 1 and onto a beam dump. The sample beam and reference beams are combined at BS3, reflected by BS4 and Mirror 2, and travel back through BS4 to Camera 1 where their interference pattern is measured. In the playback step shown in Fig. 3.1(c), the FPGA processes the camera data to generate a suitable wavefront solution and sends it to the DMD which displays the corresponding phase map. The playback beam then propagates through BS4, BS3, and L3 to the sample. Meanwhile, the sample beam is blocked by a fast shutter to prevent backscattering off the sample. This playback process results in a focus observed through the sample on Camera 2 and a corresponding peak recorded by the APD. As the reference beam and playback beam are two separate beams, the fluence reflectivity is limited only by the damage threshold of DMD and the laser power. In our system, the fluence reflectivity was set at 2000. As response speed is a design priority, each major component of this system is chosen and adapted for this purpose. We will discuss each component in the following subsections.

Single shot binary phase retrieval

In order to compute the correct phase map to display on the DMD, Camera 1 captures the interference pattern between the reference field $E_{ref}(x, y)$ and the sample field $E_{sam}(x, y)$. This interference pattern can be described as $I_i(x, y) = I_{ref}(x, y) + I_{sam}(x, y) + 2\sqrt{I_{ref}(x, y)I_{sam}(x, y)}\cos|\Delta\theta|$, where $I_{ref}(x, y)$ and $I_{sam}(x, y)$ are the intensity of the reference and sample fields, respectively, and $\Delta\theta$ is their phase difference. By setting $\langle I_{sam}(x, y)\rangle \ll I_{ref}(x, y)$, $I_i(x, y)$ can be approximated as

$$I_i(x, y) \approx I_{ref}(x, y) + 2\sqrt{I_{ref}(x, y)I_{sam}(x, y)}\cos|\Delta\theta| \tag{3.2.1}$$

Then, $I_{ref}(x, y)$ can be measured independently by blocking the sample beam and by comparing it to $I_i(x, y)$, we can determine the range in which the absolute phase difference $|\Delta\theta|$ lies.

$$\begin{aligned} I_i(x, y) < I_{ref} &\rightarrow \tfrac{\pi}{2} < |\Delta\theta| \leq \pi, \\ I_i(x, y) > I_{ref} &\rightarrow 0 \leq |\Delta\theta| \leq \tfrac{\pi}{2}. \end{aligned} \tag{3.2.2}$$

In this way, the intensity of the interference pattern at a point (x, y) can be used to recover the binary phase of $E_{sam}(x, y)$ in a single-shot. In comparison, two methods commonly applied in DOPC systems, phase stepping holography [23] and off-axis

holography [24], are capable of fully recovering the sample field but sacrifice either speed or spatial resolution. While DOPC playback with binary phase information is less efficient than with perfect phase information, this small sacrifice in efficiency yields a large enhancement in response speed.

FPGA based data processing and transfer

An FPGA board (as shown in Fig. 3.2) is implemented in the DOPC system for data processing and transfer. It has a Camera Link connection directly to the recording camera and an HDMI (High Definition Multimedia Interface) connection to the DMD. This allows full frame (1920×1080) interference pattern transfer in 5.0 ms (6.8 Gb/s) and full frame size phase map transfer in 1.56 ms (1.8 Gb/s). Here, the phase map transfer time is the time from starting the binary phase data transfer to completing the stable display on the DMD. Although the DMD chip (DLP9500, TI) has a fast refreshing speed of up to 23K fps, the standard 60 Hz HDMI display interface of the W4100 board limits the performance. To fully utilize the fast response speed of the DMD, we designed custom firmware for the FPGA controller (Virtex 5, Xilinx) on the W4100 board. With a custom HDMI protocol, we encode 24 binary pixels into one 24 bit RGB pixel of standard HDMI allowing us to achieve fast binary image transfer. In the recording step, the FPGA board reads out the interference image from the recording camera and retrieves the phase in parallel. Once the phase map is ready and has been adjusted to compensate for the curvature of the DMD (see Supplement), it is transferred to the DMD board and displayed. Compared to a computer, the FPGA allows for greatly accelerated data processing

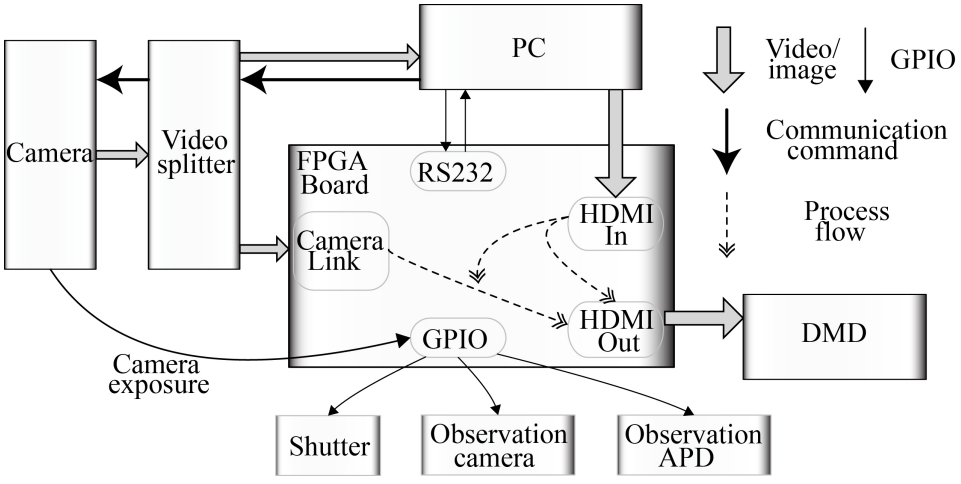

Figure 3.2: Functional schematic of FPGA based DOPC.

and transfer speeds. When using a PC as the host processor in DOPC, the multi-task scheduling and hardware access wrapping in modern operating systems limits the latency between recording and playback steps to a minimum of around two hundred milliseconds [22]. In contrast, as an FPGA inherently has a highly parallel computing capacity, the processing latency for binary phase retrieval is eliminated by overlapping the phase processing with the camera image transfer. In addition to the speed of the FPGA system, our setup allows for data collection and processing to be seamlessly switched to the PC for time-insensitive optical system debugging and pixel-pixel alignment between the recording camera and the DMD. To achieve this, a video splitter (CLV-402, Vivid Engineering) is implemented to switch the output of the recording camera between the PC and the FPGA. An HDMI interface is also set up between the PC and FPGA to allow the PC to transfer phase maps to the DMD.

DMD based phase conjugation

When a conjugate phase map is displayed on the DMD, the DMD implements a binary amplitude modulation scheme [25] to construct a conjugate focus through the tissue. Here we will analyze the binary phase modulation scheme, which although essentially identical to binary amplitude modulation, is formulated here to easily integrate into the framework of phase conjugation [26]. When using the DMD for

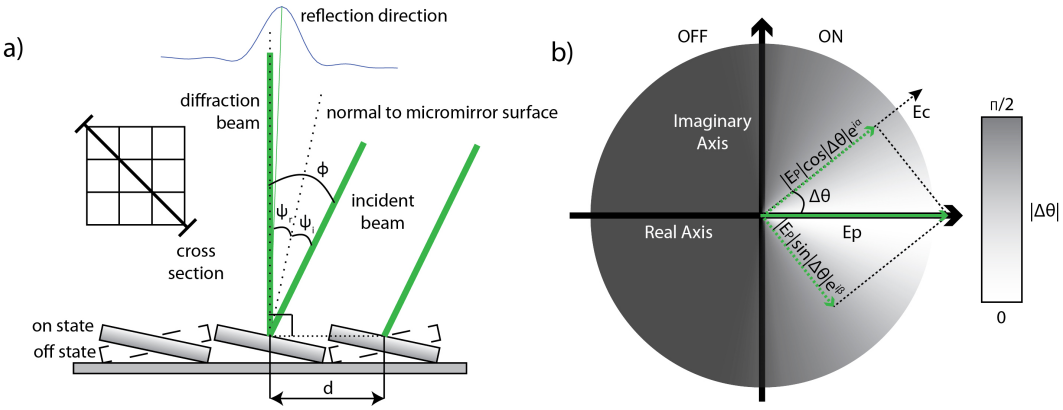

Figure 3.3: (a) DMD diffraction demonstration. (b) Binary phase modulation of DMD. E_p is the field played back by the DMD, E_c is the desired phase conjugate field, and $\Delta\theta$ is the phase difference between E_c and E_p. When a pixel of the DMD is turned on, it plays back the phasor E_p which can be decomposed into two orthogonal components. One is in the direction of the desired phase conjugate field E_c with an amplitude modulated by $\cos|\Delta\theta|$ and contributes to the focus. The other component orthogonal to E_c is modulated by $\sin|\Delta\theta|$ and contributes to the background.

light modulation, every individual micro-mirror acts as a diffractive element and together the whole DMD acts as a 2D blazed grating. As shown in Fig. 3.3(a), when a pixel is turned on, it will tilt 12° clockwise in the diagonal direction. This oblique angle complicates the DOPC system design, as it is a challenge that does not exist for SLM based DOPC systems. To address this, we choose to illuminate the DMD with an appropriately tilted light field such that the diffracted light propagates perpendicularly with respect to the surface of the DMD. This propagation direction is subject to the blazed grating equation, which is a function of the center-to-center distance between the individual micro-mirrors in the array (d), the angle of incidence (ϕ) with respect to the DMD surface normal, the wavelength (λ), and the diffraction order (n). Setting the diffraction angle to fix the diffraction direction normal to the DMD surface yields a simplified form of the blazed grating equation:

$$d \sin \phi = n\lambda. \tag{3.2.3}$$

However, in order to achieve the maximum possible intensity of the diffraction beam, the incident angle should be chosen so that the central peak of the sinc^2 envelope determined by the direction of the specular reflection from each individual micro-mirror matches as closely with the direction normal to the DMD surface as possible. Combining the simplified blazed grating equation above with the law of reflection ($\psi_i = \psi_r$) which determines the location of the sinc^2 envelope, we can solve for the incident angle in order to maximize the intensity of the diffracted beam. Given a light source with a wavelength of 532 nm and $d = 10.8\sqrt{2}$ µm from the dimensions of the DMD, we solve to find the optimum incident angle and diffraction order to be $\phi = 24.7°$ and $n = 12$, respectively.

After optimizing the alignment of the DMD in the DOPC system, we fit the binary amplitude modulation of the DMD into a phase conjugation framework. Since the diffracted light from the DMD has a uniform phase, we can spatially choose whether it is played back or not by manipulating each pixel's state. As shown in Fig. 3.3(b), without loss of generality, we suppose playback beam E_p has uniform amplitude A and phase zero. For an electric field $E_c = |E_c|e^{i\alpha}$ which is the optimal phase conjugate solution to be played back, there is a phase difference $\Delta\theta$ between E_c and E_p. Using the binary phase retrieval algorithm described earlier, we determine whether an individual pixel should be played back. If $|\Delta\theta|$ is less than $\pi/2$, the corresponding pixel is turned on. Otherwise, it is turned off. When we turn on the pixel, E_p can be decomposed into orthogonal phase vectors, as shown in Fig. 3.3(b).

This allows us to derive the phase modulation function of the DMD in DOPC as

$$f\left(|\Delta\theta|\right) = \begin{cases} 0, & \frac{\pi}{2} < |\Delta\theta| \leq \pi \\ \cos|\Delta\theta|e^{i\alpha} + \sin|\Delta\theta|e^{i\beta}, & 0 \leq |\Delta\theta| \leq \frac{\pi}{2} \end{cases}. \tag{3.2.4}$$

This means that when $0 \leq |\Delta\theta| \leq \frac{\pi}{2}$ and a pixel of the DMD is turned on to represent a certain E_c, we will play back the electric field $|E_p|\cos|\Delta\theta|e^{i\alpha}$, which has the phase of E_c and amplitude modulated by $\cos|\Delta\theta|$, along with an orthogonal electric field $|E_p|\sin|\Delta\theta|e^{i\beta}$ with amplitude modulated by $\sin|\Delta\theta|$. The cosine term will be played back as a correct component of the phase conjugate field, and construct a peak. The sine term, which has an orthogonal phase, will make no contribution to the peak recovery and will form a background in the playback field. Following a similar derivation in reference [13, 25] (see details in the Supplement), we find the theoretical peak to background ratio (PBR) for DMD based DOPC to be

$$\text{PBR} = \frac{1/2 + (N-1)/2\pi}{M} \approx \frac{N}{2\pi M}, \tag{3.2.5}$$

where M is the number of modes in the focus, and N is the number of controllable modes on DMD. Implementing the DMD in the DOPC setup allows our system to save more than 10 milliseconds for conjugate phase display compared to the time reported in LC-SLM based DOPC systems [13, 15, 22]. When a voltage is applied to an LC-SLM based on nematic liquid crystal technology, it usually takes over 10 milliseconds to turn to the specified direction. This limits the refresh rate to tens of Hz. In contrast, a DMD, which is based on MEMS technology, has a response time around 18 µs with a 23 kHz refresh rate [27], over two orders of magnitudes faster than typical LC-SLMs.

Workflow of fast DOPC

The workflow of our system is shown in Fig. 3.4. Prior to operation, the reference beam intensity distribution is recorded. Then the DOPC loop starts. At the beginning of every loop, all the DMD pixels are turned off and the interference pattern is captured. Once the intensity of a pixel is transferred from the camera and stored by the FPGA, its binary phase is processed and recovered. After all the pixels are processed, the binary phase map is transferred to the DMD and displayed for a designated time. During the process, the fast shutter, exposure of the observation camera and the recording of the APD signal are synchronized by the FPGA GPIOs. Each loop is synchronized by the exposure and transfer signals of the recording camera. As shown in Fig. 3.4, the playback latency is the sum of the time required

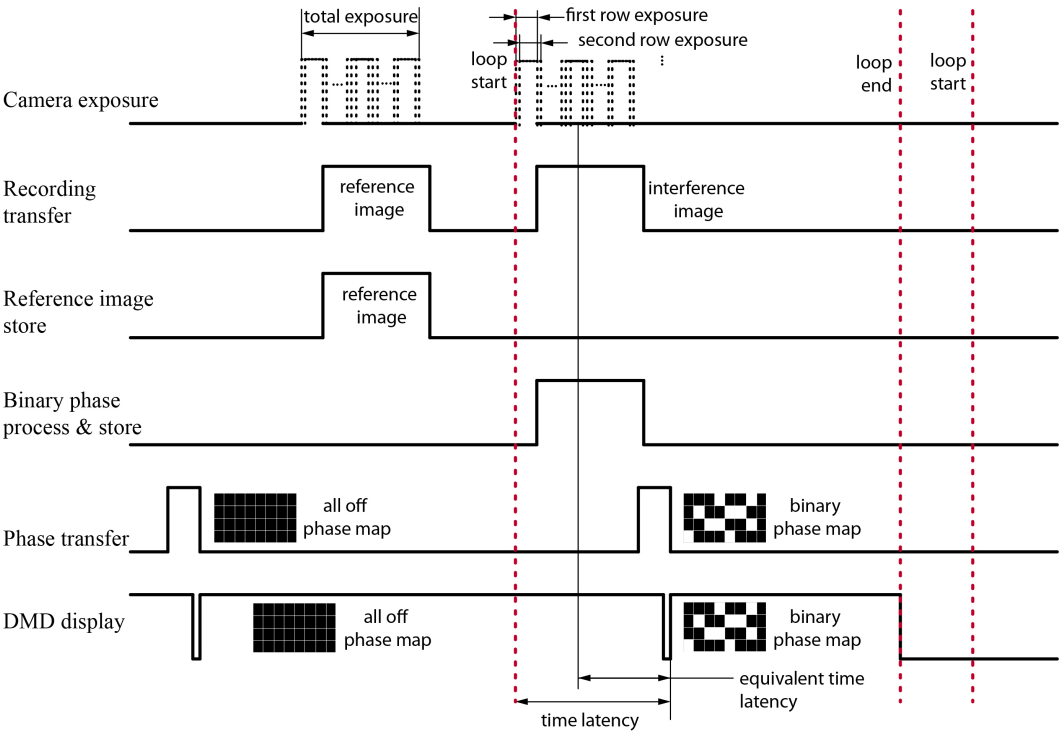

Figure 3.4: Workflow of FPGA based DOPC.

by the recording exposure, data transfer from the recording camera to the FPGA (recording transfer), and binary phase transfer from the FPGA to the DMD (phase transfer). For a full frame size of 1920×1080 (up to 2.1×10^6 controllable modes) and 0.5 ms exposure, the time from the start of the exposure to playback is 7.06 ms. Rolling shutter is used for the recording exposure, so neighbor rows start to expose successively with a 9.17 µs delay. The time latency is calculated from the average exposure start time to the time playback starts. The latency is quantified by the following experiments.

3.3 Results

Playback Latency Quantification

To evaluate the actual playback latency of our system, DOPC experiments were conducted on tissue samples with a controllable decorrelation time using a moving tissue strategy [20]. A piece of 3 mm thick chicken breast (μ_s = 30/mm, g = 0.965) was sandwiched between two 1 mm thick glass slides. In the middle layer, a 3 mm thick U shape spacer was placed surrounding the chicken breast to guarantee its thickness and mobility (as shown in Fig. 3.5(a). During the experiment, samples were changed before they dried out to ensure their scattering properties. The whole

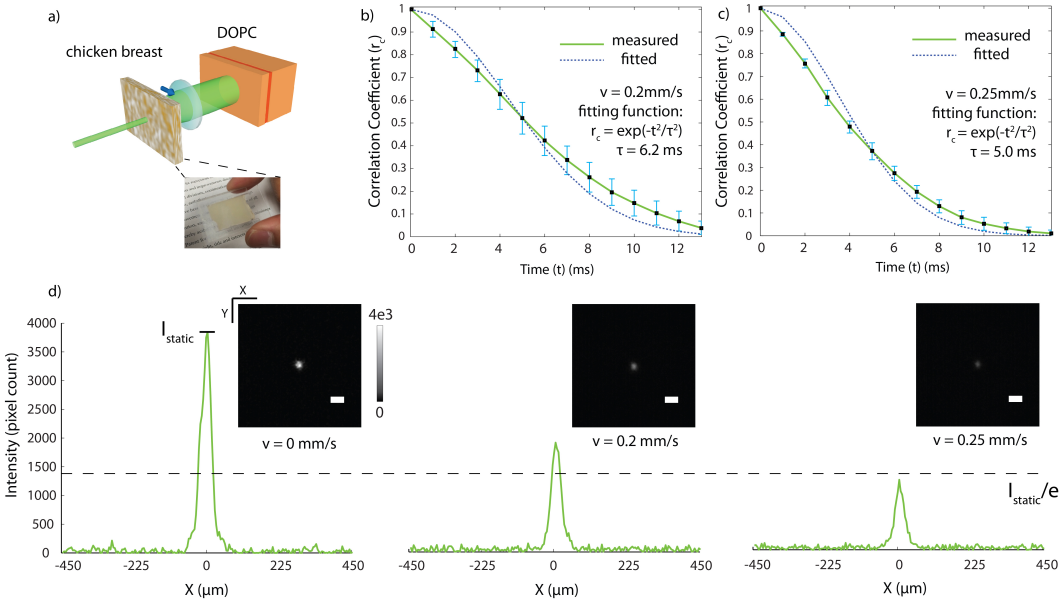

Figure 3.5: (a) Moving sample setup. (b),(c) Moving sample speckle decorrelation curves at lateral velocity 0.2 mm/s and 0.25 mm/s. Error bars indicate standard deviation over 10 datasets. (d) Conjugate focus images and cross section peak plots when the sample was static, moving at 0.2 mm/s and 0.25 mm/s.

sample was held by a translation stage with a motorized actuator (LTA-HS, Newport) to generate different decorrelation times by varying the lateral velocity.

The decorrelation time of the tissue itself was several seconds [13], which was negligible in several milliseconds. To avoid the effects of slow decorrelation when the stage was accelerating, experiments were done when the stage had reached full speed. Tissue decorrelation curves when lateral velocity was set to 0.2 mm/s and 0.25 mm/s are shown in Fig. 3.5(b) and (c), respectively. Here we define the decorrelation time τ as the time t when the speckle correlation coefficient r_c decreases to $1/e$. Fitting with a Gaussian function $r_c = e^{-t^2/\tau^2}$ [28], we can find the decorrelation time τ is 6.2 ms and 5.0 ms for each case. The conjugate focus results for the two cases are shown in Fig. 3.5(d). Given that the motion induced degradation ratio of PBR is identical to the drop in the speckle correlation coefficient [22], it is straightforward to conclude that the system playback latency is identical to the decorrelation time of the sample when the PBR achieved on a moving sample is $1/e$ of the static PBR. From the results, the PBR is 88 for 0.2 mm/s and 56 for 0.25 mm/s. Comparing these to the value of the static PBR divided by e ($\sim$ 65), we can tell the time latency is slightly more than 5.0 ms, which can be accurately calculated as 5.3 ms.

OPC Efficiency Quantification

As shown in Eq. 3.2.5, PBR is related to both number of input modes (N, number of speckle grains on DMD) and number of output modes (M, number of speckle grains in the focus). Therefore, it is not a fair comparison to quantify DOPC performance merely by the PBR for different numbers of output modes. However, OPC efficiency, which is ratio of PBR achieved on a system to theoretical PBR, sets a suitable standard for different systems. To evaluate the OPC efficiency of our system, we used our DOPC system to focus light through an opal diffuser (10DIFF-VIS, Newport). Based on the derivation of DMD based conjugation and the measured interference pattern on the recording camera, we determined the speckle size to be 4 pixels wide on the DMD. Since the DMD has 1920×1080 pixels, the number of optical modes we can access with the DMD equals 1.3×10^5. To determine the number of modes in the focus, we examined the conjugate focus through the sample. When the conjugate beam was played back, we observed a focus on the observation camera with a PBR of 630 and full width half maximum (FWHM) of 45 µm as shown in Fig. 3.6. When we displayed a random pattern on the DMD, the speckle FWHM was 13 µm, computed from the autocorrelation of the speckle pattern. From these two measurements, we can find that the number of modes in the focus is ~ 12. From the PBR equation, we calculated the optimal PBR as $1.3 \times 10^5/(12 \cdot 2\pi) \approx 1700$, which means our system performance has an efficiency of 37%.

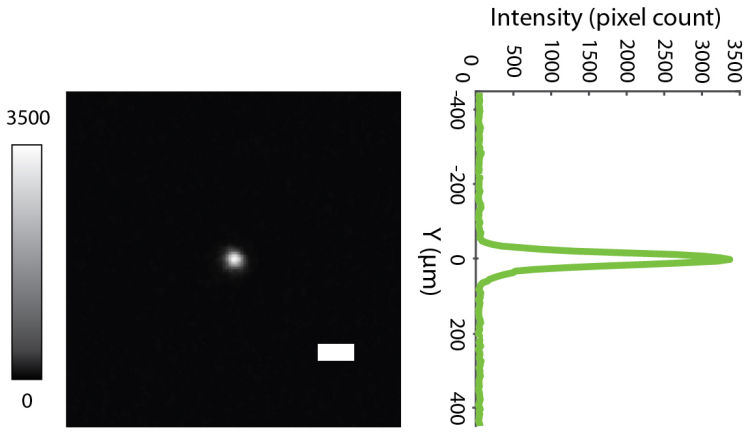

Figure 3.6: PBR quantification. Scale bar is 100 µm.

In vivo Experiments

In vivo experiments were demonstrated by focusing through the dorsal skin of a living mouse. For the *in vivo* sample, a regular white lab mouse was shaved on the dorsal skin flap. Then its dorsal skin was mounted to a clip device. Isoflurane was implemented as the inhalational anesthesia both in preparation and during the experiment. All of these procedures and the dosage of chemicals followed protocols of the Institutional Animal Care and Use Committee at the California Institute of Technology.

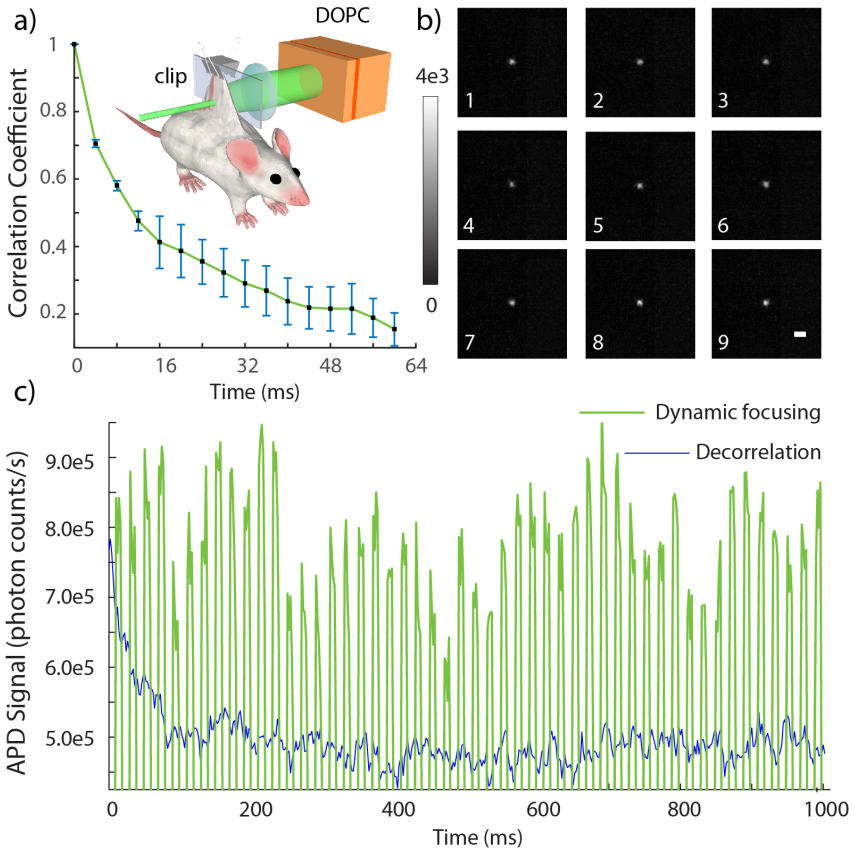

Figure 3.7: (a) Clipped mouse dorsal skin setup and speckle decorrelation curve of *in vivo* tissue. Error bars indicate standard deviation over 10 datasets. (b) Continuous conjugate foci through clipped sample. (c) APD plot for sustainable foci and decorrelation focus. Scale bar is 100 µm. In the experiment, to accurate distinguish the focus intensity from background in APD signal a background (I_b) was measured first when the focus totally vanished, which is 5×10^5 in the APD plot.

As shown in Fig. 3.7(a), a clip fixed the upper edge of the skin on a transparent plastic plate, which was placed at the sample position. In this way, the bottom of

the dorsal skin was in a natural free status. The sample beam was incident onto the bottom part of the skin, which had a thickness of around 2.3 mm. Before DOPC was applied, a series of scattering speckle patterns from the tissue were captured by the recording camera to analyze the tissue decorrelation time and form the decorrelation curve plotted in Fig. 3.7(a). From this curve we can tell its decorrelation time is 28 ms, where the decorrelation time is defined as the time when the speckle correlation coefficient decreases to $1/e$. After that, DOPC was conducted with an exposure time of 0.5 ms on the recording camera, at a refresh rate of 50 Hz and a playback holding time of 10 ms. A series of images from the observation camera triggered by the playback signal with an exposure time of 3 ms are included in Fig. Fig. 3.7(b) and Media 1 (5 seconds video) along with a corresponding APD plot in Fig. 3.7(c). From the focus images and APD plot, we can tell a clear focus was constructed and maintained through unrestricted tissue on a living animal. From the average of 10 images we calculate the PBR is 180. For our system, a refresh rate up to 100 Hz with flexible holding time is achievable. It should also be noted that while in the middle of the movie we can observe a short failing of conjugation due to severe body movement from respiration, not due to the decorrelation of the tissue itself.

3.4 Discussion and Conclusion

In this work, we demonstrated the first DMD based DOPC system. This system is capable of playback with latency on the order of milliseconds – a speed improvement of approximately two orders of magnitude over prior DOPC systems. Using the fast DOPC system, we demonstrated the ability to create an indefinitely sustainable focus through unrestricted tissue on a living animal – a capability that has never been previously reported for any OPC experiments. While non-linear approaches can, in principle, provide this capability as well, this DOPC approach is direct and can provide a greater than unity fluence reflectivity. Our system can achieve greater than 2000 fluence reflectivity which is crucial for thick *in vivo* tissue application. In our case, the playback beam is set to $\sim$ 10 mW and the total fluence of the scattered light from the sample is $\sim$ 5 μW. We further quantified our playback latency as 5.3 ms. While the background due to unmodulated light will need to be addressed in the binary phase retrieval method, it will be straightforward to extend this technology to existing OPC based technology such as TRUE, TROVE, TRACK, etc. and apply it in living tissue for biological applications. Compared to phase only OPC, DMD based DOPC encounters a PBR reduction of 80% (from $\pi/4$ to $1/2\pi$). However, for the DMD based DOPC system the PBR can be further improved by tuning $I_{ref}/\langle I_{sam}\rangle$

in the single-shot binary phase retrieval. For example, suppose I_{ref} and I_{sam} have intensities on the same order of magnitude, then the binary phase retrieval equation will be

$$\mathrm{DMD}(x,y) = \begin{cases} 1, & I_i(x,y) < I_{ref}(x,y) \rightarrow |\alpha - \pi| < \phi \\ & \phi = \arccos\left(\frac{1}{2}\sqrt{I_{ref}/I_{sam}}\right) < \frac{\pi}{2} \\ 0, & \text{else} \end{cases} . \tag{3.4.1}$$

As I_{sam} follows a Rayleigh distribution [29], by comparing the intensity difference we can statistically select a smaller phase range 2ϕ than π. The theoretical PBR in this condition (detailed derivation in the Supplement) is a unimodal function of $I_{ref}/\langle I_{sam}\rangle$, which achieves up to 12.6% higher PBR at $I_{ref}/\langle I_{sam}\rangle = 1.61$ than when $I_{ref} \gg \langle I_{sam}\rangle$. In our experiments, we selected this condition as closely as possible. However, due to the dynamic and heterogeneous nature of biological tissue, it is likely that the PBR could have been further improved by fine tuning this ratio to more accurately select this optimal condition.

Recently, focusing through thin *ex vivo* tissue samples (200 µm chicken breast) was demonstrated at sub-microsecond timescales by using the self-organization of an optical field inside a multimode laser cavity [30]. Despite its speed, the approach demonstrated only around 1000 controllable modes and the number of controllable modes will significantly diminish for thicker samples. This hinders its applications to thick *in vivo* tissue. In addition, the technique relies on optical feedback from the target position, preventing it from being extended to non-invasive techniques with a guide star to focus inside biological tissue.

The flexibility of the DOPC system also provides the additional ability to trade off controllable modes for reduced playback latency. Since the time for recording and phase transfer is proportional to frame size, shrinking the frame size can further decrease the playback latency. For example, if the frame size is reduced to 1920×70, the playback latency is below 1 ms. Although the PBR will also decrease for smaller frame sizes, up to 1.3×10^5 controllable pixels are still available at a frame size of 1920×70. In practice, we could balance the number of controllable modes (PBR) and time latency based on the decorrelation properties of different samples.

The architecture of our DOPC system also has the potential to be applied in microsecond scale wavefront shaping. Currently, the playback latency is determined by the sum of the time required by the recording exposure, data transfer from the camera to the FPGA, and binary phase transfer from the FPGA to the DMD. As the

development of fast and sensitive scientific cameras continues, the exposure time and recording transfer time can be reduced by orders of magnitudes. Here we have used an exposure time of 0.5 ms, the minimum exposure time available for the camera, which may be reduced to tens of microseconds or even several microseconds in the future. Meanwhile the sample beam intensity has to match the shorter exposure. This will be hindered by tissue absorption which can be addressed by switching from the 532 nm laser source to near infrared wavelengths, which have orders of magnitude lower tissue absorption. The minimal wavelength dependency of the DOPC system compared to non-linear OPC systems allows this conversion to a different wavelength regime to be direct. We anticipate that with near infrared light, *in vivo* DOPC applications on tissue centimeters thick can be realized. Finally, a phase transfer time around 50 µs can be realized by using a better FPGA (e.g. Altera Stratix V) and a custom designed data transfer interface to match the maximum refresh rate of the DMD (23 kHz). With the development of faster DMD devices, this time may be further reduced to several microseconds. As the decorrelation rate of tissue drastically increases with thickness, such improvements would ultimately enable wavefront shaping to be applied for optogenetics in the whole brain, *in vivo* deep tissue imaging, and photodynamic therapy for internal organs.

Appendix

Optical Diagram

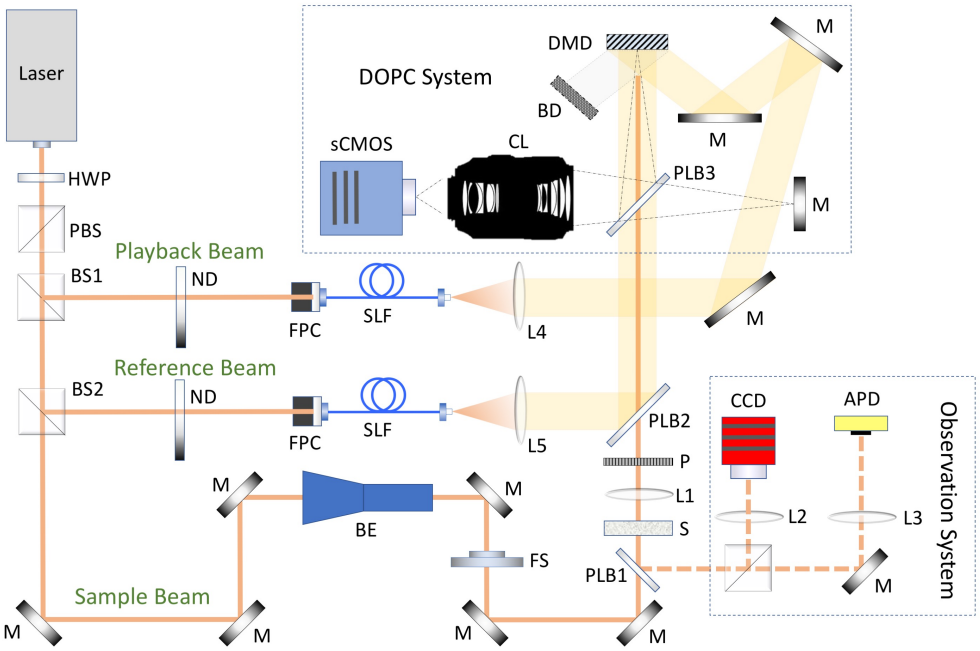

Figure 3.8: Setup diagram. BD: beam dump, BE: beam expander, BS1: 90/10 cube beamsplitter, BS2: 90/10 cube beamsplitter BS3: 50/50 cube beamsplitter, CL: camera lens (Nikon AF-S VR Micro-NIKKOR 105 mm f/2.8G IF-ED), DMD: digital micromirror device (W4100, Wintech), FPC: fiber port connector, HWP: half wave plate, L1: 50 mm planoconvex lens, L2: 100 mm planoconvex lens, L3: 100 mm planoconvex lens, L4: 150 mm planoconvex lens, L5: 15 mm planoconvex lens, M: mirror, ND: neutral density filter, PLB1: 50/50 plate beamsplitter, PLB2: 90/10 plate beamsplitter PLB3: 50/50 plate beamsplitter FS: fast shutter, PBS: polarized beam splitter, P: polarizer, S: sample, SLF: spatial light filter-single mode polarization maintaining fiber.

DMD Curvature Compensation

The performance of an OPC system is highly dependent on the fidelity between the playback and recording wavefronts. Therefore, curvature of the DMD surface must be taken into account and digitally corrected by finding a compensation phase map for the DMD and adding it to the playback phase map. The compensation phase map is acquired in three steps. First, the playback beam is turned off and the intensity of the reference beam is captured. Second, all the DMD pixels are set to the "on" position, the playback beam is turned on, and the interference pattern between the reference beam and playback beam is captured. Third, the single-shot binary phase

retrieval technique is used to compute the binary wavefront difference between the two beams and find the wavefront distortion due to the curvature of the DMD. In this case, the playback beam is modulated by the curved surface of the DMD and acts as the sample beam in the binary phase retrieval computation. The result of this calculation is a binary phase map which is then applied to each subsequently calculated wavefront in the DOPC procedure before playback.

PBR Derivation

The theoretical performance of optical phase conjugation is well described in framework of Vellekoop [26]. Scattering by tissue essentially maps the input electric field to the output electric field and can be described by a transmission matrix. Assuming the incident electric field on a scattering sample A is E_a and the electric field coming out from the other surface B is E_b, the transformation between E_a and E_b can be described as

$$E_b = T_{AB} E_a, \tag{3.4.2}$$

where T_{AB} is the total transmission matrix describing the propagation of E_a from plane A to B. In perfect phase conjugation, T_{AB} is unitary, which reflects the time symmetry $(T_{AB})^{\dagger} = (T_{AB})^{-1} = (T_{BA})^{*}$. If we play back conjugate field E_a^* on plane B, the outcome E_a' on plane A will be,

$$E_a' = T_{BA} E_b^* = T_{BA} \left(T_{AB} E_a\right)^* = T_{BA} T_{BA}^{-1} E_a^* = E_a^*, \tag{3.4.3}$$

where "†" stands for conjugate transpose. While in practice T_{AB} is only part of the total transmission matrix, we can still derive an approximate phase conjugation solution so that E_a^* is played back on surface A with a background. For a single mode input E_a with unit intensity (without loss of generality), the phase conjugate field in the original position a with background m at plane A will be

$$E_a' = \sum_{b=1}^{N} t_{ba} E_b^* = \sum_{b=1}^{N} t_{ba} \left(t_{ab} E_a\right)^* = E_a^* \sum_{b=1}^{N} |t_{ab}|^2 \tag{3.4.4}$$

$$E_{m,m\neq a}' = \sum_{b=1}^{N} t_{bm} E_b^* = \sum_{b=1}^{N} t_{bm} \left(t_{ab} E_a\right)^* = E_a^* \sum_{b=1}^{N} t_{bm} t_{ab}^*. \tag{3.4.5}$$

In the case of phase-only modulation with amplitude A, the phase conjugate field is

$$\begin{aligned} E'_a &= A\sum_{b=1}^{N} t_{ba} e^{i\cdot\arg\left(E_b^*\right)} = A\sum_{b=1}^{N} t_{ab} e^{i\cdot\arg\left(t_{ab}^* E_a^*\right)} \\ &= AE_a^*\sum_{b=1}^{N} |t_{ab}| \end{aligned} \tag{3.4.6}$$

$$E'_{m,m\neq a} = A\sum_{b=1}^{N} t_{bm} e^{i\cdot\arg\left(E_b^*\right)} = AE_a^*\sum_{b=1}^{N} t_{bm} e^{i\cdot\arg\left(t_{ab}^*\right)}. \tag{3.4.7}$$

If a DMD is used as the spatial light modulator in DOPC, the expression for the phase conjugate field at the original position needs to be modified to account for the binary modulation of the DMD. This can be written as

$$E'_a = \sum_{b=1}^{N} t_{ba} A f\left(|\Delta\theta|\right), \tag{3.4.8}$$

where $|\Delta\theta| = \left|\alpha - \theta_p\right|$, $\alpha = \arg\left(E_b^*\right)$, θ_p is the phase of playback light from the DMD, and $f\left(|\Delta\theta|\right)$ is the phase modulation function of the DMD given by

$$f\left(|\Delta\theta|\right) = \begin{cases} 0, & |\Delta\theta| > \phi \\ \cos|\Delta\theta| e^{i\alpha} + \sin|\Delta\theta| e^{i\beta}, & |\Delta\theta| \leq \phi \end{cases}, \tag{3.4.9}$$

where β is the argument of the decomposed phasor orthogonal to $e^{i\alpha}$. Pixels with an absolute phase difference less than or equal to the upper bound ϕ are turned on for playback. With phase stepping or off-axis holography, we can easily select any ϕ. When $0 \leq |\Delta\theta| < \phi$, we can decompose E'_a into two terms. The first term is a phase only conjugation term modulated by $\cos|\Delta\theta|$. As the phase distribution of speckles is uniform within the selected range, the second term, which has an orthogonal phase, will make no contribution to recovery of the peak. From the above, we can intuitively come to the result that DMD based DOPC is phase only DOPC with an amplitude modulated by the cosine term, as shown in Eq. 3.4.10 below.

$$\begin{aligned} E'_a &= \sum_{b=1}^{N} t_{ba} A f\left(|\Delta\theta|\right) \\ &= \sum_{b=1}^{N} t_{ba} A e^{i\cdot\arg\left(E_b^*\right)} \cos|\Delta\theta| \left(|\Delta\theta| \leq \phi\right) \\ &= \sum_{b=1}^{N} t_{ba} A e^{i\cdot\arg\left(t_{ab}^* E_a^*\right)} \cos|\Delta\theta| \left(|\Delta\theta| \leq \phi\right) \\ &= AE_a^*\sum_{b=1}^{N} |t_{ab}| \cos|\Delta\theta| \left(|\Delta\theta| \leq \phi\right). \end{aligned} \tag{3.4.10}$$

Since the transmission matrix elements can be assumed to follow complex circular Gaussian distribution [26], the amplitudes of the individual matrix elements $|t_{ab}|$ follow a Rayleigh distribution $|t_{ab}|$: Rayleigh(σ) and their intensities $|t_{ab}|^2$ follow an exponential distribution $|t_{ab}|^2 \sim e^{-1/(2\sigma^2)}$ with $2\sigma^2$ as the ensemble average intensity of each element. The absolute phase difference $|\Delta\theta|$ follows a uniform distribution from 0 to π. Then, based on the derivation of phase-only phase conjugation described by Wang [13], the peak intensity and its ensemble average are calculated as

$$\begin{aligned} I'_a &= \left| A \sum_{b=1}^{N} |t_{ab}| \cos|\Delta\theta| \left(|\Delta\theta| \le \phi\right) \right|^2 \\ &= A^2 \sum_{b=1}^{N} |t_{ab}|^2 \left(\cos|\Delta\theta| \left(|\Delta\theta| \le \phi\right)\right)^2 \\ &+ A^2 \left\{ \sum_{b=1}^{N} \sum_{b' \neq b}^{N} |t_{ab}|\,|t_{ab'}| \left(\cos|\Delta\theta| \left(|\Delta\theta| \le \phi\right)\right)^2 \right\}^2 . \end{aligned} \tag{3.4.11}$$

$$\begin{aligned} \langle I'_a \rangle &= A^2 N \left\langle |t_{ab}|^2 \right\rangle \left\langle \left(\cos|\Delta\theta| \left(|\Delta\theta| \le \phi\right)\right)^2 \right\rangle \\ &+ A^2 N(N-1) \left\langle |t_{ab}|^2 \right\rangle \left\langle \cos\left(|\Delta\theta|\right) \left(|\Delta\theta| \le \phi\right) \right\rangle^2 \\ &= 2NA^2\sigma^2 \left(\frac{\sin 2\phi/2 + \phi}{2\pi} \right) \\ &+ \frac{\pi}{2} N\left(N-1\right) A^2\sigma^2 \left(\frac{\sin\phi}{\pi} \right)^2 \end{aligned} \tag{3.4.12}$$

Similarly, the background can be calculated as

$$E'_{m,m\neq a} = \sum_{b=1}^{N} t_{bm} A e^{i\theta_p} \left(|\Delta\theta| \le \phi\right) \tag{3.4.13}$$

$$I'_{m,m\neq a} = A^2 \left| \sum_{b=1}^{N} t_{bm} \left(|\Delta\theta| \le \phi\right) \right|^2 \tag{3.4.14}$$

$$\begin{aligned} \left\langle I'_{m,m\neq a} \right\rangle &= A^2 \left\langle \left| \sum_{b=1}^{N} t_{bm} \left(|\Delta\theta| \le \phi\right) \right| \right\rangle \\ &= 2NA^2\sigma^2 \frac{\phi}{\pi}. \end{aligned} \tag{3.4.15}$$

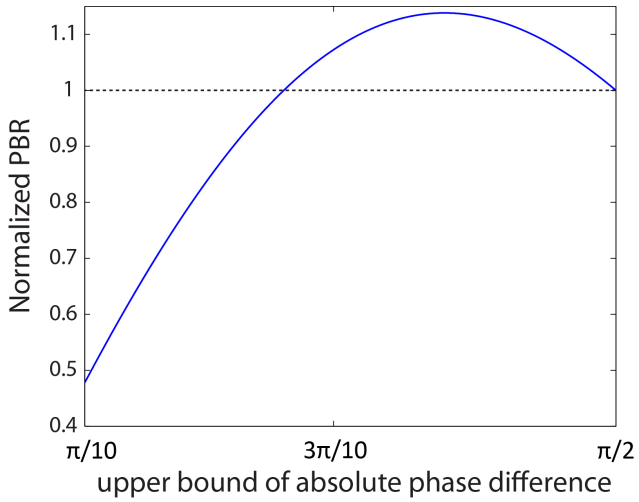

Figure 3.9: Normalized theoretical PBR with respect to ϕ (the upper bound of the absolute phase difference).

Putting these two expressions together, we can find the PBR to be

$$\begin{aligned}
\mathrm{PBR}_{\mathrm{DMD}} &= \frac{\langle I'_a \rangle}{\left\langle I'_{m,m\neq a} \right\rangle} \\
&= \frac{2NA^2\sigma^2 \left(\frac{\sin 2\phi/2+\phi}{2\pi}\right) + \frac{\pi}{2}N\left(N-1\right)A^2\sigma^2\left(\frac{\sin\phi}{\pi}\right)^2}{2NA^2\sigma^2\frac{\phi}{\pi}} \\
&= \frac{1}{2} + \frac{\sin 2\phi + (N-1)\sin^2\phi}{4\phi} \\
&\approx \frac{N\sin^2\phi}{4\phi}.
\end{aligned} \tag{3.4.16}$$

For $\phi = \pi/2$, the PBR is

$$\mathrm{PBR}_{\mathrm{DMD},\phi=\pi/2} = \frac{1}{2} + \frac{(N-1)}{2\pi} \approx \frac{N}{2\pi}, \tag{3.4.17}$$

which is consistent with derivation in iterative binary iterative wavefront optimization [25]. As shown in Fig. 3.9, the PBR is a unimodal function of ϕ, reaching its maximum at $\phi = 0.371\pi$, with a 13.8% higher value than at $\phi = \pi/2$. When there are M nonzero optical modes in focus, the PBR is scaled by M so that the new PBR is

$$\mathrm{PBR}_{\mathrm{DMD}} \approx \frac{N\sin^2\phi}{4M\phi}. \tag{3.4.18}$$

Single-shot Binary Phase Retrieval

Using a reference beam with an electric field $E_{ref}(x, y)$ (whose intensity is $I_{ref}(x, y)$ and phase is zero without loss generality), the complex information (phase and amplitude) of the sample field $E_{sam}(x, y)$ (whose intensity is $I_{sam}(x, y)$ and phase is α) is coupled into the intensity of their interference pattern I_i as

$$I_i(x, y) = I_{ref}(x, y) + I_{sam}(x, y) + 2\sqrt{I_{ref}(x, y)I_{sam}(x, y)}\cos\alpha. \tag{3.4.19}$$

For phase retrieval in DMD based DOPC, only the condition $\frac{\pi}{2} < \alpha < \frac{3\pi}{2}$ or $-\frac{\pi}{2} \leq \alpha \leq \frac{\pi}{2}$ is needed. This allows a single-shot binary phase retrieval technique to be used to determine which DMD pixels should be turned on.

$$\mathrm{DMD}(x, y) = \begin{cases} 1, & I_i(x, y) < I_{ref}(x, y) \rightarrow B(\alpha) = \pi \\ 0, & \text{else} \rightarrow B(\alpha) = 0 \end{cases}. \tag{3.4.20}$$

It can be shown that $I_i(x, y) < I_{ref}(x, y) \rightarrow \frac{\pi}{2} < \alpha < \frac{3\pi}{2}$. For this phase range of interest, the absolute phase difference is defined as $|\Delta\theta| = |\alpha - \pi|$. To derive the PBR, new notations are defined $r = I_{sam}/4I_{ref}$ and $g = I_{ref}/\langle I_{sam}\rangle$. For a pixel with specific phase α, its status is controlled by the intensity ratio of the reference and sample signal as derived from Eqs. 3.4.19 and 3.4.20,

$$\mathrm{DMD}(x, y) = \begin{cases} 1, & \cos|\Delta\theta| > \sqrt{r} \\ 0, & \text{else} \end{cases}. \tag{3.4.21}$$

As the absolute phase distribution of $\frac{\pi}{2} < \alpha < \frac{3\pi}{2}$ is uniform within $\left(0, \frac{\pi}{2}\right)$, given an intensity I_{sam}, the upper phase difference bound of "on" pixels is

$$\phi = \begin{cases} \arccos\left(\sqrt{r}\right) & r \leq 1 \\ 0, & \text{else} \end{cases}. \tag{3.4.22}$$

Since the sample intensity follows a Rayleigh distribution $I_{sam} :\ \mathrm{Rayleigh}(\sigma)$, the ratio r also follows a Rayleigh distribution with a scale parameter given by

$$\sigma_r = \sigma_{I_{sam}}/4I_{ref} = \frac{\sigma_{I_{sam}}}{4g\langle I_{sam}\rangle} = \frac{\sigma}{2\sqrt{2\pi}g\sigma} = \frac{1}{2\sqrt{2\pi}g}. \tag{3.4.23}$$

The peak intensity can then be derived from Eq. 3.4.12:

$$\begin{aligned}
\left\langle I_{peak} \right\rangle &\approx \frac{\pi}{2} N\left(N-1\right) A^2\sigma^2 \left\langle \left(\frac{\sin\phi}{\pi}\right)^2 \right\rangle \\
&= \frac{\pi}{2} N\left(N-1\right) A^2\sigma^2 \left(\int_0^1 \frac{1-r}{\pi^2} f(r)dr + \int_1^\infty \frac{0}{\pi^2} f(r)dr \right) \\
&= \frac{1}{2\pi} N\left(N-1\right) A^2\sigma^2 \int_0^1 (1-r)\frac{r}{\sigma_r^2} e^{-r^2/(2\sigma_r^2)} dr \\
&= \frac{1}{2\pi} N\left(N-1\right) A^2\sigma^2 \left[1 - \sqrt{\frac{\pi}{2}\sigma_r^2 \left(1 - e^{-1/\sigma_r^2}\right)} \right] \\
&= \frac{1}{2\pi} N\left(N-1\right) A^2\sigma^2 \left[1 - \sqrt{\frac{1-e^{-8\pi g^2}}{16 g^2}} \right].
\end{aligned} \tag{3.4.24}$$

In the same way, the background can be derived from Eq. 3.4.15:

$$\begin{aligned}
\left\langle I_{background} \right\rangle &= \frac{2NA^2\sigma^2}{\pi} \left\langle \phi \right\rangle \\
&= \frac{2NA^2\sigma^2}{\pi} \left(\int_0^1 \arccos\left(\sqrt{r}\right) f(r)dr + \int_1^\infty 0 f(r)dr \right) \\
&= \frac{2NA^2\sigma^2}{\pi} \int_0^1 \arccos\left(\sqrt{r}\right) \frac{r}{\sigma_r^2} e^{-r^2/(2\sigma_r^2)} dr \\
&= 16Ng^2 NA^2\sigma^2 \int_0^1 \arccos\left(\sqrt{r}\right) r e^{-4\pi g^2 r^2} dr.
\end{aligned} \tag{3.4.25}$$

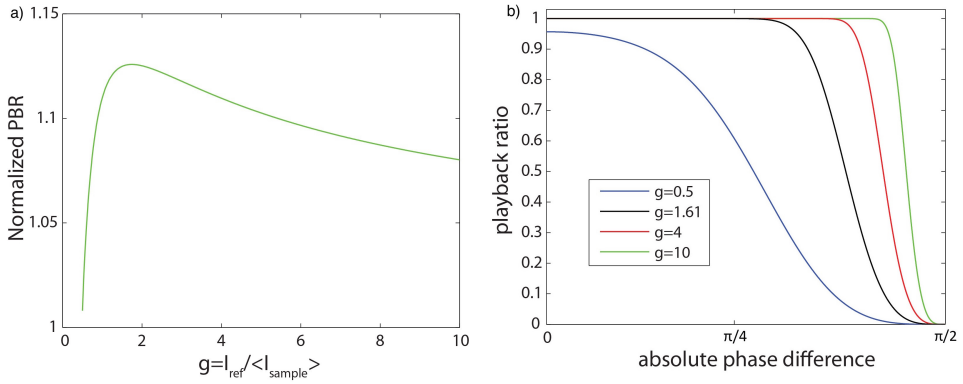

Figure 3.10: **Single shot binary phase retrieval**: (a) The normalized theoretical PBR (relative to $\mathrm{PBR}_{\mathrm{DMD},\phi\,=\,\pi/2}$) with respect to the intensity ratio g of the reference and sample beam. (b) The playback ratio function for different intensity ratios g.

So, calculating the PBR from these two quantities gives

$$\begin{aligned}
\mathrm{PBR}_{\mathrm{DMD},g=I_{ref}/\langle I_{sam}\rangle} &= \frac{\left\langle I_{peak}\right\rangle}{\left\langle I_{background}\right\rangle} \\
&= \frac{\frac{1}{2\pi}N\left(N-1\right)A^2\sigma^2\left[1-\sqrt{\frac{1-e^{-8\pi g^2}}{16g^2}}\right]}{16Ng^2NA^2\sigma^2\int_0^1 \arccos\left(\sqrt{r}\right)re^{-4\pi g^2r^2}dr} \\
&= \frac{\left(N-1\right)\left[1-\sqrt{\frac{1-e^{-8\pi g^2}}{16g^2}}\right]}{32\pi g^2\int_0^1 \arccos\left(\sqrt{r}\right)re^{-4\pi g^2r^2}dr} \\
&\approx \frac{N\left[1-\sqrt{\frac{1-e^{-8\pi g^2}}{16g^2}}\right]}{32\pi g^2\int_0^1 \arccos\left(\sqrt{r}\right)re^{-4\pi g^2r^2}dr},
\end{aligned} \tag{3.4.26}$$

which is a unimodal function of the intensity ratio g. For $\langle I_{sam}\rangle \ll I_{ref}$, $g \to \infty$ and the PBR is $\mathrm{PBR}_{\mathrm{DMD},\phi=\pi/2}$. As shown in Fig. 3.10(a), the function reaches its maximum at $g = 1.61$, having a value 12.6% higher than $\mathrm{PBR}_{\mathrm{DMD},\phi=\pi/2}$. This is consistent with Eq. 3.4.16, where the maximum value position is at $\phi = 0.371\pi$ equal to $\arccos\left(1/(2\sqrt{g})\right)$. The inherent statistical phase selection capacity of single-shot phase modulation allows us to achieve a PBR enhancement nearly equivalent to that offered by selecting the optimal bound ϕ from the exact phase map. According to Eq. 3.4.21, given a pixel with absolute phase difference $|\Delta\theta| < \pi/2$ and intensity I_{sam}, it will be turned on for playback when

$$\phi = \arccos\left(\sqrt{r}\right) = \arccos\left(\sqrt{I_{sam}/4I_{ref}}\right) > |\Delta\theta|\,. \tag{3.4.27}$$

For all pixels with an absolute phase difference $|\Delta\theta|$, as $r = I_{sam}/4I_{ref}$ follows a Rayleigh distribution, the fraction of pixels on will be

$$\begin{aligned}
p_{on}\left(|\Delta\theta|\right) &= \int_{|\Delta\theta|}^{\pi/2} f(\phi)d\phi \\
&= \int_0^{\cos^2|\Delta\theta|} \frac{r}{\sigma_r^2}e^{-r^2/(2\sigma_r^2)}dr \\
&= 1-e^{-4\pi g^2\cos^4|\Delta\theta|}.
\end{aligned} \tag{3.4.28}$$

The playback ratio function is plotted for different intensity ratios in Fig. 3.10(b).

References

[1] Ivo M Vellekoop and Allard P Mosk. “Focusing coherent light through opaque strongly scattering media”. In: *Optics Letters* 32.16 (2007), pp. 2309–2311.

[2] Allard P Mosk et al. “Controlling waves in space and time for imaging and focusing in complex media”. In: *Nature photonics* 6.5 (2012), pp. 283–292.

[3] Ivo M Vellekoop, Ad Lagendijk, and Allard P Mosk. “Exploiting disorder for perfect focusing”. In: *Nature Photonics* 4.5 (2010), pp. 320–322.

[4] Donald B Conkey, Antonio M Caravaca-Aguirre, and Rafael Piestun. “High-speed focusing of light through dynamic turbid media”. In: *Computational Optical Sensing and Imaging*. Optical Society of America. 2012, CTu4B–6.

[5] Hasan Yılmaz, Willem L Vos, and Allard P Mosk. “Optimal control of light propagation through multiple-scattering media in the presence of noise”. In: *Biomedical optics express* 4.9 (2013), pp. 1759–1768.

[6] SM Popoff et al. “Image transmission through an opaque material”. In: *arXiv preprint arXiv:1005.0532* (2010).

[7] Thomas Chaigne et al. “Controlling light in scattering media non-invasively using the photoacoustic transmission matrix”. In: *Nature Photonics* 8.1 (2014), pp. 58–64.

[8] Jonghee Yoon et al. “Measuring optical transmission matrices by wavefront shaping”. In: *Optics Express* 23.8 (2015), pp. 10158–10167.

[9] Zahid Yaqoob et al. “Optical phase conjugation for turbidity suppression in biological samples”. In: *Nature photonics* 2.2 (2008), pp. 110–115.

[10] Chia-Lung Hsieh et al. “Digital phase conjugation of second harmonic radiation emitted by nanoparticles in turbid media”. In: *Optics express* 18.12 (2010), pp. 12283–12290.

[11] Haowen Ruan et al. “Iterative time-reversed ultrasonically encoded light focusing in backscattering mode”. In: *Scientific reports* 4 (2014), p. 7156.

[12] Xiao Xu, Honglin Liu, and Lihong V Wang. “Time-reversed ultrasonically encoded optical focusing into scattering media”. In: *Nature photonics* 5.3 (2011), pp. 154–157.

[13] Ying Min Wang et al. “Deep-tissue focal fluorescence imaging with digitally time-reversed ultrasound-encoded light”. In: *Nature communications* 3 (2012), p. 928.

[14] Benjamin Judkewitz et al. “Speckle-scale focusing in the diffusive regime with time reversal of variance-encoded light (TROVE)”. In: *Nature photonics* 7.4 (2013), pp. 300–305.

[15] Edward Haojiang Zhou et al. “Focusing on moving targets through scattering samples”. In: *Optica* 1.4 (2014), pp. 227–232.

[16] Cheng Ma et al. “Time-reversed adapted-perturbation (TRAP) optical focusing onto dynamic objects inside scattering media”. In: *Nature photonics* 8.12 (2014), pp. 931–936.

[17] Puxiang Lai et al. “Time-reversed ultrasonically encoded optical focusing in biological tissue”. In: *Journal of Biomedical Optics* 17.3 (2012), pp. 0305061–0305063.

[18] Puxiang Lai et al. “Focused fluorescence excitation with time-reversed ultrasonically encoded light and imaging in thick scattering media”. In: *Laser Physics Letters* 10.7 (2013), pp. 075604–075609.

[19] Cheng Ma, Xiao Xu, and Lihong V Wang. “Analog time-reversed ultrasonically encoded light focusing inside scattering media with a 33,000× optical power gain”. In: *Scientific Reports* 5 (2015).

[20] Yan Liu et al. “Optical focusing deep inside dynamic scattering media with near-infrared time-reversed ultrasonically encoded (TRUE) light”. In: *Nature Communications* 6 (2015).

[21] B Jayet, J-P Huignard, and F Ramaz. “Optical phase conjugation in Nd: YVO 4 for acousto-optic detection in scattering media”. In: *Optics Letters* 38.8 (2013), pp. 1256–1258.

[22] Mooseok Jang et al. “Relation between speckle decorrelation and optical phase conjugation (OPC)-based turbidity suppression through dynamic scattering media: a study on in vivo mouse skin”. In: *Biomedical optics express* 6.1 (2015), pp. 72–85.

[23] Ichirou Yamaguchi and Tong Zhang. “Phase-shifting digital holography”. In: *Optics Letters* 22.16 (1997), pp. 1268–1270.

[24] Michael Liebling, Thierry Blu, and Michael Unser. “Complex-wave retrieval from a single off-axis hologram”. In: *Journal of the Optical Society of America A* 21.3 (2004), pp. 367–377.

[25] Duygu Akbulut et al. “Focusing light through random photonic media by binary amplitude modulation”. In: *Optics Express* 19.5 (2011), pp. 4017–4029.

[26] Ivo Micha Vellekoop. “Controlling the propagation of light in disordered scattering media”. In: *arXiv preprint arXiv:0807.1087* (2008).

[27] Dana Dudley, Walter M Duncan, and John Slaughter. “Emerging digital micromirror device (DMD) applications”. In: *Micromachining and Microfabrication*. International Society for Optics and Photonics. 2003, pp. 14–25.

[28] Giorgio Volpe, Giovanni Volpe, and Sylvain Gigan. “Brownian motion in a speckle light field: tunable anomalous diffusion and selective optical manipulation”. In: *Scientific Reports* 4 (2014).

[29] Joseph W Goodman. *Statistical Optics*. Vol. 1. Wiley-Interscience, 2000.

[30] Micha Nixon et al. “Real-time wavefront shaping through scattering media by all-optical feedback”. In: *Nature Photonics* 7.11 (2013), pp. 919–924.

Chapter 4

GLARE SUPPRESSION BY COHERENCE GATED NEGATION

This chapter is adapted from the manuscript Zhou, E.H., Shibukawa, A., Brake, J.& Yang, C. "Glare suppression by coherence gated negation". Optica 3, 1107 (2016). The contributions of authors are as follows: EHZ, JB and CY conceived the initial idea. EHZ developed the idea and experimental scheme. The experiments were designed and performed by EHZ and AS. The data analyses were performed by EHZ, AS, HR, JB and CY.

Imaging of a weak target hidden behind a scattering medium can be significantly confounded by glare. We report a method, termed coherence gated negation (CGN), that uses destructive optical interference to suppress glare and allow improved imaging of a weak target. As a demonstration, we show that by permuting through a set range of amplitude and phase values for a reference beam interfering with the optical field from the glare and target reflection, we can suppress glare by an order of magnitude, even when the optical wavefront is highly disordered. This strategy significantly departs from conventional coherence gating methods in that CGN actively 'gates out' the unwanted optical contributions while conventional methods 'gate in' the target optical signal. We further show that the CGN method can outperform conventional coherence gating image quality in certain scenarios by more effectively rejecting unwanted optical contributions.

4.1 Introduction

The ability to optically illuminate and image a target hidden behind a scattering medium is important in many applications, including transportation, remote sensing, biomedicine and astronomy. A classic example is the scenario of driving through fog at night with the automobile headlights on. The degradation of image quality in such scenarios can be generally ascribed to two effects: the optical wavefront distortion caused by the scattering medium and the glare from light backscattered from the scattering medium. The wavefront distortion limits our ability to perform diffraction-limited imaging and optical focusing. However, even in cases where the wavefront distortion does not prohibit imaging of the target, the sheer intensity of the glare can mask the weak optical reflection from a target and thereby prevent us from observing the target altogether.

Recent developments in wavefront shaping and adaptive optics have shown great promise in addressing the wavefront distortion challenge [1–6]. These methods have improved the imaging resolution beyond what was thought possible even a decade ago. However, in almost all of the demonstrations performed so far, the problem of glare is averted either by choosing a target that emits light at a different wavelength (fluorescence [4, 7, 8] or second harmonic generation [9, 10]) or by designing the experiments to operate in a transmission geometry [11, 12]. Glare remains a challenge largely unaddressed in the context of these developments. Unfortunately, glare is unavoidable in a variety of practical scenarios—driving in a foggy night is a good example. In that scenario, the objects you would like to observe are unlikely to be fluorescent, and you simply cannot rely on having an independent light source behind the objects to provide you with a transmission imaging geometry.

Glare suppression in principle is possible using time-of-flight methods with the help of fast imaging systems, such as those based on intensified charge-coupled device (ICCD) technology [13–15] or single photon avalanche diode (SPAD) arrays [16–18]. These devices are able to bin the light arriving at the detector with fine temporal resolution and therefore glare can be suppressed by discarding glare photons selected by their arrival time. Unfortunately, these instruments are very costly. But perhaps more importantly, the range to which they can suppress glare is determined by their response speed. The best commercial instruments available have a response time of 0.5 ns, which translates to a minimum length of 10 cm for which they can suppress glare by time gating. Recently, SPAD arrays with a temporal resolution of 67 ps have been demonstrated, which translates to a minimum glare suppression range of 1 cm. However, they are currently only available in small array sizes (32 x 32 pixels) [17, 19].

There have also been some interesting developments on the use of modulated illumination and post-detection processing in the phase or frequency domain to achieve time-of-flight based gating [20, 21]. One significant limitation to these methods is that they need to contend with glare associated noise, as the glare is not suppressed prior to detection. Moreover, such techniques are limited by the frequency bandwidth of the sensors, which leads to a minimum length involved on the order of meters. This length limitation for all known glare countering methods precludes useful applications of such time-of-flight methods in biomedicine where the length scale of interest ranges from microns to millimeters.

The streak camera is yet another fast response optical detection system. Its response

speed is on the order of one picosecond. Unfortunately, the streak camera is intrinsically a one-dimensional imaging system. Recently, it has been demonstrated that the use of compressed sensing can allow the streak camera to perform fast two-dimensional imaging with a spatial resolution of 11 mm [22–24]. However, the object sparsity constraint is too restrictive for the majority of glare suppression applications.

Here we report a method, termed coherence gated negation (CGN), that is capable of coherently suppressing glare through the use of destructive interference to allow improved imaging of a weak target. This method can operate over a length scale span that is limited only by the coherence length of available optical sources, which can range from microns (for superluminescent diodes) to kilometers (for fiber lasers). CGN shares its roots with acoustic noise cancellation [25]. The basic idea is to use a reference optical field of the same magnitude and opposite phase to destructively interfere with the glare component of a returning optical field to null out the glare and its associated noise, thereby allowing the electronic detector to measure only the optical signal from the hidden target. In the case of acoustic noise cancellation, the amplitude and phase of the unwanted signal can be separately measured and used as input in the cancellation process. In CGN, we do not have this luxury as we do not have prior knowledge of the glare optical field characteristics. Here, we instead employ a light source of suitable coherence length such that a) the glare optical field is coherent with the reference optical field, and b) the target reflection is incoherent. By permuting through a specific set of amplitude and phase values for the reference field, we ensure that the condition for effective destructive interference is met within a certain error bound for one of the permutations. By screening for the minimum detected optical signal through the whole set, we can then determine the signal reflected from the target. When performed in an imaging context, this allows us to use a single permutation set operating over all the camera pixels at once to generate a glare suppressed image even if the optical field is highly disordered and speckled.

Using this approach, we experimentally demonstrate the ability to suppress the glare intensity by a factor of 10 times with the use of a permutation set of size 256. Our experimental design choice also allowed us to demonstrate glare suppression on the length scale of 2 mm—a regime that conventional time-of-flight methods are presently unable to reach. Finally, we discuss the advantages and tradeoffs of CGN versus traditional coherence gating methods and report our experiments

demonstrating CGN's ability to image targets at different depths without system alterations, and several scenarios where CGN can provide better target image quality than conventional coherence gating methods.

4.2 Principle

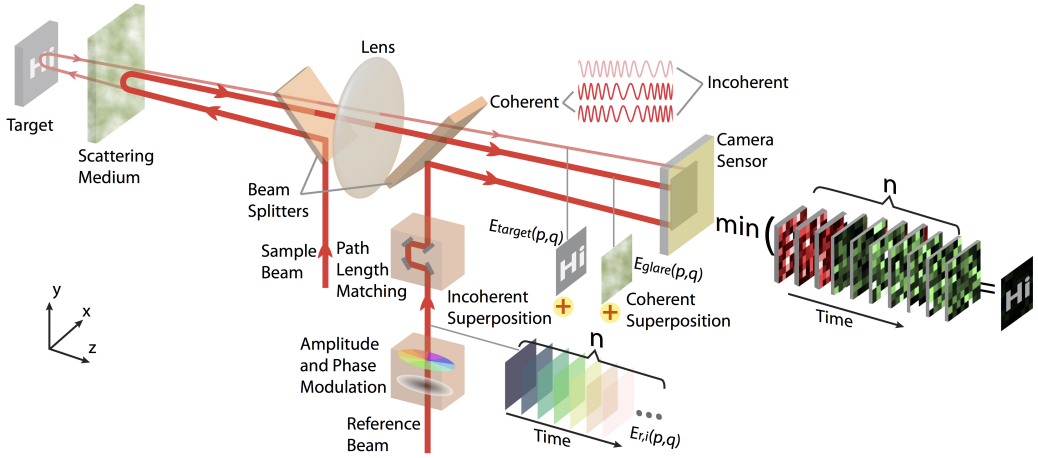

Figure 4.1: **Principle of the CGN technique**: The CGN system uses a laser as the illumination source for the active imaging system. With the presence of a scattering medium, a significant portion of the light is backscattered to the camera that images the target. A plane-wave reference beam, with path length and polarization matched to the backscattered light (glare), is used to cancel the glare by destructive interference. In this case, we step both the amplitude and phase of the reference beam to cover a significant dynamic range of the glare and combine each of them with the glare respectively, resulting in a set of speckle images from the camera. By taking the minimum intensity of each pixel vector along the time axis of the speckle image set, we can reconstruct the image of the target with significant glare suppression.

A concise setup to explain the principle of CGN is shown diagrammatically in Fig. 4.1. A laser beam illuminates a two-dimensional target located behind a scattering sample. The returning light, which consists of light that is back-scattered by the scattering medium as well as light reflected from the target, is captured by the imaging system, resulting in an image of the target obscured by glare. On the camera sensor chip, the captured optical field is the superposition of the glare $E_{glare}(p,q)$ and the target reflection $E_{target}(p,q)$, where p and q are the pixel numbers in the x and y directions, respectively. To realize CGN, a collimated reference beam $E_{r,i}(p,q)$ is added on the camera by a beam splitter to interfere with $E_{glare}(p,q)$ and $E_{target}(p,q)$. We perform path length matching of the glare contribution and the reference beam. By choosing the coherence length of the laser source appropriately,

we can make sure the glare contributions from the extended scattering medium are in coherence with the reference beam. As long as the optical path length of the target reflection is substantially different from the majority of the optical path lengths of the glare components, the target reflection will not be in coherence with the reference beam. We then permute the reference beam through a series of phase and amplitude values. The observed image intensity for the ith image can be expressed as

$$I_i(p,q) = I_{target}(p,q) + |E_{glare}(p,q) + E_{r,i}(p,q)|^2, \tag{4.2.1}$$

where $I_{target}(p,q) = |E_{target}|^2$ is the target intensity.

We further assume that the imaging is performed in such a way that the image speckle size is greater than the camera pixel size. This ensures that there are no phase variations across the surface of any given pixel. In this case, the minimum value that $I_i(p,q)$ can take is $I_{target}(p,q)$, which occurs when $E_{r,i}(p,q)$ is of the same magnitude and opposite phase of $E_{glare}(p,q)$ (destructive interference), that is $|E_{glare}(p,q) + E_{r,i}(p,q)|^2 = 0$. As such, by permuting through different phase and amplitude values for $E_{r,i}(p,q)$, we can determine $I_{target}(p,q)$ for each image pixel simply by taking the smallest measured $I_i(p,q)$ through a set of reference field permuted images. As the glare cancellation is performed in the optical regime, CGN can allow detection of the target without any noise consideration from the glare at all.

In practice, we do not expect complete destructive interference to occur as the glare optical field's phase and amplitude are continuously distributed, while the modulation of the reference phase and amplitude can only be performed in a discrete fashion. The greater the permutation set, the more effectively we can suppress the glare at the price of longer data collection time.

4.3 Methods

Sample Preparation

Polystyrene microspheres with a mean diameter of 3 μm (Polybead Microsphere, Polysciences, Inc.) were mixed with a 1.5% carrageenan gel in aqueous phase. The mixture was cast in a mold of size 15 mm × 25 mm, with a thickness of 1 mm or 0.5 mm. The medium had a scattering coefficient of $\mu_s = \sigma_s \times N = 1.3$ mm^{-1} and a reduced scattering coefficient of $\mu_s' = 0.2925 mm^{-1}$ as calculated via Mie scattering theory, where the density of the microspheres N was 6.8×10^7 ml^{-1} and the scattering cross section σ_s was 18.7 μm^2. The ballistic transmission of the sample was measured to be 23%, which agrees with the theoretically predicted

value. The target was made by attaching a positive mask showing letters “Hi” to an optical mirror. The height of the letter ‘H’ was 1 mm.

Setup

The experiment was carried out on a custom-built setup as depicted in Fig.4.2(a). A continuous-wave laser (MGL-FN-532, Opto Engine) with a wavelength of 532 nm and a coherence length of 1mm (see Supplement for detailed measurement) was used as the light source to illuminate the target. A laser with a long coherence length (Excelsior 532, Spectra Physics, 532 nm wavelength, >9 m coherence length) was used only for characterizing the glare (Fig. 4.3). Light from the laser was split into a reference beam and a sample beam by a beam splitter (CBS). The sample beam illuminated the target at 2 mm behind the scattering sample (SS) (shown in Fig. 4.2(a)). Light reflected from the target and the glare propagating through a beam splitter (BS1) was captured by an objective lens (OBJ, M Plan Apo 2×, NA=0.055, Mitutoyo), linearly polarized, and imaged by a tube lens (L1) on to the camera (Resolution: 1936 (H) × 1456 (V), Pixel size: 4.54 µm x 4.54 µm, Prosilica GX 1920, Allied Vision). The optical field’s effective angular range was 6.3 degrees. This translates to an optical speckle spot size of 19.2 µm on average at the sensor (pixel size 4.4 µm). The reference beam was modulated by an amplitude modulator (EO-AM-NR-C4, Thorlabs) and a phase modulator (EO-PM-NR-04, Thorlabs) through permutations of 8 amplitude steps and 32 phase steps successively. The polarization direction of the reference beam was aligned with the sample beam. The reference beam was spatially filtered, collimated into a plane wave, and coupled to the camera in normal direction using a beam splitter (BS2). The path length of the reference beam matched with that of the light reflected from the scattering sample.

4.4 Experiments and Results

Experimental Demonstration of Glare Suppression with CGN

To validate the CGN method, we implemented the experimental setup shown in Fig. 4.2(a). A continuous-wave laser (MGL-FN-532, Opto Engine, 532 nm wavelength, 1mm coherence length) was used as the light source. Light from the laser was split into a reference and sample beam by a beam splitter (CBS). The sample beam illuminated the target, which was placed 2 mm behind the scattering sample (SS) (shown in Fig. 4.2(a)). The scattering sample (15 mm (x) × 25 mm (y) × 1 mm (z)) consisted of polystyrene particles (3 µm in diameter) in a gel phantom (concen-

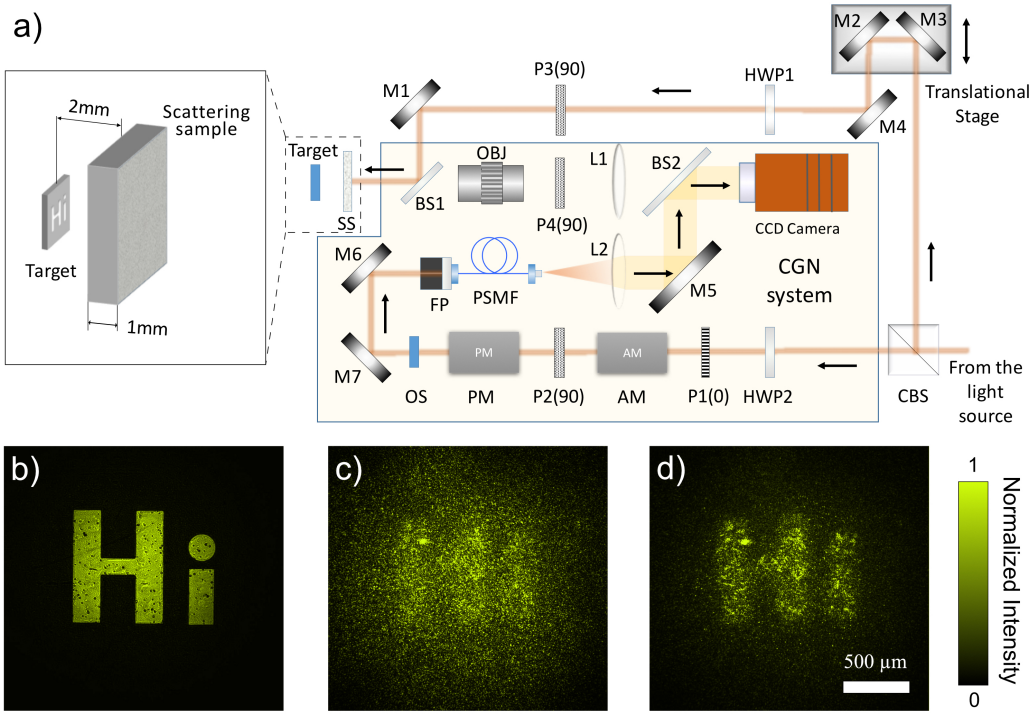

Figure 4.2: **Experimental demonstration of CGN**: (a) Experimental setup. AM, amplitude modulator; BS, beam splitter; CBS, cubic beam splitter; FP, fiber port; HWP, half-wave plate; L, lens; M, mirror; OBJ, objective lens; OS, optical shutter; P, polarizer; PM, phase modulator; PSMF, polarization-maintaining single mode fiber. (b) Image of the target without glare. (c) Image of the target with glare before CGN. (d) Image of the target after CGN.

tration 6.8×10^7 ml^{-1}, see Methods, Sample preparation). The back-reflected light consisted of reflections from the target and glare from the scattering sample. On the other optical path, the reference beam was passed through an amplitude and phase modulator, spatially filtered, and collimated into a plane wave. The collimated reference beam illuminated the camera sensor chip at normal incidence. The reflected light from the target and the glare propagating through BS1 was captured by an objective lens (OBJ), filtered to a single polarization, and imaged by a tube lens (L1) onto the camera. The optical field's effective angular range was 6.3 degrees. This translates to an optical speckle spot size of 19.2 µm at the sensor. In comparison, the camera pixel size is 4.4 µm. This allowed us to enforce the CGN operating requirement that the phase not vary substantially across any given pixel's surface. By path length matching, the collimated reference beam only interfered with the glare but not the reflection from the target. Before CGN was applied, an optical shutter (OS) blocked the reference beam, and an image of the target occluded by

glare was captured as shown in Fig. 4.2(c). The optical shutter was then opened and CGN applied. The reference beam was modulated through all permutations of 8 amplitude values and 32 phase values successively. The 8 amplitude values were chosen to be $\frac{n}{8}A$, respectively, where n = 1 to 8 and A is the 99th percentile value of the glare amplitude. For the phase, the 32 values simply divide 0 to 2π radians equally. After the reference beam went through all the permutations, a glare suppressed CGN image was acquired (Fig. 4.2(d), Media 2). Comparing the image before CGN (Fig. 4.2(c)) and after CGN (Fig. 4.2(d)), we can clearly discern the previously obscured target. To quantify the glare suppression ability of the CGN technique, we define the glare suppression factor as the ratio between the mean intensity of the glare before and after the CGN process. Through a null target experiment, we determined that the glare suppression factor was 10 for this experiment. Unsurprisingly, the glare wavefront was highly disordered. The glare wavefront as determined by the CGN process is reported in the appendix.

As discussed earlier, the glare suppression factor is directly determined by the size of the permuted set of reference amplitude and phase values. We next performed an experiment to measure the glare suppression factor with different numbers of steps in the reference field phase and amplitude. To eliminate the influences of laser coherence for residual glare intensity, a laser with a long coherence length (Excelsior 532, Spectra Physics, 532 nm wavelength, >9 m coherence length) was used in this experiment.

A series of glare suppression factors were measured through CGN experiments with a null target but the same scattering medium (15 mm (x) × 25 mm (y) × 1 mm (z)) consisting of polystyrene particles (3 μm in diameter) in a carrageenan gel phantom (concentration 6.8×10^7 ml^{-1}, see Methods, Sample preparation). Following the aforementioned strategy, we varied the number of amplitude steps from 1 to 10 and the number of phase steps from 1 to 32. The full chart is shown in the appendix. The plots of selected combinations are included in Fig. 4.3(a). For comparison, the expected CGN factor computed through an idealized simulation are shown as well (see appendix for details). The mismatch between the measured and ideal CGN factor can be attributed to: a) phase jitter in the reference beam and sample beam due to vibration in the system, b) noise in the electronics including the laser and electro-optical modulator, and c) limited extinction ratio of the amplitude modulator and polarized optics, etc. Fig. 4.3(b) shows a histogram of the glare intensity before and after CGN for the situation where we permute through 10 amplitude steps and

32 phase steps. In this case, we experimentally achieved a glare suppression factor of ~30.

Comparison to Coherence Gating

By only detecting the optical field component that is coherent with the reference field, conventional coherence gating methods can also reject glare. However, the way in which conventional coherence gated (CG) and coherence gated negation (CGN) imaging methods work are opposite in nature. While CG imaging methods are good at 'gating in' an optical field originating from a specific chosen distance, CGN is good at 'gating out' the glare optical field. These different approaches to imaging in the presence of scattering and glare lead to two key distinctions between conventional CG methods and the CGN approach [26–28].

The first key distinction between CG and CGN is that CG methods reject glare contributions as well as any other potential optical signals of interest outside the coherence window. In comparison, CGN can permit detection of all optical signals that do not share the same coherence window as the glare components. This distinction is practically important. In a scenario where there are two objects at different distances behind a fog, a CG method, such as coherent Light Detection And Ranging (LiDAR), is only able to detect one object at a given time. Another class of CG methods, based on spectral sweeping, such as swept source optical coherence tomography [27], can perform simultaneous depth-ranging of multiple objects. However, such methods are intrinsically limited in their range span. Moreover, if the objects' distances are unknown, the coherent LiDAR system would have to be exhaustively range-scanned to find the objects. In comparison, by working to suppress glare, CGN permits direct observation of all objects at any range beyond the glare suppression region. However, this advantage does come with a compensating disadvantage - CGN is not capable of providing depth information of the objects.

To demonstrate CGN's advantage over CG in this aspect, we performed the following experiment. As shown in Fig. 4.4(a), following the aforementioned procedure, CGN was applied to the target located at different positions A, B, and C, which correspond to 1 mm, 2 mm, and 3 mm behind the scattering sample, respectively. Since CGN works by coherently gating out the glare component of the light, no adjustment is required to adapt to the depth change of the target, as long as the target remains within the depth of field of the imaging system. The experimental results are displayed in Fig. 4.4(b)-(g). Fig. 4.4(b)-(d) are images of the target captured before

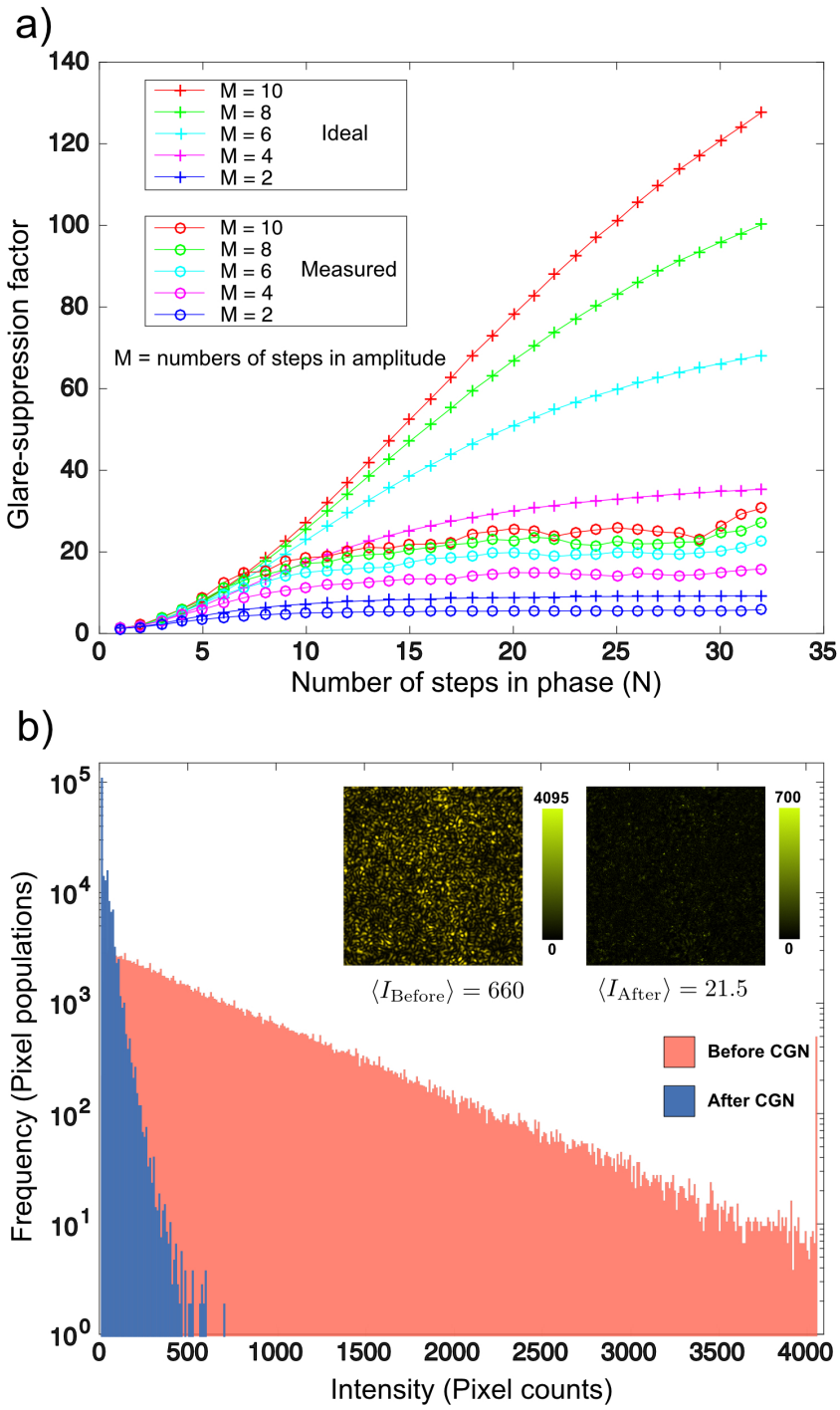

Figure 4.3: **Characterization of glare suppression factor**: (a) Comparison of glare suppression factor between measurement and simulation results with various phase and amplitude steps. (b) Histogram of pixel intensities before and after glare suppression, with intensity maps of the glare shown in the insets.

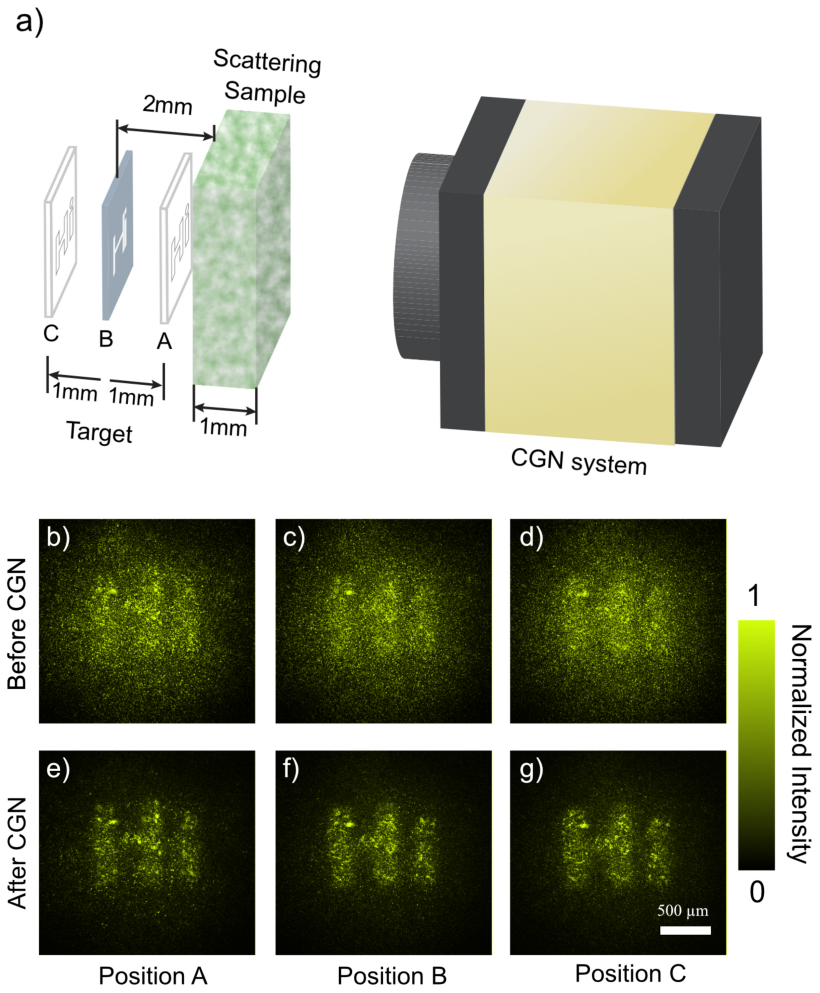

Figure 4.4: **Reconstruction of the target at different distances**: (a) Illustration of the target positions. (b-d) Before CGN, images of the target at position A, B, and C, respectively. (e-g) After CGN, images of the target at position A, B, C, respectively.

glare suppression, while Fig. 4.4(e)-(g) are images captured after glare suppression. From their comparison, we can easily discern that glare is suppressed and the visibility of the target is enhanced.

The second key distinction between CG and CGN is that if an element contributing glare and a weak target object both lie within the coherence envelope of the light source, CGN can actually provide a superior signal-to-background image of the object. To clearly and simply explain this point, we consider a scattering sample as the glare contributor and a weak target placed at a distance L away from the CGN system (as shown in Fig. 4.5(b). Here the coherence length of the light source is C, and L is set to be shorter than C (L<C). Under CGN operation, we adjust the path

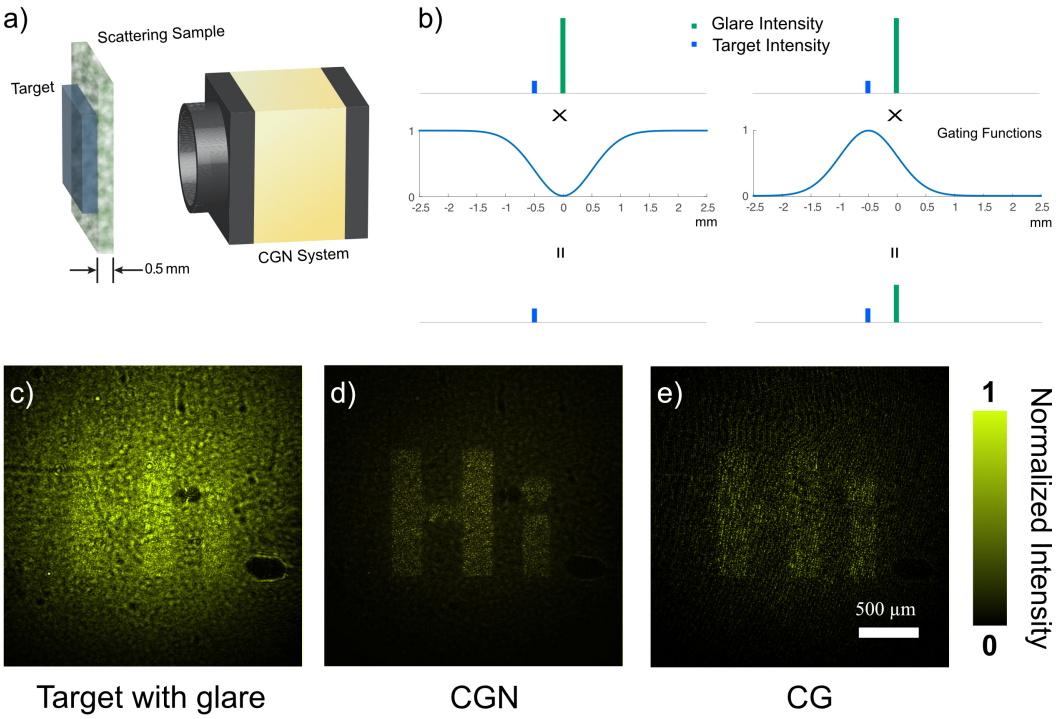

Figure 4.5: **Comparison of CGN and CG techniques**: (a) Illustration of the experimental configuration. (b) Cartoon diagrams that schematically illustrate the difference between CGN and CG techniques when both the target and scattering medium are within the coherence gating window. The CGN technique uses an inverted coherence gating function to gate out the glare significantly, with less suppression of the target, resulting in higher target intensity than glare. The CG technique gates in the target intensity with less preservation of glare. However, the residue of the glare remains higher than the target intensity because of the strong nature of the glare. (c) Original image of the target with glare. (d) Reconstructed image of the target with the CGN technique. (e) Reconstructed image of the target with the CG technique.

length to match the reference beam with the glare contribution. CGN will completely suppress the glare in this situation. As the target is partially coherent, we would expect a diminished signal associated with the target as only the incoherent portion of the target will contribute to image formation. In contrast, under conventional CG operation, we would match the reference beam path length to the target. This results in the detection of the target as well as a partial contribution from the coherent component of the glare. In aggregate, the CGN detection scheme results in a depressed target signal with no glare background, which is more desirable than the CG case where a glare background is present. This result is also valid over the range of an extended scattering media. To demonstrate CGN's advantage, we performed

the following experiment. As shown in Fig. 4.5(a), a thin scattering medium (15 mm (x) × 25 mm (y) × 0.5 mm (z)) consisting of polystyrene particles (3 μm in diameter) in a gel phantom (concentration 6.8×10^7 ml^{-1}, see Methods, Sample Preparation) was attached directly on the top of a reflective target. CGN was applied after the path length of the reference beam was matched with the glare as shown in Fig. 4.5(b). Images of the target acquired before and after CGN are included in Fig. 4.5(c) and Fig. 4.5(d), respectively. After these images were acquired, the path length of the reference beam was adjusted to match the reflection from the target and phase shifting holography [29] was applied as a demonstration of a CG approach. The retrieved intensity map from this procedure is shown in Fig. 4.5(e).

4.5 Discussion

In this series of experiments, we demonstrated the differences and advantages of CGN compared to hardware based time-of-flight glare reduction systems and conventional coherence gating methods. CGN's ability to suppress glare over optical distances as short as several microns through the use of low coherence light sources, such as superluminescent diodes, contrasts favorably compared to conventional time-of-flight hardware. We also showed that, by suppressing glare and permitting all other optical signals to pass, CGN allows for the simultaneous imaging of objects at different distances. In contrast, CG methods are good at imaging objects at a given distance and rejecting optical contributions before and after the chosen plane. We further showed that CGN can outperform CG methods in image quality under certain conditions—specifically, when the glare components and the target optical field are within the same coherence window of the interferometer.

At the current time, the CGN method can only be used to assist the imaging of amplitude objects. While we do not see a straightforward way to extend CGN to enable phase imaging, we do not preclude the possibility of such developments in the future.

The CGN design for a specific application will be application dependent. For example, in the scenario where we would like to cancel glare from a fast changing scattering medium, we would likely need both a fast camera and a fast reference field permutation apparatus. One solution may be to directly measure the amplitude and phase of the glare wavefront using holography and then play back the appropriate field to negate the glare in a single step without iteration. However, this method will still be relatively slow since it needs a camera. Furthermore, it would likely be very

challenging to implement since it is requires the ability to simultaneously control both the amplitude and phase of the wavefront across the full-frame. In order to achieve a faster implementation, we may instead choose to perform CGN on a pixel-by-pixel basis rather than a full-frame basis. For pixel-by-pixel CGN, we would focus on a single pixel and iteratively derive the correct reference cancellation field quickly using a fast single pixel detector such as a photodiode. In an ideal situation, we would only need a few measurements to arrive at the correct field [30, 31]. By performing CGN this way, we can progressively work through all the image pixels. As long as the time taken to optimize glare suppression for each pixel is shorter than the time scale at which the scattering medium is decorrelating its optical field, we can expect to suppress glare effectively.

Appendix

Characterization of the Glare Field

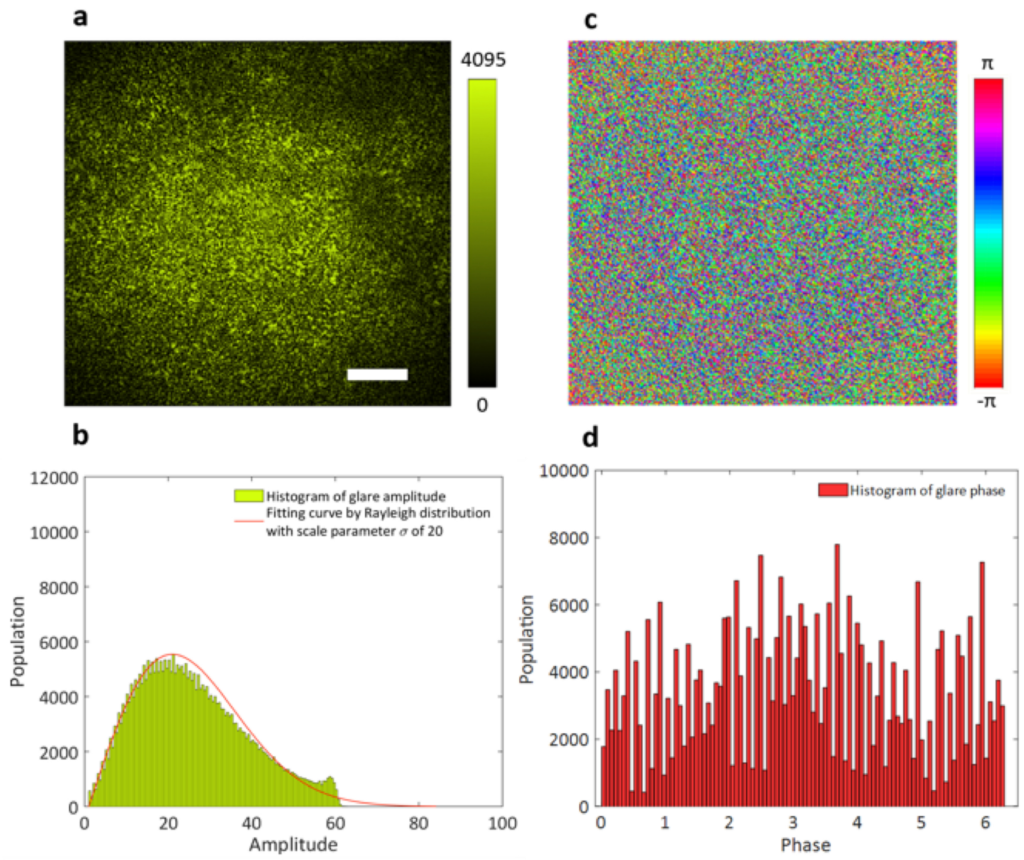

Figure 4.6: **Characterization of glare back-reflected from a scattering medium**: (a) Intensity of the glare. The glare appears as a random speckle field. (b) Histogram of the amplitude of the glare. The amplitude of the speckle typically follows a Rayleigh distribution with probability density function $p(A) = \frac{A}{\sigma^2} e^{-\frac{A^2}{2\sigma^2}}$, where A is the amplitude and σ is the mode of the Rayleigh distribution. Fitting the data with a Rayleigh distribution ($\sigma = 20$) shows good agreement with the histogram of the measured amplitude. (c) Phase map of the glare. (d) Histogram of the phase of the glare. The phase is uniformly distributed over 0 to 2π. Scale bar is 500 μm.

Simulated and Experimental CGN Factor

To simulate glare, a speckle field of 10^6 grains is generated, which follows a Rayleigh distribution in amplitude and a uniform distribution in phase. We also generate multiple sets of reference fields consisting of different numbers of steps in amplitude and phase. The number of reference fields for a single set, whose number of steps in amplitude and phase are M and N, respectively, is $M \times N$. By screening for the

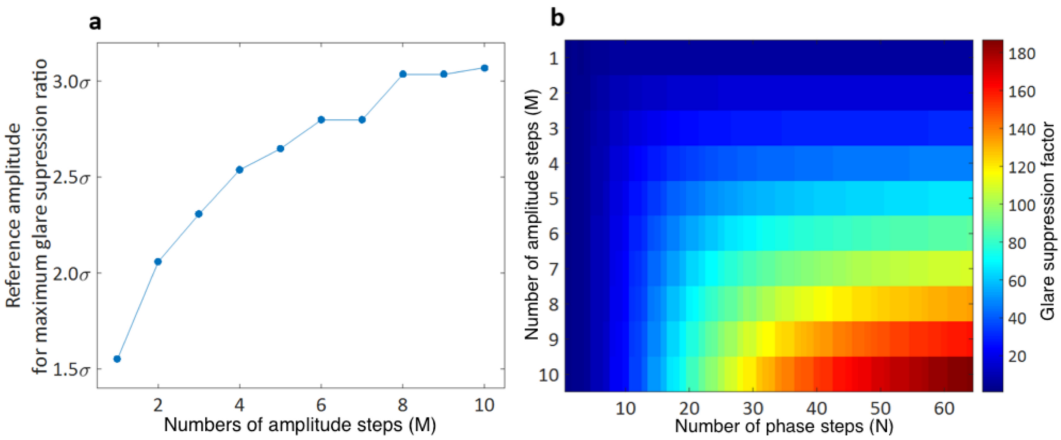

Figure 4.7: Ideal glare suppression factor in different conditions computed via simulation.

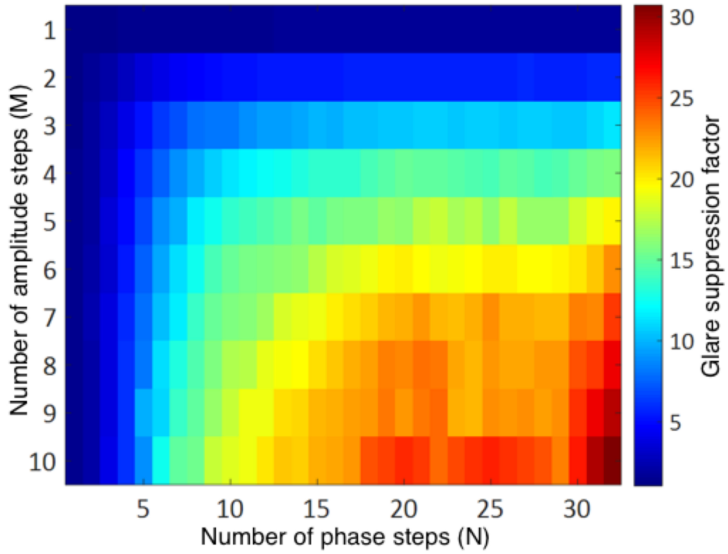

Figure 4.8: Measured glare suppression factor in different conditions.

minimum value of destructive interference between the speckle field and the whole set of reference fields, the residue of glare of the speckle field is determined as the glare after CGN is applied. The glare suppression factor is calculated from the ratio of the glare intensity before and after CGN. Fig. 4.7(a) is a plot of the optimum reference amplitude versus the number of amplitude steps. If the reference amplitude is set to the maximum glare amplitude, the glare suppression factor will be extremely low. Due to the Rayleigh distributed amplitude, the majority of the glare amplitude values are much lower than its maximum, as shown in Fig. 4.6(b). To efficiently suppress the glare, the reference maximum amplitude must be chosen properly.

This plot can be used as a reference. Fig. 4.7(b) is a 2D plot of glare suppression factor versus the number of steps in the reference amplitude and phase. When the number of steps in amplitude and phase are 10 and 32 respectively, the ideal glare suppression factor is around 130. As a comparison, a series of glare suppression factors were measured. The experimental results are included in Fig. 4.8. From the plot, we can tell when the number of steps in the amplitude and phase are 10 and 32, respectively, the measured glare suppression factor is around 30. The mismatch between measured and ideal glare suppression factor can be attributed to a) phase jitter in the reference beam and the sample beam due to vibration in the system, b) noise in the electronics including the laser and electro-optical modulator, and c) limited extinction ratio of the amplitude modulator, polarized optics, etc.

Light Source Coherence Characterization

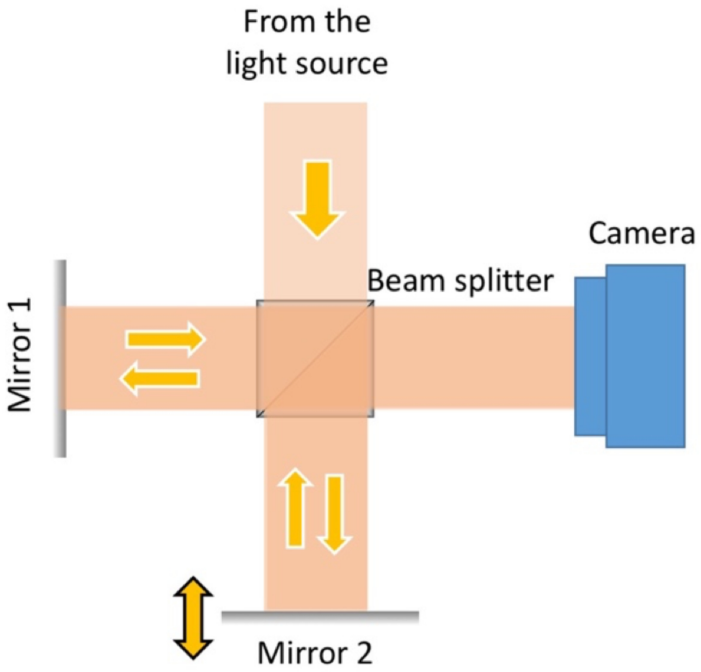

Figure 4.9: Schematic setup of Michelson interferometer for characterizing the coherence properties of the light source.

To characterize the coherence of the light source, a Michelson interferometer was built as shown in Fig. 4.9. Collimated light from the laser was split into two arms by a beam splitter. Each of those was reflected back toward the beamsplitter which then combined their amplitudes interferometrically. The resulting interference pattern was captured by a camera (Prosilica GX 1920, Allied Vision). The two plane

waves intersected with an angle, and therefore parallel fringes can be observed on the camera. The contrast ratio of the fringes represents the coherence of the light source,

$$V = \frac{I_{max} - I_{min}}{I_{max} + I_{min}}, \tag{4.5.1}$$

where I_{max} is the maximum intensity of the bright fringes and I_{min} is the minimum value of the dark fringes. Mirror 2 was mounted on a piezo stage (AG-LS25, Newport). The stage traveled a distance of 5 mm. A series of interference patterns were captured at different positions, from which their corresponding contrasts were calculated. A plot of the contrasts versus the position were included in Fig. S5. From the plot, we can tell its full width half maximum (FWHM), which is equivalent to the coherence length, is 1.03 mm.

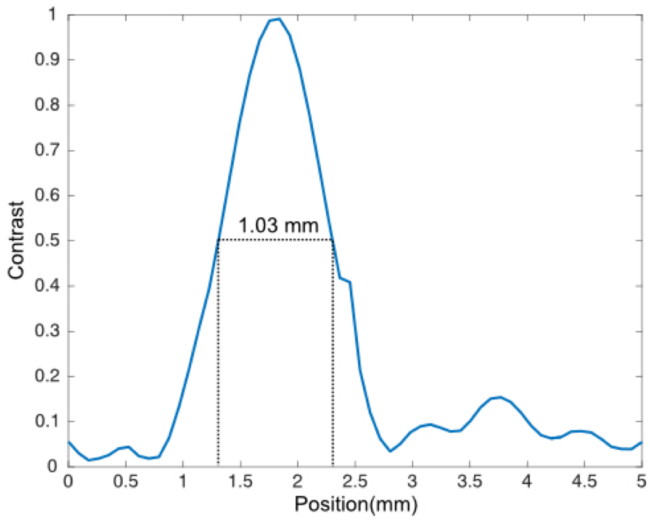

Figure 4.10: Plot of fringe contrast versus mirror position.

References

[1] Allard P Mosk et al. “Controlling waves in space and time for imaging and focusing in complex media”. In: *Nature photonics* 6.5 (2012), pp. 283–292.

[2] Roarke Horstmeyer, Haowen Ruan, and Changhuei Yang. “Guidestar-assisted wavefront-shaping methods for focusing light into biological tissue”. In: *Nature photonics* 9.9 (2015), pp. 563–571.

[3] Zahid Yaqoob et al. “Optical phase conjugation for turbidity suppression in biological samples”. In: *Nature photonics* 2.2 (2008), pp. 110–115.

[4] Jacopo Bertolotti et al. “Non-invasive imaging through opaque scattering layers”. In: *Nature* 491.7423 (2012), pp. 232–234.

[5] Ori Katz, Eran Small, and Yaron Silberberg. “Looking around corners and through thin turbid layers in real time with scattered incoherent light”. In: *Nature photonics* 6.8 (2012), pp. 549–553.

[6] Na Ji, Daniel E Milkie, and Eric Betzig. “Adaptive optics via pupil segmentation for high-resolution imaging in biological tissues”. In: *Nature methods* 7.2 (2010), pp. 141–147.

[7] Ying Min Wang et al. “Deep-tissue focal fluorescence imaging with digitally time-reversed ultrasound-encoded light”. In: *Nature communications* 3 (2012), p. 928.

[8] Edward Haojiang Zhou et al. “Focusing on moving targets through scattering samples”. In: *Optica* 1.4 (2014), pp. 227–232.

[9] Xin Yang, Ye Pu, and Demetri Psaltis. “Imaging blood cells through scattering biological tissue using speckle scanning microscopy”. In: *Optics express* 22.3 (2014), pp. 3405–3413.

[10] Chia-Lung Hsieh et al. “Digital phase conjugation of second harmonic radiation emitted by nanoparticles in turbid media”. In: *Optics express* 18.12 (2010), pp. 12283–12290.

[11] Ori Katz et al. “Non-invasive single-shot imaging through scattering layers and around corners via speckle correlations”. In: *Nature photonics* 8.10 (2014), pp. 784–790.

[12] Eitan Edrei and Giuliano Scarcelli. “Optical imaging through dynamic turbid media using the Fourier-domain shower-curtain effect”. In: *Optica* 3.1 (2016), pp. 71–74.

[13] Martin Laurenzis et al. “3D range-gated imaging in scattering environments”. In: *SPIE Defense, Security, and Sensing*. International Society for Optics and Photonics. 2010, pp. 768406–768406.

[14] Martin Laurenzis et al. “Investigation of range-gated imaging in scattering environments”. In: *Optical Engineering* 51.6 (2012), pp. 061303–1.

[15] Martin Laurenzis and Emmanuel Bacher. “Image coding for three-dimensional range-gated imaging”. In: *Applied optics* 50.21 (2011), pp. 3824–3828.

[16] Mauro Buttafava et al. “Non-line-of-sight imaging using a time-gated single photon avalanche diode”. In: *Optics express* 23.16 (2015), pp. 20997–21011.

[17] Genevieve Gariepy et al. “Single-photon sensitive light-in-fight imaging”. In: *Nature communications* 6 (2015).

[18] Fabrizio Guerrieri et al. “Two-dimensional SPAD imaging camera for photon counting”. In: *IEEE Photonics Journal* 2.5 (2010), pp. 759–774.

[19] Genevieve Gariepy et al. “Detection and tracking of moving objects hidden from view”. In: *Nature Photonics* (2015).

[20] Andreas Velten et al. “Recovering three-dimensional shape around a corner using ultrafast time-of-flight imaging”. In: *Nature communications* 3 (2012), p. 745.

[21] Achuta Kadambi et al. “Frequency domain ToF: encoding object depth in modulation frequency”. In: *arXiv preprint arXiv:1503.01804* (2015).

[22] Liang Gao et al. “Single-shot compressed ultrafast photography at one hundred billion frames per second”. In: *Nature* 516.7529 (2014), pp. 74–77.

[23] Liren Zhu et al. “Space-and intensity-constrained reconstruction for compressed ultrafast photography”. In: *Optica* 3.7 (2016), pp. 694–697.

[24] Jinyang Liang et al. “Encrypted Three-dimensional Dynamic Imaging using Snapshot Time-of-flight Compressed Ultrafast Photography.” In: *Scientific reports* 5 (2014), pp. 15504–15504.

[25] RR Leitch and MO Tokhi. “Active noise control systems”. In: *IEE Proceedings A (Physical Science, Measurement and Instrumentation, Management and Education, Reviews)* 134.6 (1987), pp. 525–546.

[26] David Huang et al. “Optical coherence tomography”. In: *Science (New York, NY)* 254.5035 (1991), p. 1178.

[27] Ireneusz Grulkowski et al. “High-precision, high-accuracy ultralong-range swept-source optical coherence tomography using vertical cavity surface emitting laser light source”. In: *Optics letters* 38.5 (2013), pp. 673–675.

[28] Sungsoo Woo et al. “Depth-selective imaging of macroscopic objects hidden behind a scattering layer using low-coherence and wide-field interferometry”. In: *Optics Communications* 372 (2016), pp. 210–214.

[29] Ichirou Yamaguchi and Tong Zhang. “Phase-shifting digital holography”. In: *Optics Letters* 22.16 (1997), pp. 1268–1270.

[30] Song Zhang, Daniel Van Der Weide, and James Oliver. “Superfast phase-shifting method for 3-D shape measurement”. In: *Optics express* 18.9 (2010), pp. 9684–9689.

[31] Peisen S Huang and Song Zhang. “Fast three-step phase-shifting algorithm”. In: *Applied optics* 45.21 (2006), pp. 5086–5091.

Chapter 5

IMAGING MOVING TARGETS THROUGH SCATTERING MEDIA

This chapter is adapted from the manuscript Cua, M., Zhou, E.H. & Yang, C. "Imaging moving targets through scattering media". Optics Express 25, 3935 (2017). The contributions of authors are as follows: EHZ and CY conceived the initial idea. MC and EHZ developed the idea and scheme demonstration. The experiments were designed and performed by MC and EHZ. The data analyses were performed by MC and EHZ.

Optical microscopy in complex, inhomogeneous media is challenging due to the presence of multiply scattered light that limits the depths at which diffraction-limited resolution can be achieved. One way to circumvent the degradation in resolution is to use speckle- correlation-based imaging (SCI) techniques, which permit imaging of objects inside scattering media at diffraction-limited resolution. However, SCI methods are currently limited to imaging sparsely tagged objects in a dark-field scenario. In this work, we demonstrate the ability to image hidden, moving objects in a bright-field scenario. By using a deterministic phase modulator to generate a spatially incoherent light source, the background contribution can be kept constant between acquisitions and subtracted out. In this way, the signal arising from the object can be isolated, and the object can be reconstructed with high fidelity. With the ability to effectively isolate the object signal, our work is not limited to imaging bright objects in the dark-field case, but also works in bright-field scenarios, with non-emitting objects.

5.1 Introduction

Optical imaging is challenging in turbid media, where multiple scattering of light causes a degradation of resolution and limits the depths at which we can reliably image ($<$ 1 mm in biological tissue) without having to resort to destructive optical clearing or sectioning techniques [1]. Many approaches currently exist to filter out the multiply scattered light and detect only the unscattered (ballistic) or minimally scattered photons. These include methods such as time and coherence gating, which separate the ballistic photons from the scattered photons based on their transit time to the detector [2, 3]; methods that rely on preserving the initial angular momentum

or polarization modulation [4–7]; and methods that rely on spatial confinement, such as confocal and multi-photon microscopy [1, 8]. An issue with methods that rely on detecting only the minimally scattered photons is the maximum achievable depth of penetration, since the chance of detecting a quasi-ballistic photons decreases exponentially with increasing depth.

Instead of rejecting the scattered photons, other approaches have aimed to take advantage of the information inherent within the detected speckle field that arises from multiply scattered light. Wavefront shaping (WFS) techniques exploit the principles of time-reversal to undo the effect of scattering and enable focusing of light in thick, scattering media [9–12]. However, WFS usually requires long acquisition times to measure the transmission matrix, and/or the presence of a guide star. On the other hand, speckle-correlation-based imaging (SCI) approaches exploit the angular correlations inherent within the scattering process to reconstruct the hidden object and do not need long acquisition times or a guide star [13, 14]. However, SCI methods are limited to working in dark-field scenarios, with sparsely-tagged objects [14], since the detected light must consist solely of light arising from the object.

In this work, we demonstrate imaging of hidden moving objects in a bright-field scenario by leveraging the temporal correlations inherent in the scattering process to separate and remove the dominating contribution from the background [15, 16]. To create a spatially incoherent light source, a spatial light modulator (SLM) was used to apply the same set of random phase patterns during different acquisitions. The use of a deterministic phase modulator ensured that the background contribution remained constant across the detected images. By removing the background component, the speckle pattern from the object was isolated, and the object was reconstructed with high fidelity. Using this technique, we experimentally demonstrate successful recovery of moving objects that would otherwise be obscured by scattering media.

5.2 Principle

Fig. 5.1 presents an overview of our system. A moving object, hidden at a distance u behind a scattering media, is illuminated using a spatially incoherent, narrow-band light source. The scattered light is detected by a high-resolution camera that is placed at a distance v from the scattering media.

In the absence of any correlations in the scattering pattern, the detected image is merely a speckle intensity field. However, by exploiting the deterministic nature of

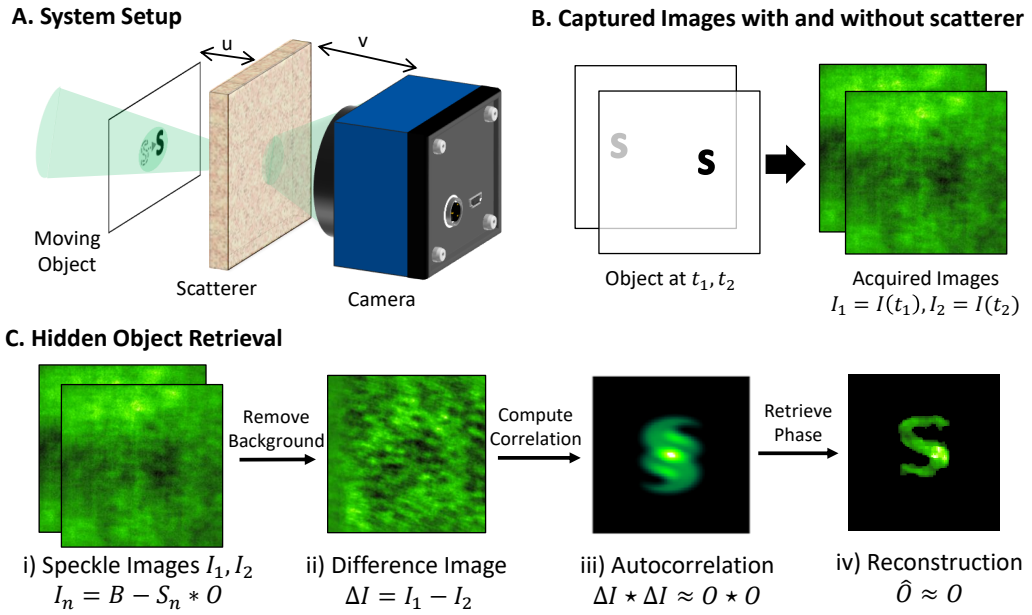

Figure 5.1: **Principle behind non-invasive imaging of obscured moving objects**. A) A spatially incoherent light source illuminates a moving object hidden behind a visually opaque turbid media. The resultant speckle field is captured by a camera sensor. B) Speckle images are acquired by the camera sensor at different times, with the object moving between the captures. The scattering media prevents us from resolving the object. C) The hidden object can be retrieved from the seemingly random speckle images by taking advantage of inherent angular correlations in the scattering pattern. i) Each captured image I_n consists of a background, B, subtracted by the imaged object, where the imaged object is the convolution of the PSF of the scattering media, S, and the object pattern, O. ii) Although the background signal dominates over the object, it can be subtracted out by taking the difference between the two captured images ΔI. iii) The object autocorrelation $O \star O$ is approximated by autocorrelating the difference image ΔI. iv) The hidden object can be reconstructed from the object autocorrelation by using phase retrieval techniques.

scattering, the hidden object can be recovered (Fig. 5.1(c)). Let us first consider the case where light is confined to emit solely within an isoplanatic range, as defined by the angular memory effect (ME). In this case, the detected light can be mathematically represented as

$$I = S * O, \tag{5.2.1}$$

where S is the point spread function (PSF) of the light scattering process, or equivalently the speckle intensity distribution at the camera arising from a single point source at the object plane, and O is the object, defined as the collection of points through which light can be transmitted [14]. For this paper, we use the operator $*$

to denote convolution. The memory effect region can be approximated as $\delta x = \frac{u\lambda}{\pi L}$, where L is the thickness of the scattering media, λ is the wavelength of light, and u is the distance between the scattering media and the object.

If we now consider the case of an absorptive object in a bright-field scenario, then the majority of the detected light arises from the background. Using superposition, the detected intensity image I can be mathematically described as

$$I = B - S * O, \tag{5.2.2}$$

where B is the speckle intensity image arising from the scattered light transmitted through the medium, and $S * O$ is the portion that the object would have contributed if it were transmitting, as opposed to blocking, light [Fig. 5.1(c,i)]. Due to the dominating contribution from the background B, we cannot retrieve O from I alone. By acquiring multiple intensity images with the background, but not the object, constant between acquisitions, we can remove the background signal and thereby retrieve the object.

One strategy to achieve this is to use a moving object. If the object dimensions falls within the ME region, the contribution of the object in each image can be represented as the convolution of the object pattern with an acquisition-dependent PSF. As long as the rest of the sample is static, the speckle field arising from the background will remain unchanged and can be subtracted out by taking the difference between captures. That is,

$$I_n = B - S_n * O, n = 1, 2, ...N \tag{5.2.3}$$

$$\text{and } \Delta I_n = I_{n+1} - I_n = (S_n - S_{n+1}) * O, \tag{5.2.4}$$

where I_n denotes the n^{th} captured image. Since the scattering PSF is a delta-correlated process ($S_n(x) \star S_n(x) \approx \delta(x)$), taking the autocorrelation (AC) of the image ΔI yields the object autocorrelation (OAC), plus additional noise terms [Fig. 5.1(c,iii)]. That is,

$$\Delta I_n \star \Delta I_n \approx 2 \times (O \star O) - (S_n \star S_{n+1} + S_{n+1} \star S_n) * O = 2 \times (O \star O) - \text{noise}, \tag{5.2.5}$$

where $\star$ denotes autocorrelation. We shall refer to $\Delta I_n \star \Delta I_n$ as the speckle autocorrelation (SAC).

The object can be recovered from the SAC by using phase retrieval techniques, such as the Fienup iterative phase retrieval methods, to recover the Fourier phase (Fig. 5.1(c,iv)) [17]. The resultant object will have an image size dictated by the magnification of the system, $M = -\frac{v}{u}$.

Effect of travel distance

Depending on the distance traveled by the object, the PSFs $S_n, n = 1, 2, \ldots$ may or may not be correlated. Figure 5.2 illustrates the effect of travel distance, relative to the ME range, on the SAC. The speckle intensity images I_1, I_2 were determined using simulation. For comparison, the autocorrelation of the object/target, $A = O \star O$ has also been provided [Fig. 5.2(A, "Object AC")]. For simplicity, only the case of two image captures ($n = 1, 2$) has been considered.

For a moving object, the associated PSFs S_1, S_2 will have a degree of correlation $C(\Delta\mathbf{x})$ based on the object travel distance $\Delta\mathbf{x}$. For scattering media with thicknesses L greater than the mean free path, the degree of correlation can be approximated using the angular correlation function

$$C(\Delta\mathbf{x}) = \left[\frac{k\Theta L}{\sinh(k\Theta L)}\right]^2, \tag{5.2.6}$$

where $k = \frac{2\pi}{\lambda}$, L is the thickness of the scattering medium, and $\Theta \approx \frac{\Delta\mathbf{x}}{u}$ [18–20]. When $C(\Delta\mathbf{x}) > 0.5$, the object is considered to have traveled within the ME field of view. The following sections describe three possible cases in more detail: $C(\Delta\mathbf{x}) \approx 1$, $C(\Delta\mathbf{x}) > 0.5$, and $C(\Delta\mathbf{x}) \to 0$.

Case 1: Object travels distance where $C(\Delta\mathbf{x}) \approx 1$

In the case where the object travels a small distance (such that $C(\Delta\mathbf{x}) \approx 1$), we have

$$S_2(\mathbf{x_i}) \approx S_1(\mathbf{x_i} + \Delta\mathbf{x_i}), \tag{5.2.7}$$

where $\mathbf{x} = (x, y), \mathbf{x_i} = (x_i, y_i)$ are coordinates in the object plane and image plane respectively, $\Delta\mathbf{x}$ is the distance the object traveled in the object plane, and $\Delta\mathbf{x_i} = M\Delta\mathbf{x}$. We can equivalently consider the PSF to be the same in both captures and have the object travel between captures. That is,

$$O_2 = O(\mathbf{x_i} + \Delta\mathbf{x_i}), \tag{5.2.8}$$

$$\Delta I = S * [O(\mathbf{x_i}) - O(\mathbf{x_i} + \Delta\mathbf{x_i})], \tag{5.2.9}$$

$$\text{and } \Delta I \star \Delta I = 2A(\mathbf{x_i}) - A(\mathbf{x_i} + \Delta\mathbf{x_i}) - A(\mathbf{x_i} - \Delta\mathbf{x_i}), \tag{5.2.10}$$

where $A = O \star O$ is the object autocorrelation (OAC). The SAC contains three copies of the OAC: a positive copy centered at $\mathbf{x} = (0, 0)$, and two negative copies shifted by an amount commensurate with the object travel distance (as shown in Fig. 5.2(B, "Speckle AC")).

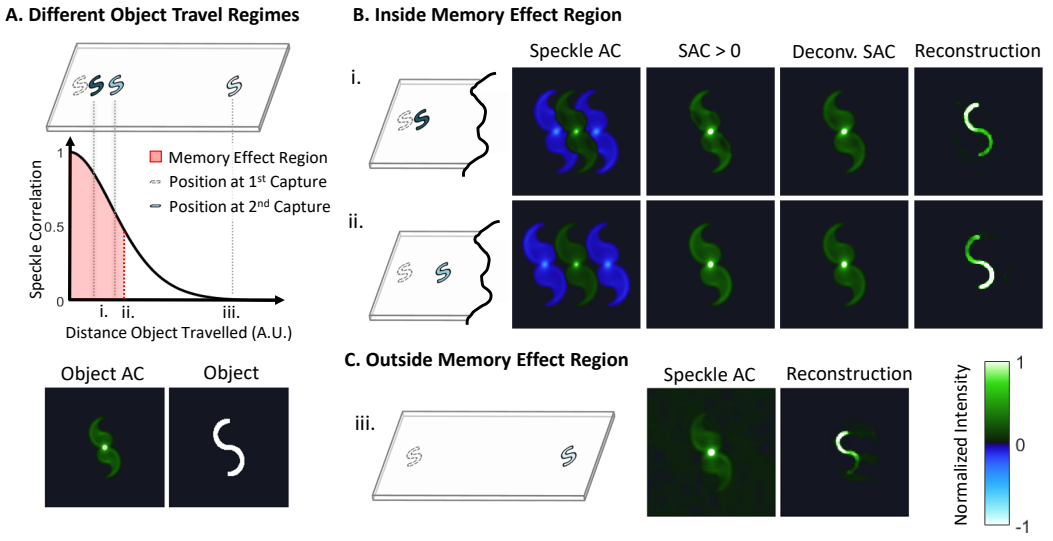

Figure 5.2: **Impact of object travel distance on the computed speckle autocorrelation (SAC).** A) The scattering PSFs experienced by an object have a degree of correlation $C(\Delta\mathbf{x})$ that depends on the distance the object traveled. When $C(\Delta\mathbf{x}) \geq 0.5$ (shown in red), the object is considered to have traveled within the memory effect (ME) region. For comparison, the object and its autocorrelation (AC) are displayed. B) When the object travels inside the ME region, the SAC contains three copies of the object autocorrelation (OAC): a centered, positive copy and two negative copies shifted by an amount proportional to the object travel distance. The OAC can be determined by either deconvolving the SAC or by thresholding out the negative portions (negative with reference to the mean, background level). The object can be reconstructed from the estimated OAC using phase retrieval techniques. C) When the object travels a distance where $C(\Delta\mathbf{x}) \approx 0$, only a single copy of the OAC is seen, with additional noise from the cross-correlation between uncorrelated PSFs. The normalized colormap used to display the AC and reconstructed object, with 0 corresponding to the mean background level.

Since $C(\Delta\mathbf{x}) \approx 1$ when $\Delta\mathbf{x} \approx 0$, the object may travel a distance shorter than the extent of its autocorrelation. In this case, the SAC will yield positive and negative copies of the OAC that overlap (as shown in Fig. 5.2(i)). The OAC can be recovered using deconvolution (as shown in Fig. 5.2(i, "Deconv. SAC.")). Using thresholding to remove the negative portions will adversely impact the positive copy and result in an incomplete estimation of the OAC (Fig. 5.2(i,"SAC>0")). For the results presented in Fig. 5.2, the objects were reconstructed by applying an iterative phase retrieval algorithm on the deconvolved SAC [13, 14, 17].

Case 2: Object travels distance where $C(\Delta\mathbf{x}) > 0.5$

In the regime where the object travels within the angular ME range ($C(\Delta\mathbf{x}) > 0.5$), S_1 and S_2 are correlated. To highlight the impact of the degree of correlation $C(\Delta\mathbf{x})$ on the SAC, we can mathematically represent S_2 as

$$S_2 = C(\Delta\mathbf{x})S_1(\mathbf{x_i} + \Delta\mathbf{x_i}) + \sqrt{1 - [C(\Delta\mathbf{x})]^2}S, \tag{5.2.11}$$

where S is a speckle intensity pattern that is uncorrelated with S_1.The scatter PSFs in the equation above are mean-subtracted speckle intensities. Representing S_2 in the form above allows us to preserve speckle intensity statistics (that is, the speckle intensity variance and mean satisfy $\mathbb{V}[S_1] = \mathbb{V}[S_2]$ and $\mathbb{E}[S_1] = \mathbb{E}[S_2]$ respectively.)

Using Eq. 5.2.11, Eqs. 5.2.4 and 5.2.5 become

$$\Delta I = \left(S_1 - C(\Delta\mathbf{x})S_1(\mathbf{x_i} + \Delta\mathbf{x_i}) - \sqrt{1 - [C(\Delta\mathbf{x})]^2}S\right) * O \tag{5.2.12}$$

$$\text{and } \Delta I \star \Delta I \approx 2A(\mathbf{x_i}) - C(\Delta\mathbf{x})A(\mathbf{x_i} \pm \Delta\mathbf{x_i}) + \sqrt{1 - [C(\Delta\mathbf{x})]^2} \times \text{ noise}, \tag{5.2.13}$$

where the last equation follows from noting that the speckle fields are a delta-correlated process and that the cross-correlation of two uncorrelated speckle intensities yields noise.

The SAC still contains three copies of the OAC. However, the ratio of the intensity of the positive and negative OAC copies is determined by the ME correlation function $C(\Delta\mathbf{x})$. Moreover, since $S_2 \neq S_1$, there is an additional noise term that increases with decreasing $C(\Delta\mathbf{x})$. Since there is no overlap between the positive and negative OAC copies, the OAC can be retrieved by either thresholding out the portions of the SAC that are smaller than the background value (as shown in Fig. 5.2(ii, "SAC>0")), or by deconvolving the image (as shown in Fig. 5.2(ii, "Deconv. SAC.")). Appendix provides more details on the deconvolution algorithm.

Case 3: Object travels distance where $C(\Delta\mathbf{x}) \approx 0$

In the case where the object travels outside the memory effect region between captures, S_1 and S_2 are uncorrelated, and Eq. 5.2.13 can be simplified as Eq. 5.2.5. Comparing the SAC in Fig. 5.2(iii) with those in Fig. 5.2(i-ii), we see that the SAC in the case where the object travels farther than the ME region exhibits more noise. This is expected due to the additional noise term caused by $S_1 \star S_2$ that is not present in Case 1.

From above, in all cases (for $C(\Delta\mathbf{x}) \in [0, 1)$), we can successfully retrieve the object autocorrelation from the acquired speckle images, S_1, S_2. From the estimated OAC, phase retrieval techniques can then be applied to reconstruct the object at diffraction-limited resolution.

5.3 Results

For the experimental demonstration, a laser light beam (CrystaLaser CS532-150-S; $\lambda = 532$ nm) was expanded ($1/e^2$ diameter of 20 cm) and reflected off a phase-only spatial light modulator (SLM; Holoeye PLUTO-VIS) to generate a spatially incoherent light source (Fig. 5.3). An SLM was used in place of a rotating diffuser in order to generate a deterministic, temporally variant set of 50 to 100 random phase patterns. This set of patterns was used for all the acquisitions to ensure that the background light captured remained constant. The object and camera (pco.edge 5.5, PCO-Tech, USA) were placed at a distance $u = 20 - 30$ cm and $v = 10 - 15$ cm from the scattering media (DG10-120 diffuser; Thorlabs, USA) respectively (Fig. 5.3).

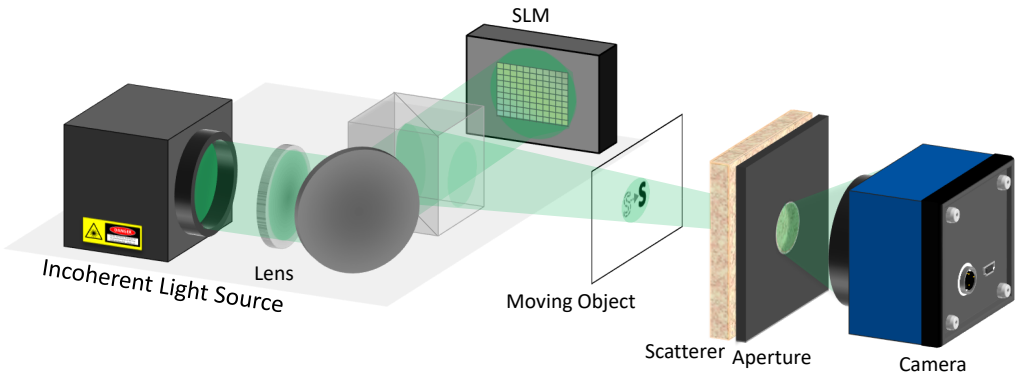

Figure 5.3: **Experimental setup for imaging hidden moving objects.** A spatially incoherent source is generated by reflecting an expanded laser beam (λ= 532 nm; $1/e^2$ diameter of 20 cm) off a spatial light modulator (SLM), which applies a temporally varying set of random phase patterns. The light source is transmitted through the moving object and scattered by the turbid media. The emitted scattered light is collected by a camera. An aperture controls the final object resolution and the speckle size at the camera. Lens focal length = 400 mm.

To ensure that only the object moved between successive image captures, a transmissive SLM (tSLM; Holoeye LC2002 with polarizer) coupled with a polarizer (Thorlabs, LPVISE200-A) was used for amplitude modulation, and served as the object (Fig. 5.4). For each object, a set of n=4 images, $I_1, ...I_4$ were acquired, with the object moving 1.5mm between each acquisition. The raw camera images

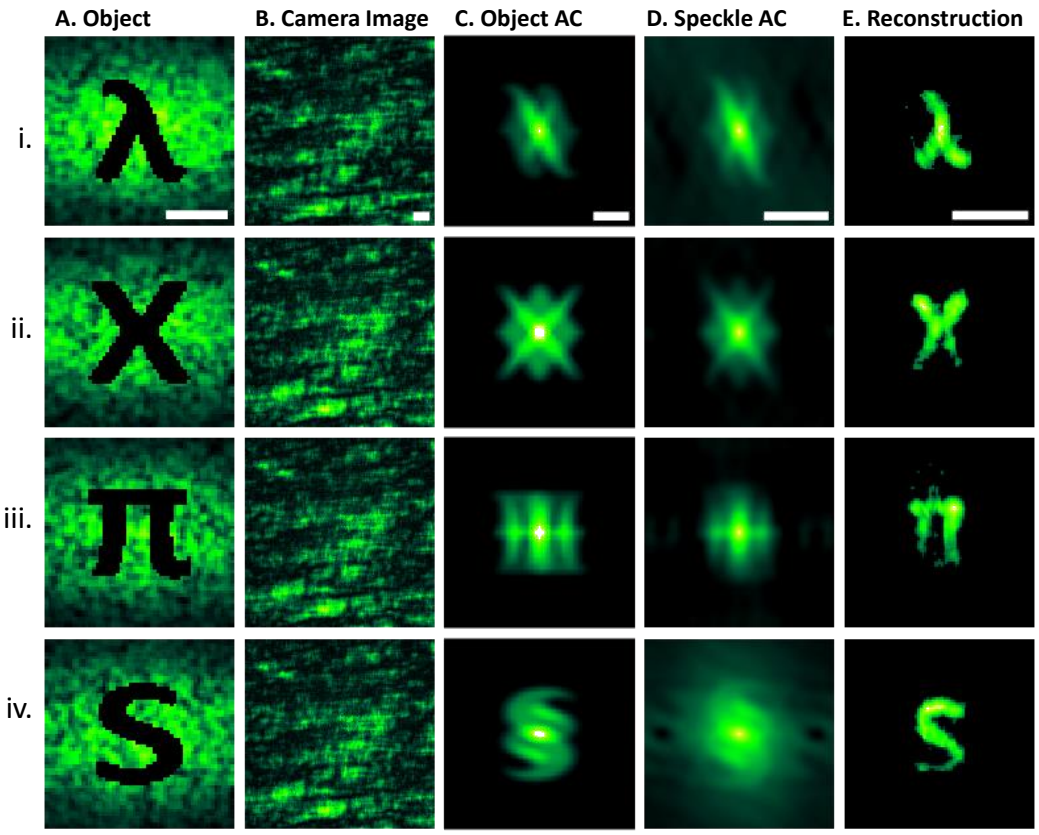

Figure 5.4: **Experimental imaging of moving targets hidden behind a diffuser.** A) The "object" is hidden behind a scattering medium and attenuates light transmission. The object was moved 1.5 mm between acquisitions. B) Due to the presence of the scattering medium, the object is obscured, and the camera image I_1 is dominated by the scattered light from the background. C) The ideal object autocorrelation (AC). D) The speckle autocorrelation $\Delta I \star \Delta I \approx O \star O$. E) By applying phase retrieval on the speckle autocorrelation, the hidden object was reconstructed with high fidelity. Scale bar = 500 μm.

(Fig. 5.4(b)) display a seemingly random light pattern that is similar for different objects. This is due to the dominant contribution of the background.

From each successive pair of acquired images, the OAC (Fig. 5.4(d)) was estimated by deconvolving the SAC. The deconvolved SAC images were then averaged to reduce noise and yield a better estimate of the OAC. A Fienup-type iterative phase retrieval method was applied to reconstruct the hidden object with high fidelity (Fig. 5.4(e)) [13, 14, 17]. One modification that was made to the algorithm was to add an object support to the object constraints; this object support was determined from the OAC support [21, 22]. In all cases, the obscured object was successfully

reconstructed (Fig. 5.4(e)).

To experimentally demonstrate the effect of object travel distance, we moved an object a distance of 0.5, 1, and 3 mm between image acquisitions, and looked at the corresponding SAC and reconstructed object (Fig. 5.5). As expected, the SAC contained three copies of the OAC. We also compared the effect of processing the SAC using deconvolution (Fig. 5.5(b)) vs. thresholding (Fig. 5.5(c)).

For Case i, the object traveled a distance $\Delta\mathbf{x} < \delta\mathbf{x}$, and both the object and SAC overlapped in space between successive acquisitions. In the case of object overlap, only the non-overlapping portion of the object can be retrieved (Fig. 5.5(i)). Comparing the result of deconvolution vs thresholding, the reconstructed image from the deconvolved SAC more closely resembles the original object (Fig. 5.5(i,b)). However, in both cases, what we are left with is an incomplete OAC and reonstructed object.

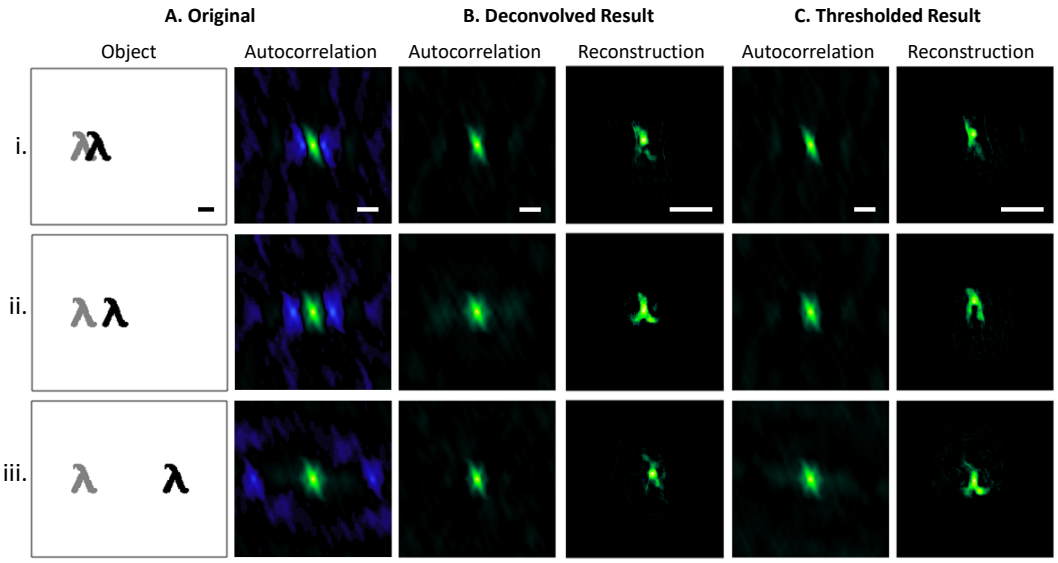

Figure 5.5: **Experimental results showing the effect of object motion distance on the speckle autocorrelation (SAC) and object reconstruction.** A) A diagram showing the position and shape of the object at both time captures, and the SAC, showing three shifted copies of the object autocorrelation (OAC). The effect of applying B) deconvolution and C) thresholding to retain the positive portion (with respect to the mean level) for estimating the OAC from the SAC was compared in three cases (i-iii). The hidden object was reconstructed by applying Fienup phase retrieval on the estimated OAC. Colormap: green is positive, blue is negative (with respect to the mean value, in black). Scale bar: 500 μm.

For Case ii, the object traveled a distance $\delta\mathbf{x} < \Delta\mathbf{x} \leq 2\delta\mathbf{x}$. Since the OAC support

is approximately twice the object support, the positive and negative copies of the OAC overlapped (Fig. 5.5(ii)) [21]. Due to the overlap, thresholding resulted in an imperfect object reconstruction (Fig. 5.5(ii,c)). In contrast, by deconvolving, the signal from the negative copies can be used to gain a better estimate of the OAC, from which the object can be reconstructed (Fig. 5.5(ii,b)).

For Case iii, the object traveled a distance $\Delta\mathbf{x} >> 2\delta\mathbf{x}$, and there was no overlap in the SAC. Due to the large $\Delta\mathbf{x}$, $C(\Delta\mathbf{x})$ decreased, and correspondingly, the noise increased. Since the signal-to-noise ratio (SNR) of the negative copies decreased, the entire OAC cannot be seen in the negative copies (Fig. 5.5(iii,a)); thus, performing a deconvolution results in a noisy, imperfect OAC (Fig. 5.5(iii,b)), and it is more advisable to use thresholding to retain only the positive portion of the SAC (Fig. 5.5(iii,c). If we compare the reconstructed objects in both cases, we see that the object from the thresholded result more closely resembles the original object.

Imaging moving objects hidden between scattering media

To further demonstrate our imaging technique, we placed a moving object between two diffusers (Newport 10^o Light Shaping Diffuser, Thorlabs DG10-220-MD) (Fig. 5.6(A)). A moving object (a bent black wire) was flipped in and out of the light path between image captures, such that $I_2 = B$. We blocked the partially-developed speckle field (from the propagation of the SLM phase pattern) and used only the fully-developed speckle pattern [23]. This fully-developed speckled pattern was transmitted through both scattering media and the moving object. The emitted scattered light was detected by a camera.

The background halo from each detected speckle intensity image was estimated and removed by performing Gaussian filtering (500x500 kernel, $\sigma = 100$), and then dividing each image by the background halo [14]. The SAC was then computed to estimate the OAC, from which phase retrieval was applied to reconstruct the hidden object. Although the object is fully obscured from both sides by scattering media and cannot be resolved from the camera image alone, using our technique, we were able to successfully reconstruct the hidden object with high fidelity (Fig. 5.6(B)).

5.4 Discussion and Conclusion

In this paper, we demonstrated successful reconstruction of moving targets that were hidden behind an optically turbid media. Although the angular memory effect has already been used to demonstrate imaging of hidden targets, to the best of our knowledge, these prior systems were limited to imaging dark-field, sparsely-tagged

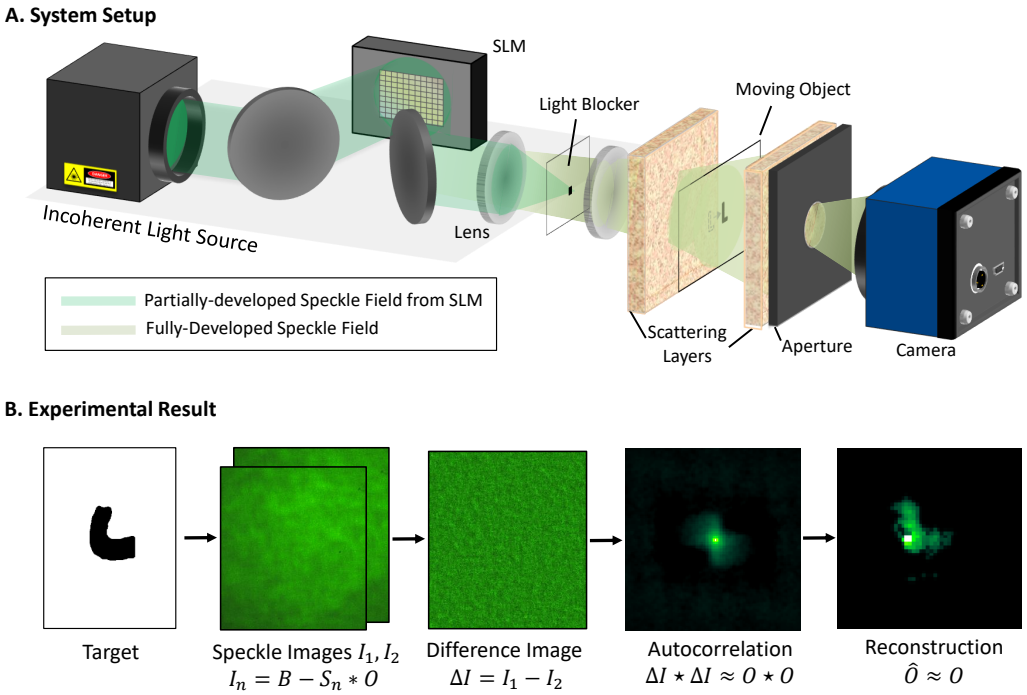

Figure 5.6: **Experimental retrieval of moving targets hidden within a scattering object.** A) Schematic of the experimental setup. A spatially incoherent light source is generated by reflecting an expanded laser beam off a spatial light modulator (SLM) that applied a temporally variant random phase pattern. The partially developed speckle field component is blocked, and only the fully-developed speckle field transmits through the moving object and two scattering layers. The emitted scattered light is collected by a camera. An aperture controls the resolution and the speckle size at the camera. B) Experimental result of a moving target. Two speckle intensity images , I_1, I_2, were captured, with the target present for the first capture, and absent for the second. The background halo from I_1 and I_2 were removed prior to computing the difference $\Delta I = I_2 - I_1 \approx S_1 * O$. The speckle autocorrelation yielded an estimate of the object autocorrelation, from which the target was retrieved by applying Fienup phase retrieval. Lens focal length = 400 mm.

objects [13, 14, 24]. We extended this work to imaging in the bright-field scenario by exploiting the temporal correlations inherent in the scattering process to remove the dominating contribution from the background and isolate the signal arising from the object [15, 16]. Although we demonstrated our results on non-emitting objects in the bright-field scenario, our technique works equally well with transmissive or reflective objects. A cursory examination reveals that, when $I_n = B + S_n * O$ and $\Delta I = I_n - I_{n+1}$, the speckle autocorrelation is still given by Eq. 5.2.5, similar to imaging absorptive objects in the bright-field scenario. In the remainder of this section, we discuss some of the factors that impact system performance.

Firstly, our method depends on the angular correlations inherent in the scattering process. Thus, the object dimension should fall within the angular memory effect field of view (FOV), approximated using the full-width-half-maximum (FWHM) of the correlation function, $\frac{u\lambda}{\pi L}$. The axial extent of the object, δz, should also fall within the axial decorrelation length $\frac{2\lambda}{\pi}\left(\frac{u}{D}\right)^2$ [25]. Since the ME FOV is inversely proportional to L, our technique works best with thin scattering media, or through more anisotropically scattering media, since anisotropy enhances the angular memory effect range [20]. Strongly anisotropic media, such as biological tissue, also exhibit the translational memory effect, which may be exploited to further the fidelity of imaging through scattering layers [26].

Secondly, to maximize SNR and minimize overlap, the object travel distance should be such that $\delta x < \Delta x$ and $C(\Delta\mathbf{x}) \geq 0.5$, since smaller values of $C(\Delta\mathbf{x})$ results in higher levels of noise. However, if the object moves such a large distance as to not fall within the laser light beam, then $I_2 = B$, and $\Delta I = S_1 * O$, and we can also retrieve the object with high fidelity. In all these cases, successful retrieval of the object is dependent on the background light pattern remaining constant between successive image captures. Thus, the illuminated portion of the tissue should remain constant between image captures, and the time between image captures should fall well within the temporal decorrelation time of the scattering sample. For biological samples, the temporal decorrelation time is related to the motion of scatterers embedded within [27].

Imaging through biological samples can be achieved using a faster system. The imaging speed in our current design was limited by the refresh rate of the SLM($\approx$ 8 Hz) and by the exposure time required to capture an image (50-200ms). With a more powerful laser, or a faster deterministic random phase modulator, it would be possible to shorten our imaging time, and extend our work to imaging within non-static samples, such as biological tissue.

A third factor in the fidelity of the reconstruction is the complexity of the object and the size of the background relative to the object. The dynamic range of the camera should be large enough to resolve the equivalent speckle signal from the object. Since the signal contrast is inversely related to the object complexity [14], the dynamic range of the camera limits the maximum object complexity. To maximize the SNR, the camera exposure and laser power should be adjusted such that the full well depth of the camera is utilized. A camera with a larger well depth and dynamic range would provide higher SNR and the capability to image more complex objects.

The diameter of the aperture in the system can be adjusted to fine-tune the image resolution and control the object complexity.

Lastly, each speckle grain at the camera should satisfy the Nyquist sampling criterion and be easily resolvable. At the same time, the number of speckle grains that are captured in each image should also be maximized in order to maximize SNR. Although the scattering PSFs are ideally a delta-correlated process, in practice, we are only sampling a finite extent of the PSF. Thus, the PSF autocorrelation yields a delta function plus some background noise which can be minimized by increasing the number of captured speckle grains [14]. Due to Nyquist requirements, the maximum number of speckle grains is a function of the camera resolution; thus, a high resolution camera would provide lower noise. Another method to reduce this speckle noise is to take multiple acquisitions and compute the average of the speckle autocorrelation images.

In conclusion, we demonstrated successful imaging of hidden moving targets through scattering samples. The temporal and angular correlations inherent in the scattered light pattern allowed us to reconstruct the hidden object in cases where multiply scattered light dominates over ballistic light. This paper presented a first proof of concept. Although we demonstrated imaging of binary-amplitude targets, our system can also be extended to imaging gray-scale targets [28]. Since our imaging technique utilizes the angular memory effect, it is scalable. Moreover, our method does not require access inside the scattering media, and can therefore be used as a black box imaging system. With appropriate optimization, this opens up potential for use in applications involving the tracking of moving object in turbulent atmospheres, such as fog or underwater.

Appendix

Deconvolving the Speckle Autocorrelation

To deconvolve the speckle autocorrelation (SAC), $\Delta I \star \Delta I$, Weiner deconvolution was applied to reduce the deconvolution noise. We briefly describe the process here. We can rewrite Eq. 5.2.13 as

$$g = \Delta I \star \Delta I \approx A * h + n = y + n,$$

where $h(\mathbf{x_i}) = 2\delta(\mathbf{x_i}) - C(\Delta\mathbf{x})\delta(\mathbf{x_i} \pm \Delta\mathbf{x_i})$, $A = O \star O$, and n is the noise term. In this case, Weiner deconvolution estimates A by applying

$$\mathcal{F}(A) = \mathcal{F}(g)\frac{\mathcal{F}(h)}{|\mathcal{F}(h)|^2 + k} \approx \frac{\mathcal{F}(y)}{\mathcal{F}(h)},$$

where $\mathcal{F}$ is the Fourier transform operator, and $k = \frac{\mathcal{F}(n)}{\mathcal{F}(g)} \approx \frac{1}{SNR}$ estimates the SNR level of your signal [29]. Since all object ACs have a peak value of $A(\mathbf{x_i} = (0,0)) = \sum_{\mathbf{x}} O^2$, to determine h from the SAC, we estimated the value of $C(\Delta\mathbf{x})$ by taking the negative/positive peak values in the SAC. The locations of the negative peaks, with respect to the centered, positive peak, provided the value of the shift $\Delta\mathbf{x_i}$.

Object Complexity and SNR

In this section, we analyze the relation between the object complexity, full well depth, and signal to noise ratio. Let us consider the light beam incident upon the object plane. Let the area the light beam covers be denoted $a = N\delta_x$, where δ_x is the area of a resolution cell area (RCA). Let N_o be the number of RCAs the object occupies; then, the number of light-emitting RCAs from the background is $N_b = N - N_o$. The detected image intensity, $I = B - S * O$, is composed of N_b speckle patterns and will have a mean and standard deviation $\mu_b \propto N_b$ and $\sigma_b \propto \sqrt{N_b}$ respectively. The signal from the object, $S * O$ is composed of the sum of N_o speckle intensities, and will have a mean and standard deviation of $\mu_o \propto N_o$ and $\sigma_o \propto \sqrt{N_o}$. Since the object signal is carried by the background light, we need $\mu_b > \mu_o \implies N_b > N_o$ (1).

N_b and N_o are also limited by the specifications of the camera. Let F denote the full well depth, η the quantum efficiency of the detector, and b denote the number of quantization bits in the analog-to-digital converter. For ease of discussion, let the mean detected speckle intensity arising from a single RCA be $\eta\mathbb{E}[S] = 1$. Since each image we captured has a mean intensity of $\mu_B = N_b$, we need $N_b \leq F$ in order to prevent saturation. Since the majority of the information about the object comes from the fluctuations in the speckle pattern, we can approximate the magnitude of the

signal to be σ_o. Thus, in order to resolve the object signal, we have the requirement that $\frac{\sigma_o}{\mu_o} = \frac{1}{\sqrt{N_o}} > \frac{F}{2^b}$ (2). However, at the same time, increasing image complexity, N_o, decreases signal contrast, since $C \doteq \frac{\sigma_o}{\mu_o} = \frac{1}{\sqrt{N_o}}$.

Let us now consider the effect of shot noise. Each detected image can be mathematically represented as $I_i = B - S_i * O + n_i$ where n is the shot noise. The detected shot noise would have a mean and standard deviation of $\mu_{SN} = \eta\mathbb{E}[I] = N_b$ and $\sigma_{SN} = \sqrt{\eta\mathbb{E}[I]} = \sqrt{N_b}$. For each detected image, the relative signal magnitude is $C = \frac{1}{\sqrt{N_o}} > \frac{\sigma_{SN}}{\mu_{SN}} = \frac{1}{\sqrt{N_b}}$ which leads to $N_b > N_o$ (3). For each detected image, the limit on the shot noise is when $\mu_{SN} = N_b \approx F$, in which case we would need $\frac{1}{\sqrt{N_o}} > \frac{1}{\sqrt{F}}$, or $F > N_o$. Thus, we have the requirement that $F \geq N_b > N_o$ (2). This, in conjunction with (1), shows that the full well depth and number of quantization bits of the camera are the ultimate limiting factor on the allowable object complexity.

This analysis only includes the effect of shot noise, and not any other sources of noise, such as decorrelation noise. From the above analysis, we have the object signal contrast, $C = \frac{1}{\sqrt{N_o}}$. In order to successfully retrieve more complex objects, we need to decrease other sources of noise as much as possible.

References

[1] Vasilis Ntziachristos. “Going deeper than microscopy: the optical imaging frontier in biology”. In: *Nature Methods* 7.8 (2010), pp. 603–614.

[2] David Huang et al. “Optical coherence tomography”. In: *Science* 254.5035 (1991), p. 1178.

[3] Stefan Andersson-Engels et al. “Time-resolved transillumination for medical diagnostics”. In: *Optics Letters* 15.21 (1990), pp. 1179–1181.

[4] Glenn H Chapman et al. “Angular domain imaging of objects within highly scattering media using silicon micromachined collimating arrays”. In: *IEEE Journal of Quantum Electronics* 9.2 (2003), pp. 257–266.

[5] Sungsam Kang et al. “Imaging deep within a scattering medium using collective accumulation of single-scattered waves”. In: *Nature Photonics* 9.4 (2015), pp. 253–258.

[6] Hema Ramachandran and Andal Narayanan. “Two-dimensional imaging through turbid media using a continuous wave light source”. In: *Optics Communications* 154.5 (1998), pp. 255–260.

[7] Sriram Sudarsanam et al. “Real-time imaging through strongly scattering media: seeing through turbid media, instantly”. In: *Scientific Reports* 6 (2016).

[8] Fritjof Helmchen and Winfried Denk. “Deep tissue two-photon microscopy”. In: *Nature Methods* 2.12 (2005), pp. 932–940.

[9] Allard P Mosk et al. “Controlling waves in space and time for imaging and focusing in complex media”. In: *Nature Photonics* 6.5 (2012), pp. 283–292.

[10] Ivo M Vellekoop and AP Mosk. “Focusing coherent light through opaque strongly scattering media”. In: *Optics Letters* 32.16 (2007), pp. 2309–2311.

[11] Xiao Xu, Honglin Liu, and Lihong V Wang. “Time-reversed ultrasonically encoded optical focusing into scattering media”. In: *Nature Photonics* 5.3 (2011), pp. 154–157.

[12] Ying Min Wang et al. “Deep-tissue focal fluorescence imaging with digitally time-reversed ultrasound-encoded light”. In: *Nature Communications* 3 (2012), p. 928.

[13] Jacopo Bertolotti et al. “Non-invasive imaging through opaque scattering layers”. In: *Nature* 491.7423 (2012), pp. 232–234.

[14] Ori Katz et al. “Non-invasive single-shot imaging through scattering layers and around corners via speckle correlations”. In: *Nature Photonics* 8.10 (2014), pp. 784–790.

[15] Edward Haojiang Zhou et al. “Focusing on moving targets through scattering samples”. In: *Optica* 1.4 (2014), pp. 227–232.

[16] Cheng Ma et al. “Time-reversed adapted-perturbation (TRAP) optical focusing onto dynamic objects inside scattering media”. In: *Nature Photonics* 8.12 (2014), pp. 931–936.

[17] James R Fienup. “Phase retrieval algorithms: a comparison”. In: *Applied Optics* 21.15 (1982), pp. 2758–2769.

[18] Shechao Feng et al. “Correlations and fluctuations of coherent wave transmission through disordered media”. In: *Physical Review Letters* 61.7 (1988), p. 834.

[19] R Berkovits, M Kaveh, and S Feng. “Memory effect of waves in disordered systems: a real-space approach”. In: *Physical Review B* 40.1 (1989), p. 737.

[20] Sam Schott et al. “Characterization of the angular memory effect of scattered light in biological tissues”. In: *Optics Express* 23.10 (2015), pp. 13505–13516.

[21] James R Fienup, TR Crimmins, and W Holsztynski. “Reconstruction of the support of an object from the support of its autocorrelation”. In: *JOSA* 72.5 (1982), pp. 610–624.

[22] JR Fienup and CC Wackerman. “Phase-retrieval stagnation problems and solutions”. In: *JOSA A* 3.11 (1986), pp. 1897–1907.

[23] Bernd Ruffing and Jürgen Fleischer. “Spectral correlation of partially or fully developed speckle patterns generated by rough surfaces”. In: *JOSA A* 2.10 (1985), pp. 1637–1643.

[24] Ori Katz, Eran Small, and Yaron Silberberg. “Looking around corners and through thin turbid layers in real time with scattered incoherent light”. In: *Nature Photonics* 6.8 (2012), pp. 549–553.

[25] Isaac Freund. “Looking through walls and around corners”. In: *Physica A: Statistical Mechanics and its Applications* 168.1 (1990), pp. 49–65.

[26] Benjamin Judkewitz et al. “Translation correlations in anisotropically scattering media”. In: *Nature Physics* 11.8 (2015), pp. 684–689.

[27] Joshua Brake, Mooseok Jang, and Changhuei Yang. “Analyzing the relationship between decorrelation time and tissue thickness in acute rat brain slices using multispeckle diffusing wave spectroscopy”. In: *JOSA A* 33.2 (2016), pp. 270–275.

[28] Huijuan Li et al. “Simulation and experimental verification for imaging of gray-scale objects through scattering layers”. In: *Applied Optics* 55.34 (2016), pp. 9731–9737.

[29] Rafael C. Gonzalez and Richard E. Woods. *Digital Image Processing (3rd Edition)*. Prentice-Hall, Inc., 2006. ISBN: 013168728X.